

BENCHMARK DATA AND ANALYSIS OF DILUTE TURBULENT FLUID-PARTICLE  
FLOW IN VISCOUS AND TRANSITIONAL REGIMES

By

MARK PEPPLE

A DISSERTATION PRESENTED TO THE GRADUATE SCHOOL  
OF THE UNIVERSITY OF FLORIDA IN PARTIAL FULFILLMENT  
OF THE REQUIREMENTS FOR THE DEGREE OF  
DOCTOR OF PHILOSOPHY

UNIVERSITY OF FLORIDA

2010

© 2010 Mark Pepple

To my family and friends for their encouragement throughout graduate school

“If you wait for perfect conditions, you will never get anything done”  
Ecclesiastes 11:4

“Not to us, O Lord, not to us but to your name be the glory,  
because of your love and faithfulness”  
Psalm 115:1

## ACKNOWLEDGMENTS

My sincere appreciation goes to my advisor, Jennifer Sinclair Curtis for her guidance, encouragement, and support. I am most grateful for the eternal perspective she exuded in the midst of a demanding professional career. I am indebted to Dr. Caner Yurteri for instructing me on LDV my first two years and entertaining all my subsequent questions. I thank my parents for their love, support, and encouragement throughout the trials of graduate school. I also want to remind them that graduate school was initially their idea. I am grateful for my many friends without whom I would not have survived or enjoyed the last five-plus years. Allyn and Eric, thanks for the weekly lunches and book discussions, they were always a welcomed interruption. Officemates, thank you for putting up with me and sharing in the ups and downs of graduate school.

# TABLE OF CONTENTS

	<u>page</u>
ACKNOWLEDGMENTS.....	4
LIST OF TABLES.....	8
LIST OF FIGURES.....	10
LIST OF ABBREVIATIONS .....	13
ABSTRACT.....	18
CHAPTER	
1 INTRODUCTION AND BACKGROUND .....	20
Introduction .....	20
Background .....	21
Stokes number .....	22
Bagnold number .....	23
Mean Flow.....	25
Collision-Dominated Flow .....	25
Viscous-Dominated Flow .....	28
Turbulence Modulation.....	30
Collision-Dominated Flow .....	30
Viscous-Dominated Flow .....	31
Turbulence Modulation Correlations .....	32
Radial Solids Concentration Profile .....	34
Two-Phase Flow Measurement Techniques .....	35
Two-Phase Flow Modeling .....	37
Motivation.....	39
2 EXPERIMENTAL SETUP AND METHODS .....	44
Experimental Setup .....	44
Experimental Particles .....	47
Laser Doppler Velocimetry .....	49
Basic principles.....	49
Phase Doppler anemometry .....	52
Solids concentration .....	54
Experimental Procedures .....	56
LDV/PDPA System .....	56
Phase Discrimination .....	58
Data Limitations .....	59
Exclusion of 1.5 mm solid data .....	59
Limited radial penetration in slurry of 0.5 mm particles .....	60

Procedural Obstacles.....	60
Flow control and air bubbles .....	60
Excessive turbulence .....	61
Phase discrimination and particle selection .....	63
Other improvements.....	66
Equipment/instrumentation issues .....	67
Error Analysis .....	68
Velocity and size measurements .....	68
Radial location .....	69
Solids concentration .....	70
Pressure measurements .....	71
3 TWO-PHASE MODEL .....	85
Kinetic Theory of Granular Flow.....	85
Governing Equations .....	86
Boundary Conditions and Model Solution.....	88
Results .....	88
4 PRESSURE LOSS IN PIPE BENDS OF LARGE CURVATURE AT HIGH RE .....	91
Introduction .....	91
Experimental .....	95
Results and Discussion .....	96
Influence of Downstream Tangent: Configuration A.....	97
Influence of Downstream Tangent: Configuration B.....	99
Conclusion .....	100
5 SINGLE-PHASE VALIDATION .....	108
Introduction .....	108
Experimental .....	109
Scaling.....	110
Results .....	111
Effect of Re.....	112
Turbulence Measurements in Air using Hot-Wire.....	112
LDV vs Hot-wire Measurements in Air Flow .....	113
Turbulence Measurements in Water .....	114
Conclusion .....	115
6 LIQUID-SOLID FLOW .....	124
Pressure Drop.....	124
Correlations .....	125
Bartosik.....	125
Littman and Paccione.....	127
Ferre and Shook.....	128
Results.....	129

Experimental.....	129
Correlations .....	131
Velocity Measurements .....	132
Fully Developed Flow and Reproducibility of Data .....	133
Mean Velocity.....	134
Fluctuating Velocity .....	135
Effect of Re .....	135
Effect of solids concentration .....	137
Error Analysis .....	140
Conclusion .....	141
7 CONCLUSIONS AND RECOMMENDATIONS .....	165
APPENDIX	
A EXPERIMENTAL VELOCITY DATA.....	169
Two-Phase Flows .....	169
0.5 mm Particles .....	169
1.0 mm Particles .....	172
1.5 mm Particles .....	177
Reproducibility.....	181
Fully-Developed Flow .....	182
Single-Phase Flows .....	182
B EXPERIMENTAL PRESSURE DATA.....	184
Two-Phase Flows .....	184
Single-Phase Flows .....	184
LIST OF REFERENCES.....	188
BIOGRAPHICAL SKETCH.....	197

## LIST OF TABLES

<u>Table</u>	<u>page</u>
1-1 Mean velocity behavior for collision-dominated flow.....	41
1-2 Mean velocity behavior for viscous-dominated flow .....	41
1-3 Fluctuating velocity behavior for collision-dominated flow.....	42
1-4 Fluctuating velocity behavior for viscous-dominated flow.....	42
2-1 LDV/PDPA settings .....	80
4-1 Published experimental pressure loss data in pipe bends .....	102
4-2 Total bend loss coefficient .....	107
5-1 Turbulence measurements in air .....	117
5-2 Turbulence measurements in water .....	118
5-3 Comparison of friction velocity values .....	119
5-4 Ratio of mean to maximum velocity, power law exponent.....	119
5-5 DNS turbulence data.....	119
6-1 Experimental parameters in dimensionless numbers .....	146
A-1 Fluid and solid velocity measurements for 0.7% solids at $Re=2.0 \times 10^5$ .....	169
A-2 Fluid and solid velocity measurements for 1.7% solids at $Re=2.0 \times 10^5$ .....	169
A-4 Fluid and solid velocity measurements for 0.7% solids at $Re=3.35 \times 10^5$ .....	170
A-5 Fluid and solid velocity measurements for 1.7% solids at $Re=3.35 \times 10^5$ .....	170
A-6 Fluid and solid velocity measurements for 3% solids at $Re=3.35 \times 10^5$ .....	171
A-7 Fluid and solid velocity measurements for 0.7% solids at $Re=5.0 \times 10^5$ .....	171
A-8 Fluid and solid velocity measurements for 1.7% solids at $Re=5.0 \times 10^5$ .....	171
A-9 Fluid and solid velocity measurements for 3% solids at $Re=5.0 \times 10^5$ .....	172
A-10 Fluid and solid velocity measurements for 0.7% solids at $Re=2.0 \times 10^5$ .....	172
A-12 Fluid and solid velocity measurements for 3% solids at $Re=2.0 \times 10^5$ .....	173

A-14	Fluid and solid velocity measurements for 1.7% solids at $Re=3.35 \times 10^5$ .....	174
A-16	Fluid and solid velocity measurements for 0.7% solids at $Re=5.0 \times 10^5$ .....	175
A-18	Fluid and solid velocity measurements for 3% solids at $Re=5.0 \times 10^5$ .....	176
A-19	Fluid velocity measurements for 0.7% solids at $Re=2.0 \times 10^5$ .....	177
A-20	Fluid velocity measurements for 1.7% solids at $Re=2.0 \times 10^5$ .....	177
A-22	Fluid velocity measurements for 0.7% solids at $Re=3.35 \times 10^5$ .....	178
A-24	Fluid velocity measurements for 3% solids at $Re=3.35 \times 10^5$ .....	179
A-26	Fluid velocity measurements for 1.7% solids at $Re=5.0 \times 10^5$ .....	180
A-28	Three measurements of solids fluctuating velocity for 1.0 mm particles at 0.7% solids at $Re=2.0 \times 10^5$ .....	181
A-29	Solid mean and fluctuating velocity at two radii and two axial locations for 0.5 mm particles at 0.7% solids at $Re=2.0 \times 10^5$ .....	182
A-30	Mean and fluctuating velocity of single phase water .....	182
B-3	Pressure gradient for 0.5 mm particles .....	184
B-3	Pressure gradient for 1.0 mm particles .....	184
B-3	Pressure gradient for 1.5mm particles .....	184
B-1	Pressure along vertical pipe and bend with sudden expansion at downstream tangent (Configuration A) .....	185
B-2	Pressure along vertical pipe and bend with steel pipe at downstream tangent (Configuration B) .....	186
B-3	Pressure along vertical pipe and bend with sudden expansion at downstream tangent (Configuration A) with vertical adjustment .....	187
B-4	Pressure along vertical pipe and bend with steel pipe at downstream tangent (Configuration B) with vertical adjustment.....	187

## LIST OF FIGURES

<u>Figure</u>	<u>page</u>
1-1 Gas-solid pressure drop.....	43
2-1 Flow loop .....	74
2-2 Venturi eductor .....	75
2-3 Configuration of pressure tap .....	75
2-4 Vertical pipe dimensions .....	76
2-5 Experimental particles.....	77
2-6 Resolving directional ambiguity with frequency shift .....	78
2-7 LDV probe volume fringes .....	79
2-8 Experimental probe volume dimensions .....	79
2-9 Light scattering intensity for 1 mm sphere for 514 nm light.....	81
2-10 Frequency and phase measurements of a Doppler burst .....	81
2-11 Signal processing flowchart .....	82
2-12 Phase Doppler setup.....	83
2-13 Sampling rate of Doppler burst.....	84
3-1 Solid fluctuating velocity of gas-solid flow of 243 $\mu\text{m}$ polystyrene particles at $\text{Re} \sim 2.2 \times 10^4$ .....	90
3-2 Solid fluctuating velocity of liquid-solid flow of 2.32 mm glass particles at $\text{Re} = 6.7 \times 10^4$ .....	90
4-1 Loss coefficient profiles.....	103
4-2 Bend geometry and discharge configurations.....	104
4-3 Loss coefficient upstream of bend entrance .....	105
4-4 Loss coefficient through bend.....	106
5-1 Effect of Reynolds number in air measurements .....	120
5-2 Effect of $\text{Re}$ in water measurements .....	121

5-3	Effect of pipe diameter .....	122
5-4	LDV vs. hot-wire measurements in air .....	122
5-5	Turbulence measurements in water .....	123
5-6	Turbulence measurements in air and water.....	123
6-1	Pressure drop with 0.5 mm particles .....	143
6-2	Pressure drop with 1.0 mm particles .....	144
6-3	Pressure drop with 1.5 mm particles .....	145
6-4	Dimensionless parameters of experiments .....	147
6-5	Fully developed flow.....	148
6-6	Linear pressure profile .....	148
6-7	Reproducibility of measurements .....	149
6-8	Fluid mean velocity at 0.7% solids .....	150
6-9	Fluid mean velocity at 1.7% solids .....	151
6-10	Fluid mean velocity at 3% solids.....	152
6-11	Solid mean velocity at 0.7% solids .....	153
6-12	Solid mean velocity at 1.7% solids .....	154
6-13	Solid mean velocity at 3% solids .....	155
6-14	Fluid fluctuating velocity at 0.7% solids.....	156
6-15	Fluid fluctuating velocity at 1.7% solids.....	157
6-16	Fluid fluctuating velocity at 3% solids .....	158
6-17	Solid fluctuating velocity at 0.7% solids.....	159
6-18	Solid fluctuating velocity 1.7% solids.....	160
6-19	Solid fluctuating velocity at 3% solids.....	161
6-20	Fluid fluctuating velocity error based on ensemble size .....	162
6-21	Evolution of $u_f'$ with data count .....	162

6-22	Evolution of $u_s'$ with data count.....	163
6-23	Fluid fluctuating velocity error based on standard deviation of $u_f'$ after 250 measurements.....	164

## LIST OF ABBREVIATIONS

A	cross-sectional area of probe volume [ $\text{m}^2$ ]
Ba	Bagnold number
$C_0$	correction factor based on length of downstream tangent
$C_d$	coefficient of drag
$C_f$	correction factor based on pipe roughness
$C_{Re}$	correction factor based on Re
$c_1$	k- $\epsilon$ turbulence model constant
$c_2$	k- $\epsilon$ turbulence model constant
$c_3$	k- $\epsilon$ turbulence model constant
D	pipe diameter [m]
$D_L$	laser beam diameter [m]
d	particle diameter [m]
$d_{30}$	volume-average particle diameter [m]
$E_{pt}$	pseudo-thermal energy [ $\text{m}^2 \text{s}^{-2}$ ]
F	focal length [mm]
$F_D$	drag force of fluid on particle
$F_{KS}$	interfacial energy flux by fluid-solid interactions
$F_{MOD}$	fluid-particle interaction term
Fr	Froude Number
$f_D$	Doppler frequency [ $\text{s}^{-1}$ ]
$f_f$	fluid phase friction factor
$f_s$	solid-phase friction factor
$f_x$	flux normal to probe volume cross section
$f_1$	k- $\epsilon$ turbulence model constant

$f_2$	k- $\epsilon$ turbulence model constant
$g$	gravity [ $\text{m s}^{-2}$ ]
$i_f$	hydraulic gradient of fluid
$i_m$	hydraulic gradient of two-phase flow
$K$	pressure loss coefficient
$K_i$	inertial coefficient in Bagnold's $\tau_s$
$K_v$	viscous coefficient in Bagnold's $\tau_s$
$k$	turbulent energy production [ $\text{m}^2 \text{s}^{-2}$ ]
$k_r$	surface roughness [m]
$k_t$	total bend loss coefficient
$k_t^*$	$k_t$ at $\text{Re} = 10^6$
$l_e$	length of most energetic eddy [m]
$N$	ensemble size
$n$	number of particles
$P$	pressure, including height adjustment if needed [Pa]
$P_{\text{meas}}$	raw pressure [Pa]
$P_{\text{ref}}$	pressure 37 diameters upstream of bend entrance [Pa]
$q_{\text{pt}}$	pseudo-thermal energy conductive flux
$R$	absolute pipe radius [m]
$R_b$	radius of bend curvature
$\text{Re}$	Reynolds number = $DU\rho_f/\mu$
$\text{Re}_f$	Reynolds number based on mean fluid velocity in two-phase flow
$\text{Re}_p$	particle Reynolds number = $du_r\rho_f/\mu$
$r$	pipe radius [m]
$\text{St}$	turbulent Stokes number

$S_{zP}$	standard error in pressure drop
$T$	period of signal [s]
$t$	time [s]
$t_f$	fluid response time [s]
$t_p$	particle response time [s]
$U_f$	mean fluid velocity [ $m\ s^{-1}$ ]
$U_m$	mean slurry velocity [ $m\ s^{-1}$ ]
$U_s$	mean solid velocity [ $m\ s^{-1}$ ]
$U_t$	friction velocity [ $m\ s^{-1}$ ]
$U$	instantaneous velocity [ $m\ s^{-1}$ ]
$u_r$	absolute value of slip velocity [ $m\ s^{-1}$ ]
$u'_t$	shear induced turbulence in single-phase flow [ $m\ s^{-1}$ ]
$u_x$	velocity normal to LDV fringes [ $m\ s^{-1}$ ]
$V$	probe volume [ $m^3$ ]
$W$	uncertainty in pressure drop
$X^*$	location downstream of bend where pressure gradient is equal to that upstream of bend
$z$	vertical distance [m]
$z_c$	confidence coefficient
Greek	
$\alpha$	function of $(R/r)$ in $k_t$
$\gamma$	shear rate [ $s^{-1}$ ]
$\gamma_{pt}$	pseudo-thermal energy dissipation rate
$\Delta z$	vertical distance [m]
$\Delta h_t$	total pressure change due to bend [Pa]
$\Delta t$	time between signal detection at multiple receivers [s]

$\delta_f$	fringe spacing [m]
$\delta_x$	probe volume length in x direction [m]
$\delta_y$	probe volume length in y direction [m]
$\delta_z$	probe volume length in z direction [m]
$\varepsilon$	turbulent energy dissipation
$\eta$	error in the population mean
$\eta_s$	ensemble mean
$\theta$	half the angle of intersecting laser beams
$\theta_b$	total angle of bend deflection
$\lambda$	wavelength [m]
$\lambda_L$	linear concentration in Ba
$\lambda_s$	constant in Prandtl's universal law of friction for smooth pipes
$\lambda_w$	linear concentration based on the solids concentration near wall
$\mu$	fluid viscosity [ $\text{kg m}^{-1}\text{s}^{-1}$ ]
$\mu_{\text{ef}}$	effective fluid viscosity [ $\text{kg m}^{-1}\text{s}^{-1}$ ]
$\mu_T$	turbulent eddy viscosity [ $\text{kg m}^{-1}\text{s}^{-1}$ ]
$v$	solids volume fraction
$v_0$	maximum solids volume fraction in Ba = 0.64
$\rho_f$	fluid density [ $\text{kg m}^{-3}$ ]
$\rho_m$	slurry density [ $\text{kg m}^{-3}$ ]
$\rho_s$	solid density [ $\text{kg m}^{-3}$ ]
$\sigma$	standard deviation
$\sigma_e$	ensemble standard deviation
$\sigma_s$	particle stress tensor
$\tau_f$	fluid shear stress

$\tau_m$	slurry shear stress
$\tau_s$	solid shear stress
$\Phi$	phase difference
$\varphi$	turbulence modulation parameter of Hosokawa and Tomiyama [25]
$\varphi_r$	angle of receiver
$\Psi$	angle created by the plane that bisects the two photo detectors in PDPA

Abstract of Dissertation Presented to the Graduate School  
of the University of Florida in Partial Fulfillment of the  
Requirements for the Degree of Doctor of Philosophy

BENCHMARK DATA AND ANALYSIS OF DILUTE TURBULENT FLUID-PARTICLE  
FLOW IN VISCOUS AND TRANSITIONAL REGIMES

By

Mark Pepple

May 2010

Chair: Jennifer S. Curtis  
Major: Chemical Engineering

The effects of flow rate and solids concentration of a liquid-solid flow consisting of water and glass spheres 0.5, 1.0, or 1.5 mm in diameter are varied to investigate the viscous, transitional, and collisional flow regimes in a vertical three inch pipe. The flow is highly turbulent, with single-phase  $Re$  from  $2.0 \times 10^5$  to  $5.0 \times 10^5$  and solids concentration from 0.7% to 3% by volume. These conditions span a wide range of Stokes and Bagnold numbers. Laser Doppler velocimetry is used to measure the mean and fluctuating velocities of the two phases simultaneously, while the phase Doppler method is used to measure particle size and thus discriminate between the phases. The detailed, non-intrusive velocity measurements under the conditions investigated provide a unique data set by which multiphase computational fluid dynamics (CFD) models can be validated.

For all particle sizes,  $Re$ , and solids concentrations the mean fluid velocity profile is very similar in shape to that of the single-phase fluid. The slip between the fluid and 0.5 mm particles is very small. The 1.0 mm particles exhibit an increase in slip as solids concentration increases. The fluctuating velocity measurements show trends characteristic of both collision-dominated and viscous-dominated flow, clearly showing

the flow is in a transitional regime. In all cases, the effects of changing the  $Re$  are greater than the effects of changing the concentration of solids. There is a reduction in turbulence of both phases across the pipe with increasing  $Re$ . However, at the highest  $Re$  there is an increase in both fluid and solid turbulence, which can be explained by an increase in vortex shedding at  $Re_p > 300$ .

The solid fluctuating velocity of the 1.0 mm particles is significantly greater than that of the 0.5 mm particles for all conditions. At each respective  $Re$ , the solids fluctuations for the 1.0 mm particles are greater than those of the fluid in their presence, except very near the wall where they become similar. Conversely, the solids fluctuations for the 0.5 mm particles are less than those of the fluid in their presence. The difference in turbulence between the two phases decreases with increasing  $Re$ .

The turbulence of both phases becomes increasingly flat near the center of the pipe with increasing  $Re$  and solids concentration. This is in agreement with the flat profiles of both fluid and solid turbulence in inertia-dominated gas-solid flows. In general, the 0.5 mm particles damp the fluid turbulence while the 1.0 mm and 1.5 mm particles are either neutral or enhance the turbulence. These data give insight into the fluid-particle interactions over a wide range of flow conditions.

## CHAPTER 1 INTRODUCTION AND BACKGROUND

### **Introduction**

Fluid-solid two-phase flows can be found in various settings including industrial processes (pneumatic/hydraulic conveying and fluidized bed reactors), natural phenomena (sand/sediment in oceans and other bodies of water), and biology (blood flow). Fluid-solid flows are found in the mining, chemical, oil, pharmaceutical, and food industries. Fundamental understanding of fluid-solid flows is necessary for the accurate design of pumps, pipelines, reactors, separation processes, heat exchangers, and any other operation involving fluid-solid materials. The presence of a solid-phase can have a significant impact on momentum, heat, and mass transfer and accordingly necessitates a fundamental understanding of fluid-particle interactions.

From an industrial perspective liquid-solid flows, or slurries, are typically classified as either settling or non-settling. This demarcation depends on particle density and size, fluid viscosity, and slurry velocity. Non-settling slurries are usually composed of particles  $\leq 100 \mu\text{m}$  and can be considered homogeneous. This homogeneity allows for the determination of an effective viscosity which is required for design of reacting and transporting operations. Settling slurries are comprised of two distinct phases and cannot be characterized by an effective viscosity. They have a minimum transport, or deposition, velocity and in horizontal pipes exhibit a non axisymmetric solids profile. The two phases that compose non-settling slurries interact; the solids can undergo direct collisions and also be influenced via the fluid. These interactions are often complex and are not fully understood.

This complexity results in significant challenges in the design, scale-up, and optimization of multiphase systems. These difficulties could be largely remedied by accurate predictive computer models. However, reliable simulation models do not exist, and consequently design is often based on large expensive physical models or other similar existing equipment. These methods are not reliable due to the complexity of multiphase systems and result in significant downtime for many two-phase operations (Merrow [1] and Bell [2]). The development of accurate computer models requires detailed experimental data by which the models can be verified. Model validation requires mean and fluctuating velocities of both phases and solids concentration profiles at varying flow rates and solids concentrations. These detailed measurements are vital to the development of constitutive relationships that link the solids motion and material properties with stress, kinetic energy production, and energy dissipation.

A non-intrusive measurement technique is essential for acquiring meaningful experimental data in multiphase flows. The solid-phase can damage intrusive measurement techniques and any intrusive device will inherently disrupt the flow. Laser Doppler velocimetry (LDV) has been used to obtain detailed velocity data in multiphase flows and jets for various particle sizes and Re, including gas-solid (Maeda et al. [3], Lee and Durst [4], Tsuji et al. [5], Sheen et al. [6], van de Wall and Soo [7], Jones [8], Hadinoto et. al. [9]), gas-liquid (Theofanous and Sullivan [10] and Wang et al. [11]), liquid-liquid (Hu et al. [12]), and liquid-solid (Zisselmar and Molerus [13], Abbas and Crowe [14], Nouri et al. [15], Alajbegović et al. [16], and Assad et al. [17]).

## **Background**

Fluid-particle flows can be categorized into two flow regimes. In cases where viscosity dominates, inter-particle momentum and energy transfer occur via the fluid.

Fluid-particle systems where the densities of the two phases are nearly equal, the solids are very small, or the flow rate is very low are typically in the macro-viscous regime. Alternatively, when particle collisions and particle inertia dominate, particles interact directly and transfer energy and momentum through direct collisions, unaffected by the interstitial fluid. This is known as the grain-inertia regime and is characteristic of flows of large particles with densities greater than the fluid. Between these two extremes, both collisional and viscous forces are significant.

Viscous-dominated flow typically includes gas-solid and liquid-solid flows with small particles. Additionally, liquid-solid flows that have low solid concentrations, low velocities, or a neutrally buoyant solid-phase also tend to be viscous-dominated flows, (Koh et al. [18], Averbakh et al. [19], Zisselmar and Molerus [13], and Nouri et al. [15]). Collision-dominated flows are usually gas-solid flows with larger and denser particles, and may include high velocities and high solids loadings, where solids loading are defined as the ratio of solid flux to fluid flux, (Tsuji et al. [5], Lee and Durst [4], and Sheen et al. [6]).

### **Stokes number**

Two common methods exist for qualifying particle forces in multiphase flows. The first is the Stokes number. According to Hardalupas et al. [20] the turbulent Stokes number can be used to describe a particle's responsiveness to fluid-phase turbulence fluctuations. Stokes numbers less than 1 characterize responsive particles while numbers greater than one are unresponsive—the particle fluctuating motion does not follow the fluid fluctuations. The turbulent Stokes number is defined as:

$$St = \frac{t_p}{t_f} \tag{1-1}$$

where  $t_p$  and  $t_f$  are the particle and fluid response times, respectively

$$t_p = \frac{d^2 \rho_s}{18\mu} \quad (1-2)$$

$$t_f = \frac{D}{U_f} \quad (1-3)$$

where  $U_f$  is the mean fluid velocity,  $D$  the pipe diameter,  $d$  the particle diameter,  $\rho_s$  the particle density, and  $\mu$  the fluid viscosity. The work of Simonin et al. [21] and Yamamoto et al. [22] suggest that particles with Stokes numbers larger than 1 will engage in particle-particle collisions, even at very low solids concentrations. Furthermore, these collisions have a significant influence on the solid fluctuating motion and the radial concentration profile.

### **Bagnold number**

The second common method of classification is the Bagnold number. Bagnold [23] defined two flow regimes, the macro-viscous and grain inertia regimes, with their differentiation defined by the Bagnold number which is a ratio of viscous and inertial forces

$$Ba = \frac{\rho_f d^2 \lambda_L^2 \gamma^2}{\mu \gamma \lambda^{3/2}} = \frac{\rho_f d^2 \lambda_L^{1/2} \gamma}{\mu} \quad (1-4)$$

where  $\rho_f$  is the density of the fluid and  $\gamma$  the shear rate, estimated as the mean fluid velocity divided by the pipe radius.  $\lambda_L$  is the “linear concentration” defined as:

$$\lambda_L = \left[ \left( \frac{v_0}{v} \right)^{1/3} - 1 \right]^{-1} \quad (1-5)$$

where  $v$  is the solids volume fraction and  $v_0$  the maximum solids concentration, which in the case of spheres is 0.64. Bagnold numbers greater than 450 are said to be

characteristic of flows dominated by solid-solid interactions and Bagnold numbers less than 40 are characteristic of viscous flow. Between these two numbers, both collisional and viscous forces are relevant and it is this region that is the focus of this research.

The 1954 work of Bagnold [23] in which he identified the “macro-viscous” and “grain-inertia” flow regimes has been critiqued extensively, with a complete review of his experiments offered by Hunt et al. [24]. Bagnold [23] stated that the rate of collisions and the momentum change per collision are both proportional to the shear rate and thus the stress is proportional to the square of the shear rate. Bagnold’s scaling has been observed numerically by Silbert et al. [25] for granular flow down an incline. However, Hunt et al. [24] argued that Bagnold’s [23] recorded shear stress measurements were influenced by the end walls of his rotational cylinder, effects Bagnold ignored in his paper. The experiments of Hunt et al. [24] resulted in a shear stress dependence on the shear rate to the 1.5 power rather than the second power. Furthermore, Hunt et al. [24] suggested that the changes Bagnold [23] identified as the macro-viscous and grain-inertia flow regimes were a change from a linear shear flow to a flow dominated by the boundary layer along the rotating end walls.

A further critique was offered by Wilson [26] who contended that data obtained from rotating cylinders can accurately predict dense flows with many particle collisions but is not suitable for predicting more dilute flows, like those often found in pipes, because there are fewer particle collisions. Admittedly, the exact numbers offered by Bagnold [23] for denoting his various flow regimes may not precisely describe slurry flow in a vertical pipe. However, this is not of concern. Both viscous and collisional forces exist in a two-phase flow and their relative magnitudes are examined and

manipulated in this work through the variation of fluid velocity and solids concentration. The experimental conditions investigated in this dissertation were selected such that they encompass both collision-dominated and viscous-dominated flows.

## **Mean Flow**

### **Collision-Dominated Flow**

There are more experimental data available for two-phase flows in the grain-inertia flow regime than the macro-viscous flow regime. This is due largely to the fact that phase discrimination and experimental access is easier in gas-solid flows which tend to be dominated by collisions. Some of the most significant gas-solid work in this flow regime include Maeda et al. [3], Tsuji et al. [5], Lee and Durst [4], Sheen et al. [6], Jones [8], and Hadinoto et al. [9] and in liquid-solid flow the work of Alajbegović et al. [16].

Tsuji et al. [5] utilized particles ranging in size from 200  $\mu\text{m}$  to 3 mm over a range of  $Re$  from  $1.6 \times 10^4$  to  $3.3 \times 10^4$ . In all cases the flow was in the collisional regime, though the smallest particles were nearing the lower limit, according to the Bagnold number. The large particles were found to have a minor flattening effect on the mean fluid flow. However, the smaller particles (500  $\mu\text{m}$  and 200  $\mu\text{m}$ ) created a concave fluid velocity profile—the maximum velocity was located away from the pipe center—in addition to an overall flattening of the profile. The mean velocity profile of the particles was flat except in the case of the 200  $\mu\text{m}$  particles which continued to show some curvature. Sheen et al. [6] and Maeda et al. [3] also found concave velocity profiles for both phases. Sheen et al. [6] observed concave velocity profiles for both phases with polystyrene particles ranging in size from 225  $\mu\text{m}$  to 675  $\mu\text{m}$  at  $Re$  of approximately  $2.7 \times 10^4$ , with the degree of concavity increasing with solids loading. Concavity was not found for 800  $\mu\text{m}$  particles.

Hardalupas et al. [20] investigated the effects of particle loading on relative slip velocities in a gas-solid jet at constant  $Re$  and found that the slip velocity decreased with increasing solids loading. Kulick et al. [27] examined the influence of particle density in gas-solid channel flow at constant  $Re$  and found that changes in particle density did not affect the mean fluid velocity. Sheen et al. [6] found that the particle mean velocity lagged that of the fluid for all cases and all locations except for the smallest particles ( $275 \mu\text{m}$ ) near the wall—in which case the negative slip velocity increased with increasing solids loading. This phenomenon was also observed by Lee and Durst [4] for  $100 \mu\text{m}$  and  $200 \mu\text{m}$  glass spheres at  $Re = 1.3 \times 10^4$ . The relative size of this region decreased with increasing particle size such that it was not observed for  $400 \mu\text{m}$  and  $800 \mu\text{m}$  particles by Lee and Durst [4] nor Maeda et al. [3] for  $475 \mu\text{m}$  and larger particles.

Jones [8] investigated gas-solid flow with solids loadings up to 30 with glass spheres  $70 \mu\text{m}$  and  $200 \mu\text{m}$  in diameter and found the fluid mean velocity became flat and then mildly concave with increased solids loading. However, no concavity was noticed in the solids mean velocity. The slip velocity between the two phases was found to decrease with increasing solids loading and increase with increasing  $Re$ . Hadinoto et al. [9] found that the fluid mean velocity became increasingly flat with increasing  $Re$  for  $200 \mu\text{m}$  particles, but not for  $70 \mu\text{m}$  particles. The larger particles are clearly in a collisional regime, while the smaller particles are in, or approaching, the transitional flow regime, depending on the  $Re$ . Hadinoto et al. [9] also showed that the slip velocity decreased with increasing  $Re$  for both particle sizes at a constant solids concentration.

In liquid-solid flow, Alajbegović et al. [16] found that on average the slip velocity decreased and the point at which the slip velocity went to zero moved toward the center of the pipe with increasing mass flux. The decrease in slip velocity with increasing  $Re$  was opposite that reported by Jones [8]. Hosokawa and Tomiyama [28] used LDV to measure the mean and fluctuating velocity of 1, 2.5, and 4 mm ceramic particles at two solids loadings in water at  $Re = 1.5 \times 10^3$  in a 30 mm diameter pipe. Under these conditions the Bagnold number varied from approximately 70 to 1200. However, insufficient data were presented to establish trends in the transitional flow regime and the fluid velocity in the presence of the solid was not measured. They found a decrease in the flattening of the mean solid velocity profile with increasing particle size and loading.

To summarize, at the level of mean velocity, the solid velocity is relatively flat with the degree of flatness increasing with particle size, density, and loading. The mean fluid velocity in the presence of small particles has been found by some to be concave to various degrees—with the maximum fluid velocity occurring away from the pipe center. The concavity increases with solids loading and decreases with increasing particle size. The mean fluid velocity has been found to be greater than the mean solids velocity across the majority of the pipe—from the center to near the wall. As the wall is approached the slip velocity decreases such that the solid velocity exceeds that of the fluid. The magnitude of the slip velocity increases with increasing particle size and density, causing the location of the slip velocity sign change to move closer to the wall. The slip velocity decreases with increasing solids loading and  $Re_p$ . At constant particle size, density, and loading, increasing the  $Re$  results in increased flattening of the mean

fluid velocity profile for sufficiently large particles. The mean solid velocity also becomes increasingly flat with increasing Re. See Table 1-1 for a summary of these trends in the flow behavior.

### **Viscous-Dominated Flow**

Only a limited amount of the turbulent liquid-solid experimental data captures both the solid velocity in the presence of the fluid and the fluid velocity in the presence of the solid. More commonly, the solid velocity in the presence of the fluid is compared to the single-phase fluid velocity, for example Chemloul and Benrabah [29]. Other liquid-solid experiments matched the index of refraction of the two phases and are thus only able to give solid-phase velocities (Zisselmar and Molerus [13] and Abbas and Crowe [14]). In addition to matching the index of refraction of the two phases, the densities are also often matched, Nouri et al. [15], Averbakh et al. [19], Koh et al. [18], and Lyon and Leal [30]. In the cases where the densities are matched no slip velocity is observed. Where a slip velocity is expected to be present, it is often redefined as the difference in solid velocity and single-phase fluid velocity at a constant volumetric flow rate. This modified slip velocity has been shown to decrease with increasing flow rate.

Nouri et al. [15] used 270  $\mu\text{m}$  particles and matched their index of refraction to the liquid at solids concentrations up to 14% in a pipe at  $\text{Re} = 3.965 \times 10^4$ . The mean particle velocity was found to be greater than that of the single-phase liquid and became increasingly flat with increasing solids concentration. However, they did observe that the mean particle velocity profile shape changes with particle concentration; the particle velocity peaked at the centerline at low solids concentration and then decreased with increasing solids concentration.

Abbas and Crowe [14] looked at silica gel particles 96  $\mu\text{m}$  and 210  $\mu\text{m}$  in diameter at solids concentrations up to 30% by volume at  $Re$  from  $1.2 \times 10^3$  to  $3.0 \times 10^4$ . At  $Re < 2.4 \times 10^3$  the solids profile remained parabolic—corresponding to laminar flow—regardless of solids concentration. At  $Re > 2.4 \times 10^3$  the solids profiles were characteristic of turbulent flow.

Koh et al. [18] and Lyon and Leal [30] used small particles (70  $\mu\text{m}$  and 95  $\mu\text{m}$ ) and low flow rates ( $< 0.1$  m/s). Their single-phase experiments exhibited the expected parabolic profile of laminar flow. This profile remained for the smaller particles at the lowest flow rate, but became progressively flat with increasing particle diameter and solids concentration. The mean solid velocity profile for a given particle concentration did not change with changes in the flow rate.

Mishra et al. [31] measured the mean velocity and solids concentration profile for copper tailings in water in a 4 inch horizontal pipe at flow velocities between 1.67 and 2.95 m/s and solids concentrations between approximately 1% and 4.5% by volume. They found that the mean solid velocity profile was largely independent of flow rate and solids concentration. Despite the high density particles, the slurry was clearly in the viscous flow regime because the average particle size was only 71  $\mu\text{m}$ . Additionally, they used an intrusive impact probe to make their measurements.

Kiger and Pan [32] used particle image velocimetry (PIV) to measure mean and fluctuating velocities of 200  $\mu\text{m}$  glass particles in a horizontal water channel at  $Re = 9.6 \times 10^3$ , developing an image separation technique to distinguish between the two phases. The mean particle velocity lagged the fluid, most noticeably in the middle of the profile. Chemloul and Benrabah [29] obtained mean velocities of water and glass

spheres (0.5 mm and 1.0 mm in diameter) in a vertical pipe and found that the slip velocity decreased with increasing Re for a given particle size and concentration—a trend opposite that found by Jones [8] but inline with the results of Alajbegović et al. [16]. The slip velocity was also the greatest at the pipe center and decreased across the pipe. The mean solids profile became increasingly flat with increasing solids concentration. See Table 1-2 for a summary of these trends in the flow behavior.

## **Turbulence Modulation**

### **Collision-Dominated Flow**

Of greater importance than the mean velocity profile is how the presence of a second phase affects the turbulence of the fluid. This effect is known as turbulence modulation. Typically, a flatter mean velocity profile corresponds with a flatter turbulence profile—the turbulence energy is spread out. However, whether the dispersed phase increases or decreases the magnitude of fluid turbulence depends on a number of factors. Furthermore, the solid-phase turbulence is related to the solids concentration profile and mean velocities.

Maeda et al. [3] found an increase in two-phase fluid-phase turbulence intensity for all particle sizes examined, 45 to 136  $\mu\text{m}$  at  $\text{Re} = 2.0 \times 10^4$ . Lee and Durst [4] investigated larger particles and found an increase in fluid-phase turbulence intensity with 800  $\mu\text{m}$  particles at  $\text{Re} = 8.0 \times 10^3$ . Tsuji et al. [5] found fluid-phase turbulence enhancement for larger particles and turbulence damping for smaller particles, with an increase in the corresponding affect with increasing solids loading. Kulick et al. [27] found that fluid fluctuations were damped by the particles, with greater damping by the 50 and 90  $\mu\text{m}$  glass particles than the 70  $\mu\text{m}$  copper particles. Hadinoto et al. [9]

studied the effect of Re on 70  $\mu\text{m}$  and 200  $\mu\text{m}$  glass particles and found that for both particles, the normalized fluid-phase fluctuations increase with increasing Re.

Hadinoto et al. [9] also found that the normalized solid-phase fluctuations decrease with increasing Re. Alajbegović et al. [16] found a flat solid-phase turbulence profile at low mass flow rates that became less flat with increasing mass fluxes for both ceramic and polystyrene particles. Indeed, there was little change in the magnitude of the solid-phase turbulence near the pipe center with changes in flow rate. However, Alajbegović et al. [16] varied both the solids loading and Re in each experimental, making qualification of the results difficult. Furthermore, the single-phase fluid turbulence was not included in the comparison with the two-phase fluid-phase turbulence plots making turbulence enhancement or damping speculative. Hosokawa and Tomiyama [28] found that the solids fluctuating velocity increased with both increasing particle size and solids loading. See Table 1-3 for a summary of these trends in the flow behavior.

### **Viscous-Dominated Flow**

Liu and Singh [33] offer the only turbulence data of both phases simultaneously, but did not conduct a thorough investigation of variables. In general they found that the particles, < 200  $\mu\text{m}$  in diameter, damped the turbulence in comparison with single-phase flow. The magnitude of the solid-phase turbulence was similar to the liquid-phase turbulence, except at the center where the solid fluctuations were approximately 30% greater. However, their maximum solids concentration was 0.5% by volume and the maximum Re was  $2.0 \times 10^4$ .

Other experimental work only compares the solid fluctuations to the single-phase liquid fluctuations. Zisselmar and Molerus [13] found that 53  $\mu\text{m}$  particles damped the

turbulence with respect to the single-phase away from the wall. In these cases the solid fluctuations have been found to decrease with increasing solids loading in some cases (Nouri et al. [15] and Chemloul and Benrabah [29]) while in others the solids fluctuations were found to be independent of solids loading except near the wall where they increased with solids loading (Lyon and Leal [30]). Nouri et al. [15] and Chemloul and Benrabah [29] both used larger particles in comparison with Lyon and Leal [30]. Nouri et al. [15] showed that the solid-phase turbulence decreased with increasing solid diameter, for neutrally buoyant particles. The particle fluctuating velocity was found to be less than that of the single-phase liquid, with the difference increasing with increasing solids loading.

At a constant solids concentration of 20% Abbas and Crowe [14] found that the centerline axial turbulence intensity increased with particle diameter (96  $\mu\text{m}$  and 210  $\mu\text{m}$ ) and slightly with Re for a non-neutrally buoyant particle. Kiger and Pan [32] found an increase in fluid fluctuating velocity in the axial direction in the presence of their solid-phase on the order of 10% across the bulk of the channel. Near the wall the fluid fluctuations were damped ( $y^+ < 30$ ) or were not significantly influenced ( $30 < y^+ < 100$ ) by the solid-phase. The solid-phase fluctuations exceeded the fluid phase in the center region of the channel ( $y/h > 0.4$ ) but were less than the fluid closer to the wall;  $y/h < 0.4$ . See Table 1-4 for a summary of these trends in the flow behavior.

### **Turbulence Modulation Correlations**

In an attempt to understand and summarize the increasing amount of turbulence modulation data, Gore and Crowe [34] and Hetsroni [35] examined available experimental data—mainly gas-solid and gas-liquid but also liquid-solid. Gore and Crowe [34] concluded that the particle diameter was the determining factor on the

turbulence modulation in a two-phase flow. The ratio of particle diameter to the characteristic length of the most energetic eddy in single-phase flow was identified as the criteria for turbulence enhancement or dampening. The length of the most energetic eddy was defined by Hutchinson et al. [36] as ( $l_e \approx 0.2R$ ). When this ratio was greater than 0.1 turbulence is enhanced by the solid-phase and conversely a ratio of less than 0.1 would result in turbulence dampening. Small particles would follow the most energetic eddies and thus diminish their energy while larger particles would create vortices in their wakes thus increasing the fluid turbulence. Crowe [37] went on to argue that increasing the amount of solids present in the flow would augment the particle-diameter dependent turbulence modulation—be it enhancement or suppression.

Hetsroni [35] also surveyed available experimental data and argued the particle Reynolds number determined the turbulence modulation:  $Re_p$  greater than about 400 enhanced turbulence. The particle Reynolds number is defined as

$$Re_p = \frac{du_r \rho_f}{\mu} \quad (1-6)$$

where  $u_r$  is the absolute value of the slip velocity. The work of Sheen et al. [6] corroborated the findings of Gore and Crowe [34] while exhibiting the turbulence modulation described by Hetsroni [35] at  $Re_p \geq 100$ . They reasoned that the slip velocity increased with increasing particle size, thus increasing vortex shedding and turbulence enhancement. Furthermore, because the slip velocity in the radial direction is minimal, radial turbulence damping will occur for all particles, regardless of particle size.

Hosokawa and Tomiyama [28] contend that the ratio of eddy viscosity of the two-phase flow to that of an analogous single-phase flow is an appropriate parameter to

correlate turbulence modulation—with no modulation occurring at unity. Their parameter,  $\phi$ , is the product of that offered by Gore and Crowe [34] with the ratio of turbulence intensity caused by the dispersed phase to that caused by shear:

$$\phi = \frac{u_r d}{u'_t l_e} \quad (1-7)$$

where  $u'_t$  the shear induced turbulence in single-phase flow. The additional terms appeared to refine the scatter of data in comparison to that proposed by Gore and Crowe [34]. However, as clearly shown by Hadinoto et al. [9], the correlations espoused by Gore and Crowe [34] and Hetsroni [35] are insufficient. The present data will offer additional insight into turbulence modulation under conditions not previously investigated.

### **Radial Solids Concentration Profile**

The radial concentration of the solid-phase also changes with flow conditions and is related to the turbulence and mean flow profiles. Typically, a greater number of particle collisions will occur in regions of higher solids density; which in turn decreases the solids fluctuating velocity through energy dissipation via inelastic collisions. In collision-dominated flow at low flow rates and solids concentrations, the radial concentration profile is relatively flat—the solids are evenly distributed across the pipe. As the flow rate or solids loading increases, the solids move toward the center of the pipe—such that areas near the pipe wall have been found void of particles (Maeda et al. [3], Lee and Durst [4], and Alajbegović et al. [16]). Mishra et al. [31] found that the solids moved from the wall toward the center of the pipe, making the distribution more uniform as the flow rate increased—at low flow rates a high density of particles were present in the bottom of the pipe. Similar to collision-dominated flow, Koh et al. [18] and

Lyon and Leal [30] found that the radial solids concentration profile shows increased solids in the center of the channel with increasing solids concentration. The concentration profile is not affected by particle size (Lyon and Leal [30], at 50% solids).

### **Two-Phase Flow Measurement Techniques**

There is a void of non-intrusive data that captures both liquid velocities in the presence of solids and solid velocities in the presence of the fluid for flows in the transitional flow regime. The effects of particle size, particle concentration, inlet flow conditions, flow geometry and other variables on the two-phase flow need to be determined. In addition, constitutive relationships that link the turbulent stress, kinetic energy, and energy dissipation to the solids motion and material properties are needed. Thus, the mean velocity and fluctuations of both phases need to be measured simultaneously.

Intrusive measurement techniques like hot-wires, pitot tubes, and isokinetic probes have been used extensively and have shown some success in many fluid-mechanical systems. However, these methods are known to disturb the flow around the point of data collection. Hot-wires and pitot tubes are not able to discriminate between solid and liquid velocity and require calibration. Isokinetic probes provide local concentration data but do not measure velocity. Additionally, the solid-phase can damage intrusive measurement devices. Chaouki et al. [38] surveyed noninvasive measurement methods which rely on either radioactive or optically active particles. Nuclear particle tracking techniques offer limited spatial resolution at high flow rates,  $> 2\text{-}3$  m/s. High speed cameras have also been used to capture solid-phase velocity and solid profiles in two-phase flows, but because the particles must be counted, this technique is laborious and only suitable for very dilute flows (Sakaguchi et al. [39]). Capacitance probes and

Gamma rays have also been used to measure average radial densities in pipes, but are not capable of measuring particle velocities.

Non-intrusive laser based techniques offer the best combination of temporal and spatial resolution. Particle image velocimetry (PIV) creates a laser plane and captures a cross section of the flow, calculating average velocity vectors by measuring particle displacement between consecutive light pulses. PIV has the ability to measure an entire plane simultaneously but LDV offers better temporal and spatial resolution. Additional complimentary features have been added to PIV which allow for particle sizing and/or phase discrimination, particle tracking via planer laser induced florescence (PIV/PLIF), and particle sizing via a global sizing velocimeter (GSV). Both of these techniques and nuclear magnetic resonance (NMR) have some of the needed abilities, but are limited in particle sizing, resolution, and introduce additional complications for large experiments.

Laser Doppler velocimetry, when used in conjunction with phase discrimination, provides the required mean and fluctuating velocities of both phases. When the velocity difference between the two phases is large enough, two distinct velocity peaks can be obtained, making phase discrimination simple. This is typically the case in gas-solid flows. This method does not work when the two phases' respective velocity histograms overlap—as is often the case in liquid-solid flows. Several in-house techniques have been used to discriminate LDV data in these cases. For example the transit-time method of Alajbegović et al. [16], the discriminator LDV of Muste et al. [40], and the laser Doppler split-phase measuring technique of Liu and Singh [33]. The transit-time

method of Alajbegović et al. [16] was attempted but not found to be reliable. The latter two methods involve significant additional signal processing.

A significantly more established and commercially available method is phase Doppler anemometry (PDA or PDPA), which measures the size of spherical particles. Each particle measurement contains both size and velocity data, making discrimination based on size straight forward. The availability and demonstrated reliability of the LDV/PDA technique made it the instrument of choice.

PDPA has also been used to estimate the radial solids concentration profile in two-phase flows. This method, and its errors, has been the subject of several papers and will be addressed in more detail in Chapter Two. The large particle size, relatively low solids concentration, and highly one-dimensional flow are advantageous conditions for concentration profile measurements with PDPA. However, the large pipe radius requires a significant penetration depth which results in significant signal attenuation. Finally, the sampling of the entire flow to determine the overall solids concentration allows for verification of the PDPA result. Thus, the present work also examines the validity of PDPA solids flux measurements.

### **Two-Phase Flow Modeling**

There exist many avenues for modeling multiphase systems. The most important factor in determining the best method is the  $Re$ . When the  $Re$  is very small viscous models can be used to model fluid-particle systems. For example, Stokesian dynamics (Brady and Bossis [41]) gives very accurate solutions for spheres with no appreciable inertia. Each particle has an equation of motion which includes fluid forces, but there is no explicit equation for fluid motion. Stokesian dynamics is not inherently restricted by particle size, but as soon as any inertial forces become significant the simulation is no

longer valid. Analogous models can be formulated for particles of other shapes. These models can be used to determine macroscopic behavior from microscopic material properties and mechanics. Brownian dynamics is a simplified form of Stokesian dynamics and has been widely used to simulate the settling of particles in a quiescent fluid (Brady and Bossis [41]). Stokesian Dynamics utilizes a more robust description of hydrodynamic forces and is consequently often used in shear flows (Brady and Bossis [41]). Although potentially very accurate, these viscous models are limited to systems with no inertial forces and total particles on the order of  $10^3$ . Consequently, a different kind of model is needed to predict the behavior of a liquid-solid flow where both viscous and inertial forces are significant.

Inertial models can be categorized as either Eulerian or Lagrangian. Lagrangian models solve an equation of motion for each particle in the system, tracking their interactions in a specific geometry. A major advantage of the Lagrangian method is that each particle can have its own physical properties—size, shape, and density. However, the scope of simulations is limited by the number of particles in the system. The discrete element method (DEM) is an example of Lagrangian principles and has been used to model a wide range of systems. When the particles simulated are large and dense in comparison with the surrounding fluid and their mean flow is not driven by a fluid, dry (no fluid) particle simulations are sufficient. When viscous forces become significant, the Lagrangian method can include fluid forces or be coupled with traditional computational fluid dynamic (CFD) models. This later technique is known as the Eulerian-Lagrangian method. However, the limitations in terms of number of particles that restrict traditional Lagrangian methods remain in Eulerian-Lagrangian models

To overcome this restriction the particles can be treated as a continuum. When this approach is utilized it is known as a two-fluid or simply an Eulerian model. The advantages of this approach are its ability to handle an infinite number of particles and be applied to any geometry. It is also significantly less computationally expensive to model large systems than when individual particles are considered. However, because the solids are treated as a continuum, equations of motion for the fluid and solid-phases are based on the seminal work of Anderson and Jackson [42], and individual particle characteristics are ignored and replaced by volume averaged quantities. Stress in the solid-phase can be described in various ways, though the most popular method is the kinetic theory of granular flow. This theory utilizes a granular or pseudo temperature energy balance equation, similar to the thermal temperature in gas molecules, to describe the behavior of the solid-phase fluctuations. Particle-particle and particle-wall collisions are described by a coefficient of restitution.

Two fluid models have successfully simulated a variety of multiphase flows including gas-solid, gas-liquid, liquid-solid, and liquid-liquid, and have been applied to two and three dimensions. An Eulerian model's ability to capture both viscous and collisional forces without restraint on the number of particles makes it the ideal method for simulating flows of practical interest.

### **Motivation**

There is clearly a dearth of detailed, non-intrusive experimental data for a two-phase flow in the viscous-dominated and transitional flow regimes. A systematic investigation into the effects of  $Re$ , particle size/density, and solids concentration on both mean and fluctuating velocities and radial solids concentration profiles is needed. Additionally, there is no data for liquid-solid two-phase flows at  $Re > 5 \times 10^4$ . Therefore,

it is the intent of this dissertation to present mean and fluctuating velocity data for a two-phase flow at  $Re$  between  $2.0 \times 10^5$  and  $5.0 \times 10^5$ . Furthermore, we will show a transition from inertial flow dominated by particle collisions to a viscous-dominated flow regime.

The experimental data can be used to validate a computer model. Figure 1-1 is representative of the inability of current state-of-the-art multiphase flow models, which neglect lubrication effects, to capture pressure drop in fluid-solid flows in the transitional flow regime. In Figure 1-1A the model accurately predicts the pressure drop for the large 200  $\mu\text{m}$  particles. As the particle diameter decreases viscous effects become more significant and the model over predicts the pressure drop (Figure 1-1B). By manipulating experimental conditions to map the transition from collision-dominated to viscous-dominated flow, the present data provides a standard by which future models can be assessed.

Table 1-1. Mean velocity behavior for collision-dominated flow

	Increasing Particle Diameter, d	Increasing Particle Density, $\rho_s$	Increasing Solids Concentration, v	Increasing Re
Fluid	Maximum away from center with small particles, with effect decreasing with increasing d	No effect	Conflicting	Increasing flatness
Solid	Increasing flatness	Increasing flatness	Increasing flatness	Increasing flatness
Solids Conc. Profile	Conflicting		Flat at low concentrations, move toward center with increasing v	Flat at low Re, move toward center with increasing Re
Slip Velocity	Increase	Increase	Decreases	Conflicting

Table 1-2. Mean velocity behavior for viscous-dominated flow

	Increasing Particle Diameter, d	Increasing Particle Density, $\rho_s$	Increasing Solids Concentration, v	Increasing Re
Fluid	Not yet studied	Not yet studied	Not yet studied	Increasingly flat
Solid	Increasing flatness	Increasing flatness	Increasing flatness	Independent
Solids Conc. Profile	No Effect	Not yet studied	Conflicting	Solids become more evenly distributed
Slip Velocity	Increases	Increases	Increases	Decreases

Table 1-3. Fluctuating velocity behavior for collision-dominated flow

	Increasing Particle Diameter, $d$	Increasing Particle Density, $\rho_s$	Increasing Solids Concentration, $v$	Increasing Re
Fluid	Increases	Increases	Increases or Decreases; Effect of particles is augmented	Increases
Solid	Increases	Increases near wall	Increases	Increases near wall

Table 1-4. Fluctuating velocity behavior for viscous-dominated flow

	Increasing Particle Diameter, $d$	Increasing Particle Density, $\rho_s$	Increasing Solids Concentration, $v$	Increasing Re
Fluid	Decrease	Little Change	Decrease	Decreases
Solid	Decreases (neutrally buoyant) increases	Decrease	Conflicting	Increases

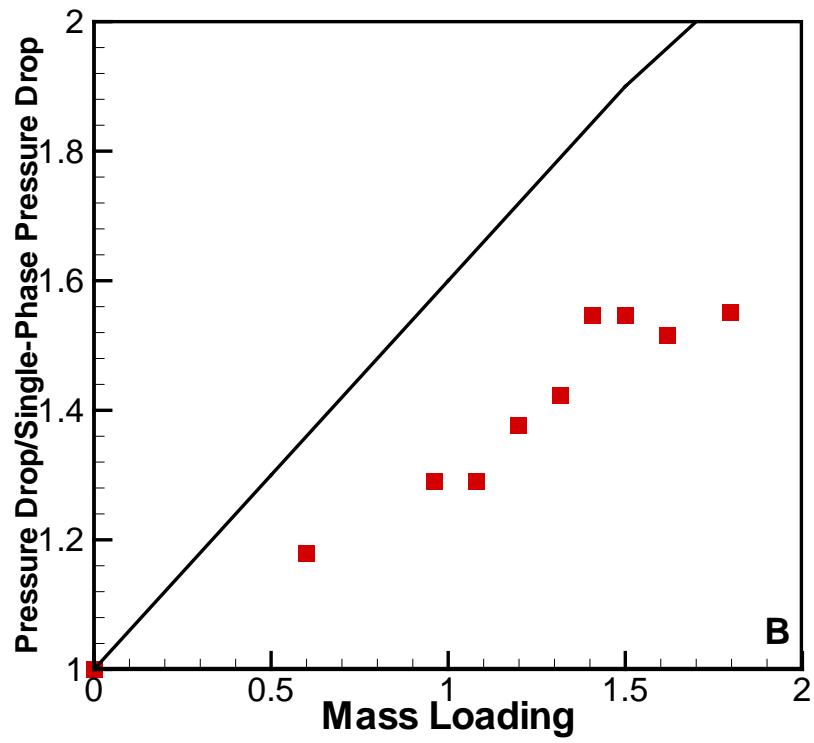
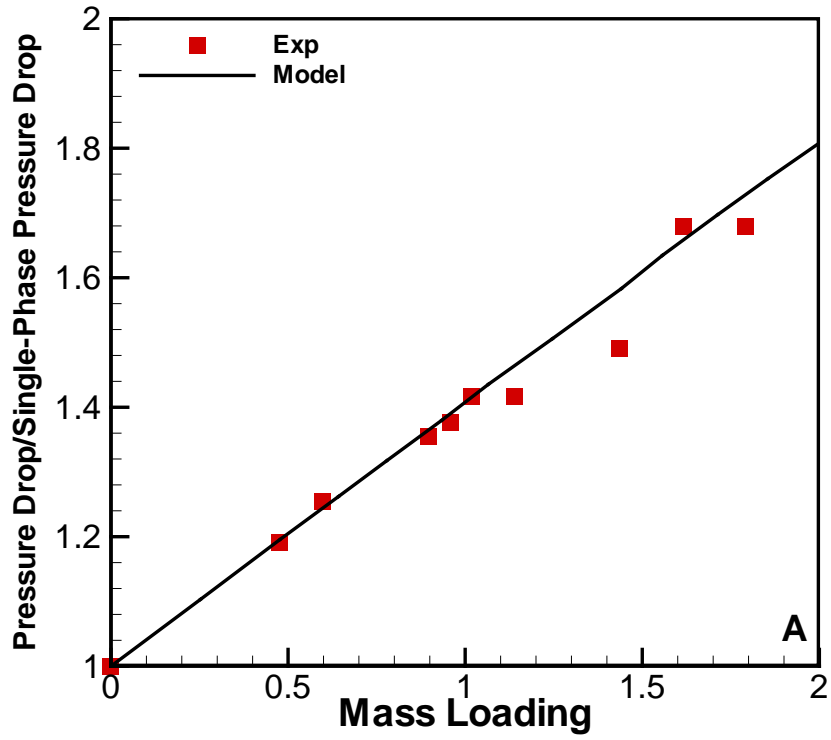


Figure 1-1. Gas-solid pressure drop. A)  $d = 200 \mu\text{m}$  and B)  $d = 70 \mu\text{m}$

## CHAPTER 2 EXPERIMENTAL SETUP AND METHODS

### **Experimental Setup**

The experiments were conducted in a pilot-scale flow loop which allowed for the study of the effects of particle concentration and slurry velocity on vertical fully developed turbulent pipe flow. A diagram of the flow loop can be seen in Figure 2-1. The setup was designed in-house and much time was devoted to ensuring the accuracy and precision of the experimental measurements.

The loop was constructed from nominal 3 inch (78 mm) schedule 40 type 304 stainless steel. The flow was driven by a 50 hp centrifugal pump and controlled by a variable frequency drive (ABB model number ACH550-UH-072A-4), which allowed for flow control with reproducibility error less than 2% by volumetric flow rate at all speeds. The flow could be controlled from a minimum at the particle deposition velocity to a maximum of over 8 m/s (at this velocity the jet within the venturi was removed). An electromagnetic flow meter gave a volumetric flow rate and was used to reproduce flow conditions. The water in the system was replaced approximately once a month during experiments. The optical purity of the water decreased over time due to the presence of dirt, dust, and other small matter in the room housing the flow loop.

The large size, 0.5 mm to 1.5 mm, of the particles necessitated their removal from the flow prior to the pump and re-introduction post pump. Separation was achieved by gravity and entrainment via a venturi eductor, see Figure 2-2. The increased velocity caused by the jet on the entrance side of the eductor induces a low pressure region that entrains the flow from above. Opening the eductor introduced the solids into the flow while closing the eductor resulted in their collection in the pipe below the particle

separator. The loop could be operated in single-phase and two-phase conditions. Two-phase conditions were defined by the presence of the 0.5, 1.0, or 1.5 mm particles at any concentration greater than approximately 0.01% by volume. For experiments at  $Re > 5.0 \times 10^5$ , based on pipe diameter and mean fluid velocity, the particles were removed from the system and the jet nozzle of the eductor was removed. Removing the nozzle reduced the pressure drop across the eductor making the operation more efficient. Furthermore, a longer pipe at the point of discharge into the particle separator was used for single-phase experiments at  $Re > 5.0 \times 10^5$ . The longer pipe was submerged in the particle separator making flow smoother and reducing splashing. See Chapter Four for more details.

The cylindrical test section was made of borosilicate glass with a wall thickness of 4.75 mm and was 12 pipe diameters (0.91 m) in length with an ID of 76 mm. The liquid entered the test section after traveling 51 vertical pipe diameters. The measurements were then taken approximately 1 diameter below the end of the test section, allowing for a total of 62 diameters for the flow to become fully developed. The small diameter difference (2.0 mm) between the nominal 3 inch schedule 40 pipe and the glass test section created a small increase in the turbulence at the wall immediately after their connection. This increase in turbulence was mapped vertically with the LDV and was found to dissipate within a few pipe diameters.

Pressure taps were placed every 5 diameters along the vertical steel pipe. The pressure taps were 1.0 mm in diameter. Threaded couplings were welded over the holes and pressure gauges were screwed into the couplings. The pipe wall thickness was over 5 times the tap diameter, so the water in contact with the gauge was assumed

to be quiescent, see Figure 2-3. The gauges (CeComp model DPG1000B15PSIG-5-HA) had a range of 0–15 PSI (0–103 kPa) with an accuracy of  $\pm 0.1\%$  of the full scale. The pressure distribution was measured at each flow rate and provided one of two methods used to verify fully developed flow. The second method required comparing fluctuating velocity profiles at varying developmental lengths. Axisymmetric flow was also verified by comparing fluctuating velocity profiles at differing azimuthal locations. Fully developed and axisymmetric flow was verified for both single and two-phase flows at a single flow rate.

The solids concentration in the slurry was determined by sampling approximately 50 gallons of the entire flow. After a series of experiments, the valve on the bottom of the small tank on top of the particle separator was closed. Once the tank was appropriately full, the three-way valve was adjusted, routing the flow around the tank. The tank was calibrated such that the total volume could be determined by the height of slurry in the tank. The water was then drained and the particles were collected, dried in an oven, and weighed. Based on the particle density a particle volume and solids volume concentration was determined. The total volume sampled was ensured to be less than the minimum well-mixed slurry in the loop. This minimum volume was estimated by assuming the particle separator was a continuation of the nominal 4 inch pipe used from the particle separator to the eductor—a volume of approximately 110 gallons. The solids that were removed were then added back into the loop to ensure a constant solid concentration. This method proved to be very reliable once the minimum fluidization velocity was obtained.

The friction velocity was needed to validate single-phase flow and was determined from the pressure drop with

$$U_t = \sqrt{\frac{\left(\frac{dP}{dz} - \rho_f g\right) R}{2\rho_f}} \quad (2-1)$$

where R is the pipe radius, g gravity, and  $\rho_f$  the fluid density. See Figure 2-4 for a detailed diagram of the vertical pipe. This value was also compared with the friction velocity calculated through wall shear-stress measurements via law-of-the-wall correlations—similar to a Clauser Chart (Tavoularis [43])

$$\log \frac{y\rho_f u}{\mu} = \frac{1}{A} \left( \frac{u}{U_t} - B \right) + \log \frac{u}{U_t} \quad (2-2)$$

where u is the velocity at point y in the logarithmic sublayer, B=5.0, and A = ln (10)/k =5.9. Additionally, these two values were compared with that obtained through Prandtl's universal law of friction for smooth pipes (Prandtl [44]):

$$\frac{1}{\lambda_s} = 2.0 \log \left( \frac{U_f D \rho_f}{\mu} \sqrt{\lambda_s} \right) - 0.8 \quad (2-3)$$

where  $U_f$  is the mean (bulk) velocity, D the pipe diameter, and  $\lambda_s$  is related to the friction velocity by

$$U_t = \sqrt{\frac{\lambda_s U_f^2}{8}} \quad (2-4)$$

The three methods produced values of  $U_t$  that were within 10% at  $Re = 5.0 \times 10^5$ . Laser Doppler velocimetry (LDV) was used to measure the liquid velocities.

### Experimental Particles

For the two-phase experiments the particles were 1.0 mm and 0.5 mm glass (borosilicate) spheres purchased from Mo-Sci and 1.5 mm glass (borosilicate) spheres

purchased from Jay-go. Photographs of the three sets of particles can be found in Figure 2-5. The particle size distributions were 0.4 - 0.6 mm, 0.8 - 1.2 mm, and 1.3 – 1.7 mm for the 0.5, 1.0, and 1.5 mm particles, respectively. The particles were highly spherical and reflected light very well. The difference in refractive index of the liquid and solid-phase was sufficient for the Phase Doppler Particle Analyzer (PDPA) to accurately measure particle diameter.

Seed particles were added to increase the visibility of the liquid-phase. The seed particles were 10  $\mu\text{m}$  silver coated hollow glass spheres, designed for liquid laser Doppler applications and purchased from Dantec Dynamics. A number of seed particles were tried with the above particles proving to be the best. Light incident on a transparent particle will undergo both reflection and refraction, while a highly reflective opaque particle will reflect the vast majority of the incident light. Utilizing the Mie-Parameter

$$\chi_M = \frac{\pi d}{\lambda} \quad (2-5)$$

where  $d$  is the particle diameter and  $\lambda$  the wavelength of light, particles with  $\chi_M > 10$  scatter light proportional to the square of the particle diameter, Albrecht et al. [45]. For the seed particles  $\chi_M = 61$ . Since the diameter of the dispersed phase particles are nearly two orders of magnitude greater than the seed particles, a highly reflective seed particle was needed due to the large amount of light scattered by the dispersed phase.

Using equations 1-1 through 1-3, the 1.0 mm glass particles had a response time of approximately 0.14 seconds while the fluid response time ranged from approximately 0.076 to 0.015 seconds, yielding Stokes numbers between 1.9 and 9.5. The response

time of the 10  $\mu\text{m}$  particles was on the order of  $10^{-6}$  seconds which clearly shows the seed particles will follow the fluid.

## **Laser Doppler Velocimetry**

### **Basic principles**

LDV is a non-intrusive, laser-based, technique capable of making instantaneous and time-averaged velocity measurements with high spatial resolution (Albrecht et al. [46]). LDV is based on the Doppler Effect—the phenomenon whereby the frequency of a wave is dependent on the velocity of the wave source and/or point of observation. An acoustic example of the Doppler Effect is the sound from a siren on an ambulance increases in frequency as it approaches and decreases as it becomes farther away. This effect can be utilized to determine the velocity of the wave, given other parameters. Multiple configurations of LDV have been successfully demonstrated, including systems with one laser beam and two scattering angles or a reference-beam. However, the most prominent arrangement consists of crossing two beams of equal intensity—with one or more receivers (Albrecht et al. [46]).

Typically, a single beam of coherent laser light is split into two beams using a beam splitter with one beam undergoing a frequency shift via a Bragg-cell. A Bragg-cell is an acousto-optic modulator that shifts the frequency of light using sound waves. An oscillating electric signal activates a piezoelectric transducer that is attached to an optically transparent material, such as glass. The vibrations of the glass create acoustic waves which cause the index of refraction of the glass to change. These changes in index of refraction scatter light. The frequency of the scattered light has been shifted by a frequency equal to the acoustic vibrations of the glass. A frequency shift on the order of 40 MHz is common in LDV.

The frequency shift is often needed to determine the direction of the flow. A particle passing through the probe volume normal to the fringes will produce a signal identical to that of a particle passing in the opposite direction. In oscillating or highly turbulent flows this can result in directional ambiguity. The Bragg-cell introduces a negative frequency offset so that the minimum detectable frequency will necessarily correspond with a negative velocity and the maximum detectable frequency will necessarily correspond with a positive velocity, see Figure 2-6.

Upon exiting the Bragg-cell, the two beams travel through a lens that focuses them at the designated point or volume—the probe volume. As the two beams of coherent light intersect their wave fronts constructively and destructively interact to form a series of equally spaced lines or fringes. Lines of constructive interference are lit while lines of destructive interference are dark, see Figure 2-7. As the particle crosses the fringes light is alternatively scattered and then not scattered. A photodetector will receive scattered light at a frequency proportional to the distance between the fringes. This distance is determined through the wavelength of light and optics used to cross the beams

$$\delta_f = \frac{\lambda}{2 \sin \theta} \quad (2-6)$$

where  $\lambda$  is the wavelength of the incident light, and  $\theta$  is half the angle of intersection of the two laser beams. Finally, the velocity of the particle is calculated as the product of the distance (fringe spacing) and frequency.

The geometry of the probe volume can be calculated geometrically, assuming the laser beam has a Gaussian intensity ( $1/e^2$  of the maximum). This results in an ellipsoid with the following dimensions:

$$\delta_z = \frac{4F\lambda}{\pi D_L \sin \theta} \quad (2-7)$$

$$\delta_x = \frac{4F\lambda}{\pi D_L \cos \theta} \quad (2-8)$$

$$\delta_y = \frac{4F\lambda}{\pi D_L} \quad (2-9)$$

F is the focal length of the transmitting optics and  $D_L$  the diameter of the laser beam, see Figure 2-8. Finally, the Doppler frequency can be calculated:

$$f_D = \frac{2u_x}{\lambda} \sin \theta \quad (2-12)$$

where  $u_x$  is the velocity normal to the fringes. Table 5-1 lists the probe volume characteristics. In determining the Doppler frequency, it is assumed that the particle velocity is constant as it travels through the volume and the fringes composing the sample volume are of uniform spacing. The magnitude and direction of scattered light depends on the relative refractive index of the dispersed and continuous phases and the wavelength of light and can be determined through Mie scattering theory. Figure 2-9 shows the relative intensity of light scattered from 1.0 mm glass spheres in water as a function of angle for 514 nm light.

The scattered light is collected through a combination of lenses and typically focused through a pinhole aperture onto either a photomultiplier tube or a photodiode. The pinhole is needed to eliminate extraneous light from other particles in the system from entering the photo detector (Goldstein [47]). Furthermore, the pinhole allows only light nearest the “core” of the probe volume to be detected. This central core of laser

light is the most planer. Finally, a photodetector transforms the laser light oscillations into an electrical signal.

As mentioned above, the Bragg-cell shifts the frequency of only one beam, so that the detected signal is that of the Doppler frequency plus the frequency shift. This signal is typically electronically downmixed to a lower frequency via a process known as heterodyning (Albrecht et al. [45]). Let  $\omega_1$  be the Doppler frequency and Bragg-cell induced frequency shift and  $\omega_2$  the designated downmixing frequency. Since the photo detector measures intensity, which is the square of the signal, the sum of the two frequencies is squared:

$$(\sin \omega_1 t + \sin \omega_2 t)^2 = (\sin \omega_1 t)^2 + 2(\sin \omega_1 t \times \sin \omega_2 t) + (\sin \omega_2 t)^2 \quad (2-13)$$

Only the middle term on the right side of the equation can be detected by the detector.

Utilizing the following trigonometric identity on the middle term

$$(\sin \omega_1 t \times \sin \omega_2 t) = \frac{1}{2}[\cos(\omega_1 + \omega_2)t + \cos(\omega_1 - \omega_2)t] \quad (2-14)$$

the difference frequency can be found. Again, the sum component is too high to be detected. Thus, the detected signal is equal to the Doppler frequency plus the difference in  $\omega_1$  and  $\omega_2$  (Goldstein [47]). The downmixing frequency can be adjustable and is dependent on the Bragg-cell frequency shift and the flow characteristics. See Figure 2-10.

### **Phase Doppler anemometry**

Phase Doppler anemometry was originally developed by Durst and Zare [48] and is now widely used and commercially available. Size measurements are determined from the difference in phase of a single Doppler signal detected at two positions separated by a known distance—assuming a spherical particle. A thorough background can be found in Albrecht et al. [46]. For two photo detectors that are symmetric about a

bisecting plane, and located at an off-axis angle of  $\varphi_r$ , and in the case of reflective particles, the difference in phase of the signal observed at the two detectors is

$$\Phi = \frac{2\pi d}{\lambda} \sqrt{2} * \left( \frac{\sqrt{1 - \cos \psi \cos \varphi \cos \theta + \sin \psi \sin \theta} - \sqrt{1 - \cos \psi \cos \varphi \cos \theta - \sin \psi \sin \theta}}{2} \right) \quad (2-15)$$

where  $\psi$  is the angle created by the plane that bisects the two photo detectors and  $\varphi_r$  is the angle of the receiver Albrecht et al. [46]. See Figure 2-11.

The PDPA uses the ratio of the time lag between the signals detected at the two locations,  $\Delta t$ , and the period of the signal,  $T$  (see Figure 2-12)

$$\Phi = 2\pi \frac{\Delta t}{T} \quad (2-16)$$

combining equations 2-15 and 2-16, the particle diameter is:

$$d = \frac{\lambda \Delta t}{\sqrt{2} T} \div \left( \frac{\sqrt{1 - \cos \psi \cos \varphi \cos \theta + \sin \psi \sin \theta} - \sqrt{1 - \cos \psi \cos \varphi \cos \theta - \sin \psi \sin \theta}}{2} \right) \quad (2-17)$$

When particles are not perfect spheres the calculated diameter will contain error. The amount of error depends on the non-sphericity of the particle and the random particle orientation while traversing the probe volume. Typically, multiple phase calculations are made from multiple photo detectors. A non-spherical particle will result in different phases and thus different diameters. Particles that exhibit phases greater than a set value can then be rejected. In the present case three photo detectors are used (A, B, and C) to calculate two phases for each particle—AB and AC. When the phase measurements between AB and AC differed by more than 8% the size measurement was rejected.

## **Solids concentration**

LDV/PDPA systems have been used to determine the solids concentration by relating the number and size of measured particles to the total volumetric flux through the probe volume over a period of time. The use of laser Doppler and phase Doppler techniques in the determination of solids concentration profiles and mass flux continues to be the subject of much research due to the many sources of error in such measurements, Dullenkopf et al. [49]. Reliable concentration measurements depend on several factors, including particle velocity, size, transit time, and trajectory (Aísa et al. [50], Roisman and Tropea [51]). Additionally, the effective size of the probe volume is dependent on laser beam intensity, particle size, collection angle, and width of the focusing slit.

The use of laser beams with Gaussian intensities has the effect of biasing PDPA measurements toward larger particles, Qiu and Sommerfeld [52]. The beam is less intense at the edge, potentially allowing smaller particles, which scatter less light, to pass through the edge of the beam undetected. A larger particle traveling through the same portion of the probe volume would scatter more light and consequently is more likely to be detected. This results in a probe volume or probe volume cross-section that is a function of particle size.

Qui and Sommerfeld [52] have identified errors stemming from signal-to-noise and trigger levels. Further errors have been identified from the simultaneous presence of multiple particles in the probe volume (Roisman and Tropea [51]) and from counting a single particle as multiple (Van den Moortel et al. [53]). In the latter, an overestimation known as burst-splitting, fluctuations in beam intensity at the level of individual bursts result in a single burst having multiple peaks and its subsequent interpretation as

multiple particles. The fluctuations can come from many sources, i.e. beam interruptions in dense flows. Recently, several post-processing algorithms have been developed with the aim of mitigating these errors (Van den Mortal et al. [53], Bergenblock et al. [54], and Sommerfeld and Qiu [55]). Unfortunately, these algorithms require signal processing not available with the PDPA presently used. Fortunately, the experimental conditions are fairly ideal (Saffman [56]) in that the flow is largely 1-dimensional (pipe flow in contrast to a jet) and relatively dilute.

Various methods exist for determining mass flux with phase Doppler techniques (Dullenkopf et al. [49] and Roisman and Tropea [51]). In all approaches the particle velocity and size are measured. The main differences lie in the determination of the experimental probe area or volume—the area or volume created by the crossing of the two laser beams. In the present case the probe volume area is automatically corrected for particle size. The experimental volume is defined as:

$$V = UtA \tag{2-18}$$

where A is the diameter dependent experimental cross section, t is time, and U the mean velocity. In determining the cross section, the laser beam is assumed to have a Gaussian power distribution and the intensity of light scattered by the particles is assumed to be proportional to the square of its diameter. Thus, the solids concentration is:

$$v = \frac{n\pi d_{30}^3}{6UtA} \tag{2-19}$$

where n is the total number of validated particles after all validation requirements are satisfied and  $d_{30}$  the volume-average diameter.

$$d_{30} = \sqrt[3]{\frac{\sum_{i=1}^n d_i^3}{n}} \quad (2-20)$$

The solids concentration measured with the PDPA was compared to that determined by sampling the flow and found to be unreliable, at time over predicting the solids concentration and at other times under predicting it. At the highest solids concentration the measured solids concentration near the wall was 2 orders of magnitude greater than that measured in the center of the pipe, indicating an almost total lack of particles in the center. However, it was clear from watching the slurry that particles were indeed traveling through the center of the pipe. The discrepancies most likely come from decreasing signal quality and data rate as the probe volume approaches the center of the pipe. Consequently, the radial solids concentration profiles as measured with the PDPA were not included in the results.

## **Experimental Procedures**

### **LDV/PDPA System**

A two-component Laser Doppler Velocimeter/Phase Doppler Particle Analyzer (LDV/PDPA) was used to measure the mean and fluctuating velocity components of the solid and liquid as well as the particle size. The system utilizes an Argon-Ion laser and a Bragg-cell to avoid directional uncertainty. The transmitting optics, receiving optics, and real-time signal analyzers were manufactured by TSI/Aerometrics. The optics are mounted on a traversing mechanism that can be positioned within 0.0001 inches. The relevant optical parameters of the LDV/PDPA system are summarized in Table 2-1.

A 500 mm focal length lens was used to measure the seed particles and 0.5 mm solids, allowing both phases to be measured simultaneously. For the 1.0 and 1.5 mm

particles two traverses across the pipe radius were made. The first measured the solid-phase and the second the fluid-phase. The 1.0 and 1.5 mm particles required a larger fringe spacing for accurate size measurements. This was accomplished through a beam contractor that reduced the initial beam separation from 40 mm to 20mm. The receiver utilized a 520 mm focal length lens and housed three photo detectors which give two phase determinations. If the two phase calculations differed by more than 8%, the particle was rejected.

The experiments with 1.0 mm and 1.5 mm particles were conducted with a Coherent 5W Argon laser. A new laser (Spectra-Physics Stabilite 2017 6W Argon) was purchased prior to the 0.5 mm experiments. The power of each laser beam at the probe was 10-20 mW with the Coherent laser and 60-90 mW with the new laser. The voltage of the photomultiplier tubes (PMTs) was adjusted as needed to compensate for signal attenuation as the probe volume penetrated the slurry. The PMTs were maintained between approximately 450 - 550 V and 375 – 450 V for the old and new lasers, respectively. The best voltage was determined by balancing maximum data rate with minimum noise, as judged by monitoring the Doppler bursts on an oscilloscope.

A 20 MHz high-pass filter was used to remove the pedestal from the raw signal. The burst threshold was maintained at 0.2 mV. The mixer frequency for the axial velocity and size measurements was 36 MHz, while the sampling rate and low-pass filter were 10 MHz and 5 MHz, respectively, for the runs at the two lower flow rates. For the highest flow rate the sampling rate and low-pass filters were doubled to 20 MHz and 10 MHz, respectively. This change was necessary because the highest velocity measurable at the combination of 10 MHz sampling and the optics employed was less

that needed to avoid aliasing. See Table 2-1. Data rates varied from over 100 Hz for the solid particles near the wall to less than 0.1 Hz for the liquid at the pipe center. The individual validation rates of the 1.0 and 0.5 mm particles ranged from 40% to 10%, depending on location in the pipe. Data was collected at 14 points across the pipe, with a greater density of points near the pipe wall. Due to refractive index changes, the closest measurements could be made to the wall was at  $r/R$  of approximately 0.95.

### **Phase Discrimination**

The discrimination of the solid and liquid was based on particle size. Established techniques based on signal amplitude differences between the two phases do not generally work in liquid-solid flow (Assar [57] and Chen and Kadambi [58]) because the slip velocity between the two phases is too small. Axial velocity and particle diameter data was collected. The data was collected under software coincidence—meaning each particle diameter measurement was associated with a specific particle velocity.

The seed particles were two orders of magnitude smaller than the particles composing the solid-phase. Thus, two distinct and easily distinguishable diameter peaks were observed by the PDPA. The 0.5 mm particles had an average particle diameter, according to the PDPA, of 0.48 mm and all coincident particles between 375 and 600  $\mu\text{m}$  were collected. The 1.0 mm particles had an average diameter of approximately 985  $\mu\text{m}$  and all coincident particles between 750 and 1200  $\mu\text{m}$  were included in the solid-phase data. In both cases, a minimum of 1000 size-velocity coincident measurements were collected at each point. However, in most cases several thousand points were obtained. In the case of the 1.5 mm particles, only the fluid was measured. For the liquid measurements, all particles from the optically limited

minimum of 2.48  $\mu\text{m}$  to 100  $\mu\text{m}$  were included in the liquid-phase statistics. Averages of 500 samples were collected for the liquid-phase.

## **Data Limitations**

### **Exclusion of 1.5 mm solid data**

The velocity measurements of the solids phase of the slurry composed of 1.5 mm particles were excluded from the results because they were determined to be inaccurate. The fluctuating velocity of the 1.5 mm particles was measured to be significantly greater (approximately double) than that of the 1.0 mm particles at each set of conditions. The 1.5 mm particles were measured with a 750 mm focal length lens (with the 0.5x beam contractor) not manufactured or specifically designed for LDV because an appropriate lens could not be purchased. A 1000 mm focal length lens with the 0.5x beam contractor was available and had the capability to size the particles, but the probe volume was too large. Additionally, lenses that precisely fit the current system could not be found and thus the 750 mm lens was had to be carefully fitted to the housing of the LDV probe.

The diameter of the 750 mm lens was slightly less than needed. Duct tape was carefully wrapped about the circumference of the lens until the lens fit securely. A razor blade was used to trim the tape and ensure the tape and lens thickness was uniform. The beams passing through the 750 mm lens passed all alignment and convergence checks, and the data rate and signal quality appeared equal to that of the lens used to measure the 1.0 mm particles. However, upon comparing the solids velocity fluctuations, the 750 mm lens with the 0.5x beam contractor was used to measure the 1.0 mm particles. The fluctuating velocity measurements were significantly inflated over those measurements obtained with the 500 mm lens with beam contractor. After

additional investigation it was decided that either the 750 mm lens or the method of securing it in the LDV probe housing was unreliable, and the data was discarded. However, the measurements of the fluid in the presence of the 1.5 mm particles are still reliable as they were made with the same lens as all fluid measurements.

### **Limited radial penetration in slurry of 0.5 mm particles**

At the highest solids concentration, 3% by volume, solid and liquid measurements of the 0.5 mm particles were limited to  $r/R \geq 0.5$ . This is due to increased signal attenuation by the increased number of particles in the slurry. For a given volumetric solids concentration, there are 8 times the number of 0.5 mm particles as 1.0 mm particles. Consequently, there is a significant increase in the number of particles the scattered light must pass through before reaching the receiver. This scatters and weakens the signal as light is reflected and refracted at each fluid-particle interface. Increasing the laser power and/or the PMT voltage did not increase the maximum penetration depth.

### **Procedural Obstacles**

The design of the slurry flow loop was begun in January 2005 and completed in March of 2006. The fabrication was completed by Met Pro Supply of Bartow, FL and delivered in May 2006. A number of modification/improvements have been made since the system was originally constructed.

### **Flow control and air bubbles**

Flow control was initially attempted via a bypass by connecting a pipe in a T-junction just after the pump, leading directly back to the water tank. This method did not provide adequate control or reproducibility of flow. Before the variable frequency drive was installed, the pump could only be operated at full power. Under full power air

bubbles were present in the test section—most likely from cavitation. However, in the process of troubleshooting the air bubbles it was hypothesized that air was being entrained through the water tank. The water discharge from the particle separator into the tank resulted in a large amount of splashing. To address this, a pipe extension was attached to the discharge. The extension submerged the discharge, split the single pipe into two, and routed the flow up through two U-bends. The objective was to route any entrained air up to the surface and decrease the flow rate to increase the residence time in the pipe, giving air more time to rise to the surface. This pipe was eventually found to be unnecessary.

In attempt to mitigate the cavitation in the venturi eductor, two additional orifices were constructed from Delrin (a hard and smooth plastic) on a lathe. The orifices had larger openings than the orifice that came with the venturi eductor. The larger diameter would increase the pressure and hopefully eliminate the cavitation. The two in-house orifices were successful in increasing the pressure in the venturi, but the failure of the bypass to control the flow necessitated the VFD, and the two in-house orifices were not needed once the VFD was installed. Delivery and installation of the VFD required a couple months.

### **Excessive turbulence**

Once the flow was under the control of the VFD the first attempted measurements were of single-phase water. Initial fluctuating velocity measurements were noticeably larger than literature values. An initial hypothesis was that the velocity fluctuations were influenced by the pipe vibrations. When running, the entire loop vibrated, with the vibrations increasing with increasing flow rate/pump speed. To mitigate this, vibration damping clamps were placed in several locations upstream and downstream of the test

section and anchored to the building by a network of steel struts. This was effective in reducing the pipe vibration but its effect on the velocity fluctuations was uncertain.

To better understand the vibrations accelerometer measurements of the test section, pump, and scaffolding were taken. These measurements showed a primary vibration frequency equal to the pump driving frequency supplied by the VFD, and then a series of harmonics that corresponded to the six veins of the pump impeller. In all cases the frequencies of vibrations were less than 1 kHz. This frequency of vibration was deemed insignificant in comparison with the Doppler frequency measurements because the scattered light signal is several orders of magnitude larger than the vibrations. Furthermore, the high pass filter used to remove the signal pedestal would also remove any contribution from the vibrations.

However, the excessive fluid turbulence remained. The turbulence intensity differed depending on the radius measured—for example, north, south, or east radius of pipe. In the original design the test section consisted of two glass windows each 6 inches in length. The two windows were separated by 8 pipe diameters of stainless steel pipe. Nominal 3 inch stainless steel pipe has an internal diameter of 3.068 inches. The glass windows were 3.0 inches. It was hypothesized that this step was increasing the level of turbulence at the wall. Further measurements confirmed this. The turbulence at the pipe center was consistent with literature values while there was an increase in wall turbulence at the bottom of the window vs. the top. The two 6 inch windows and pipe were replaced with a single window 12 pipe diameters (36 inches) in length. This new window allowed any increase in turbulence fostered by the pipe diameter difference to dissipate and fluid wall turbulence measurements confirmed this.

Between 3 and 5 pipe diameters, depending on  $Re$ , were needed for the increased wall turbulence to dissipate to that expected in fully developed pipe flow. Approximately six months elapsed from the first single-phase measurements to when those same measurements accurately matched literature values across all radii.

### **Phase discrimination and particle selection**

The two methods outlined above were based solely on laser Doppler measurements—velocity measurements only. Measuring the particle size via phase-Doppler measurements was not initially deemed feasible due to the large particle size. The refractive nature of the glass particles required a forward scattering angle. At the recommended angle of  $30^\circ$ , sizing 1.0 mm particles required a 1000 mm focal length lens and the 0.5x beam contractor. This resulted in a probe volume with length of 94 mm; more than double the pipe radius. This lack of resolution resulted in attempting measurements without the PDPA.

The method outlined by Alajbegović et al. [16] was the intended method of distinguishing the solid and liquid. Alajbegović et al. [16] utilized 2.3 mm glass particles and found their transit time was significantly larger than the seed particles, claiming two distinguishable peaks in a histogram of time spent in the probe volume. However, the probe volume is ellipsoidal and thus large particles passing through the edge will have short transit times. A series of ideal measurements conducted outside the pipe, consisting of dropping particles of various sizes from a set height through the center of the probe volume did not show any repeatable correlation between size and transit time. Several months were spent working with this method before it was rejected.

The next method of discrimination attempted was that typically used in gas-solid flows. The increased slip found in gas-solid flows results in two distinguishable velocity

peaks. Adjusting the laser power/PMT power appropriately—less power for large particles, more power for small seed particles—has been shown to give good phase discrimination (Jones [8]). The glass particles were replaced with 2 mm stainless steel shot. Two peaks were visible but largely overlapping. Larger stainless steel spheres, 3/16 inches in diameter (4.76 mm), were then attempted. These larger particles were tested, in part, to prove that the method would work. Clearly their size and density would result in a collision-dominated regime. Although two peaks were identifiable, the results were of low quality, most likely due to the large size of the particles.

While working with the stainless steel particles, whose scattering is entirely reflective, it was realized that at a reflective angle the largest diameter measurable by the PDPA increased. Consequently, stainless steel shot approximately 600  $\mu\text{m}$  in diameter was purchased. The smaller diameter and increased density, in comparison with glass, resulted in very similar Bagnold numbers (see equation 1-4). The smaller diameter allowed the PDPA to measure the size of the particles and distinguish the phases based on diameter. However, it was found that shot is not spherical enough to meet the requirements of the PDPA. The signal was very noisy and resulted in a very low quality diameter histogram. Both traditional and conditioned cut-wire shot were tried with low quality results.

Finally, glass beads, which have a much higher sphericity than steel shot, were tried with the receiver in a reflective position, at  $30^\circ$  from backscatter. This arrangement proved to be the best arrangement and was used for all experiments. Ultimately over a year was spent in determining a suitable particle and phase discrimination technique.

Several seed particles were also tried before the 10  $\mu\text{m}$  silver coated hollow glass spheres, mentioned above, were selected. Unfiltered tap water, with its inherent contaminants, was found to provide a good signal during single-phase experiments. The seed was added in hopes of improving the data rate of the fluid in the presence of the solid-phase. 10  $\mu\text{m}$  hollow glass spheres, 20  $\mu\text{m}$  polyamide particles, and  $\text{TiO}_2$  particles were also tried. Filtering the tap water and then adding seed was also tried—an in-line water filtering line was built. The filter removed material  $> 20 \mu\text{m}$ . However, it was found that filtering did not have an effect on the fluid data rate.

Laser Doppler measurements in round pipes of small diameter can often be biased by refraction effects from the curved surface. These effects are typically overcome by constructing a planar front to the pipe, such that the laser beams are normal to a flat surface that is matched in index of refraction to the pipe, and in some cases, the fluid. This error was deemed negligible under the present conditions due to the relatively large pipe diameter and the fact the measurements were limited to 1D axial profiles. The two laser beams were aligned with the axis of the pipe; the degree of curvature over the width of the laser beam at the point it entered the pipe was determined to be less than  $1^\circ$  for all radial locations across the pipe.

When a second signal processor was still working, making 2D measurements tenable, a planar front was constructed. The box had a glass front and silicone sealant was used to attach it to the glass pipe. The interstitial space was filled with a matched index of refraction liquid (a concentrated solution of NaI). The planar front was ultimately found to be disadvantageous because the data rate decreased due to the deep yellow color of the NaI solution.

## Other improvements

The paddle-wheel flowmeter was replaced with an electromagnetic flowmeter. The original location of the flowmeter was upstream of the venturi, thus making its measurement not representative of the flow through the test section. It was then moved immediately upstream of the test section. This location was eventually deemed problematic due to an increase in wall turbulence fostered by the slight differences in pipe diameter between the stainless steel pipe, flow meter, and glass test section. Ultimately the flow meter was moved to its final location approximately 5 pipe diameters downstream of the first long-radius bend.

Additional pressure taps were added to the original design, which had only 3 taps around the test section—see Chapter 4. Initially the holes into the pipe were made without regard to their diameter. However, after surveying the literature regarding pressure loss measurements, the effect of diameter was discovered. This required drilling of precise 1.0 mm holes through the pipe wall and repeating the measurements.

The original design provided for concentration sampling via the 3-way valve located immediately after the first long-radius bend. However, it was realized that due to the openness of the system, routing the flow out the 3-way valve rather up the vertical pipe into the test section necessarily changed the pressure drop and thus the flow rate. After much thought it was recognized that any change in the flow during sampling over the flow conditions during data acquisition would necessarily change the flow. This awareness led to the final “flow through” design, where the flow discharged through the sampling tank and the 3-way valve was used to route the flow around the tank after sampling. A 100 gallon tank was modified to attach a 4 inch bulkhead. A 3 inch bulkhead was initially tried and found to be too small to accommodate higher flow

rates. A 4 inch ball valve was attached to the bulkhead and was closed to fill the tank during sampling.

Changing flow meters, moving the flow meter, and moving the 3-way valve resulted in pipe length mismatches. These mismatches were remedied by constructing spacers from 0.75 inch thick sheets of acrylic. A 3 inch flow hole and corresponding holes for flange bolts were cut into squares of acrylic. The squares were then inserted between flange connections. Additionally, chlorine was added to the water each time it was replaced after mold began growing in the loop, requiring a thorough cleaning of the loop. The chlorine was designed for swimming pools and came in a granular form.

### **Equipment/instrumentation issues**

The final velocity measurements included only the axial direction. Originally both axial and radial mean and fluctuating velocity profiles were desired. The LDV/PDPA is a 3-D system. However during the course of troubleshooting both LDV signal processors ultimately failed. Both processors' power supplies failed at some point, with one requiring replacement. Ultimately, the LDV signal processors were shown to be unreliable, though their failure was not catastrophic. All told, several months were spent attempting to understand and diagnosis the erratic behavior of the processors before they were finally deemed unusable. Unfortunately, due to their age they could not be fixed and 1-D measurements were completed. Finally, prior to being found unreliable and being replaced, the paddlewheel flow meter also abruptly stopped working and was serviced.

## Error Analysis

### Velocity and size measurements

Laser Doppler velocimetry makes a direct measurement and requires no calibration. Statistical errors arise based on the number of samples used to determine the mean and fluctuating velocities of the two phases. Following the work of Yanta and Smith [59], the error in the ensemble mean is

$$\frac{\eta - \eta_e}{\eta} = \pm \frac{z_c}{\sqrt{N}} \left( \frac{\sqrt{u'^2}}{U} \right) \quad (2-21)$$

where  $\eta$  is the error in the population mean,  $\eta_s$  the ensemble mean,  $N$  the ensemble size, and  $z_c$  the confidence coefficient. The ratio of the standard deviation to the mean is the turbulence intensity. However, the error in the fluctuating velocity is independent of flow conditions

$$\frac{\sigma - \sigma_e}{\sigma} = \pm \frac{z_c}{\sqrt{2N}} \quad (2-22)$$

where  $\sigma$  is the population standard deviation and  $\sigma_s$  the ensemble standard deviation. For example, an ensemble of 1000 points at 95% confidence and a turbulence intensity of 0.05 will have 4.4% random error in the fluctuating velocity measurements.

The velocity histogram at each point was analyzed and outlying points were removed using a method analogous to the Thompson-Tau technique. A point was determined to be an outlier if it was not connected to either tail of the distribution and was more than three standard deviations from the mean. In the case of long tails, points had to be at least four standard deviations away from the mean and appear to be extraneous. After each point was removed, the mean and standard deviation was re-calculated prior to removing any additional points. Additionally, a scatter of velocity vs.

diameter was consulted to give additional information regarding the potential validity of the velocity measurement before it was discarded. The range of particle diameters used in the statistics did not have a significant impact on the velocity statistics. For example, changing the upper or lower limit by 10% would typically change the mean velocity by  $< 0.1\%$  and the fluctuating velocity by  $< 1\%$ .

When the probe volume was close to the wall a secondary peak at zero m/s would often appear. These points were removed in all cases. This was easily accomplished for the higher speed flows, while for the lowest velocity much care was taken to ensure that all relevant measurements were included. Additionally, the lowest possible sampling rate and low pass filter (LPF) combination was used in each case. It was found that using a higher sampling rate inflated the turbulence statistics. A higher sampling rate will obtain all its velocity data in a fewer number of cycles, increasing the uncertainty of the measurement, see Figure 2-13.

### **Radial location**

Measurements were always begun at the pipe wall and finished at the pipe center. The optics were positioned under single-phase flow to make alignment easier. To ensure that the laser was normal to the pipe, the beams entering the pipe were aligned vertically with their reflection off the back wall. The receiving probe has a magnifying lens that allows the user to see the crossing beams and focus the spatial filter in the center of the probe volume. The location where the beams cross from the glass pipe to the water is also visible. In each case the spatial filter was placed as close to the wall as possible while retaining a high-quality signal.

There is a small degree of uncertainty in this starting location. The distance from the first measurement to the second was 500 steps on the traverse (1.7 mm in water).

Based on the appearance of this distance in the receiving probe's magnifying glass, it can be assumed that the uncertainty in the initial starting location is  $\pm 100$  steps (0.34 mm in water). This uncertainty can be applied to all radial locations across the pipe. Near the pipe wall where the velocity gradients are the largest the radial uncertainty can contribute to the uncertainty in the fluctuating velocity measurements. Near the pipe center the gradients are much less steep and any contribution to the error in the turbulence measurements based the radial uncertainty is negligible.

It is also important to focus the receiving optics on the center of the probe volume. The center can be determined by sliding the receiving probe slightly forward and backward and ensuring the beams cross at their individual waists (narrowest point). This produces a "bow-tie" where the beams converge and diverge evenly. With a small probe volume, the center is easy to determine. When measuring the 1.0 mm particles great care was taken to ensure that the spatial filter was centered in the probe volume. As the pipe radius was traversed the receiving optics were adjusted to maintain alignment on the probe center. Near the pipe center under higher solids concentrations the crossing of the laser beams was more difficult to see. In such cases, the venturi was temporarily closed, removing the particles from the loop, making the beams visible and alignment easier before re-introducing the particles into the loop.

### **Solids concentration**

The error in the determination of the solids concentration was found to be less than 5%. The determination of the total slurry sampled was calculated from the height of slurry in the sampling tank. The height was measured from the top of the bulkhead fitting at the bottom of the tank to the water line. A wooden broom handle was slowly inserted into the tank and then removed. The waterline was then easily measured. The

error in this height measurement was estimated to be 3 mm, which translated into a total volume error of about 1%. The volume of the tank below the bulkhead was estimated mathematically based on its dimensions.

The second source of error was in the determination of the volume of the particles. The sampling tank was drained over a sieve which collected particles in the bottom of the valve. The bulkhead was not flush with the bottom of the tank, keeping settled particles from simply washing out upon draining. These particles were carefully collected by tilting the sampling tank onto its side, collecting the majority of them by hand, and then washing out the tank while passing the washout through a sieve. Some loss of particles was inevitable in this process, and thus any error resulted in an underestimation of the total solids. The amount of loss is difficult to estimate, though it can be safely assumed to be less than 5%. Based on repeatability, the sampling procedure was found to be accurate within 5%.

### **Pressure measurements**

The single greatest manifestation of error was the in the determination of the two-phase friction velocity from the hydraulic gradient. Turbulent flow is inherently random and this randomness will result in some degree of pressure fluctuations. Furthermore, the magnitude of the fluctuations will increase with increasing  $Re$ . This was found to be true for both single-phase and two-phase flow. However, the addition of the solid particles increased the variability of the pressure measurements, with the magnitude increasing with increasing solids concentration. The particle diameter did not appear to influence the pressure fluctuations significantly. The following analysis is in regard to the 1.0 mm particles.

Accordingly, the least amount of error was in the run at  $Re = 2.0 \times 10^5$  at a solids concentration of 0.7% by volume. The overall pressure change was from 5.25 to 2.20 PSI. Based on observation the pressure fluctuated from 5.1 to 5.4 PSI and 2.05 to 2.35 PSI, for the lowest and highest taps, respectively. Most of the fluctuations were about a smaller interval, and consequently the mean values could be fairly well established. The error could be safely assumed to be less than  $\pm 0.05$  PSI, or  $\pm 1.0\%$  and  $\pm 2.3\%$ , respectively.

The largest pressure fluctuations were found in the run at  $Re = 5.0 \times 10^5$  at a solids concentration of 3% by volume. In this case the pressure ranged from 7.8 to 4.3 PSI. However, the fluctuations ranged from 3.8 to 4.8 PSI and 7.3 to 8.3. These were extremes with the majority of the fluctuations on the order of  $\pm 0.25$  PSI with an uncertainty interval of  $\pm 0.15$  PSI, or 1.9% and  $\pm 3.5\%$ , respectively. This error does not appear significant, and the  $R^2$  values in the linear regression of all six pressure readings reflected this. The lowest value of the 1.0 mm particles was 0.9958, for  $Re = 3.35 \times 10^5$  at 1.7% solids. This relatively small amount of uncertainty, however, can have a significant impact on the friction velocity, and consequently the two-phase fluctuating velocity measurements were scaled by the centerline fluid velocity.

For each set of conditions the uncertainty of  $dP/dz$  at 95% confidence was determined:

$$W = t_{n-2} S_{zP} \sqrt{\frac{1}{\sum_{i=1}^n (z_i - \bar{z})^2}} \quad (2-23)$$

where  $t_{n-2}$  is the 95% confidence correlation parameter,  $z$  the height of pressure tap,  $\bar{z}$  (bar) is the average height, and  $S_{zP}$  is the standard error:

$$S_{zP} = \sqrt{\frac{\sum_{i=1}^n (P_i - P')^2}{n - 2}} \quad (2-24)$$

where  $P$  is the measured pressure and  $P'$  is the estimated value according to the best-fit linear regression. The standard error is a measure of the scatter about the best-fit line. The standard error assumes there is no error in the independent variable, in this case the height of the tap,  $z$ . Although the statistics show a significant uncertainty, the dilute nature of the slurry suggests it should not show a dramatic change in  $dP/dz$  over the single-phase. The two-phase frictional velocity was also calculated to give an additional comparison with the single-phase flow. The similarity in the two-phase friction velocity to that of the single-phase via both pressure drop and a measurement of the near-wall velocity gradient bolsters confidence in the two-phase pressure drop.

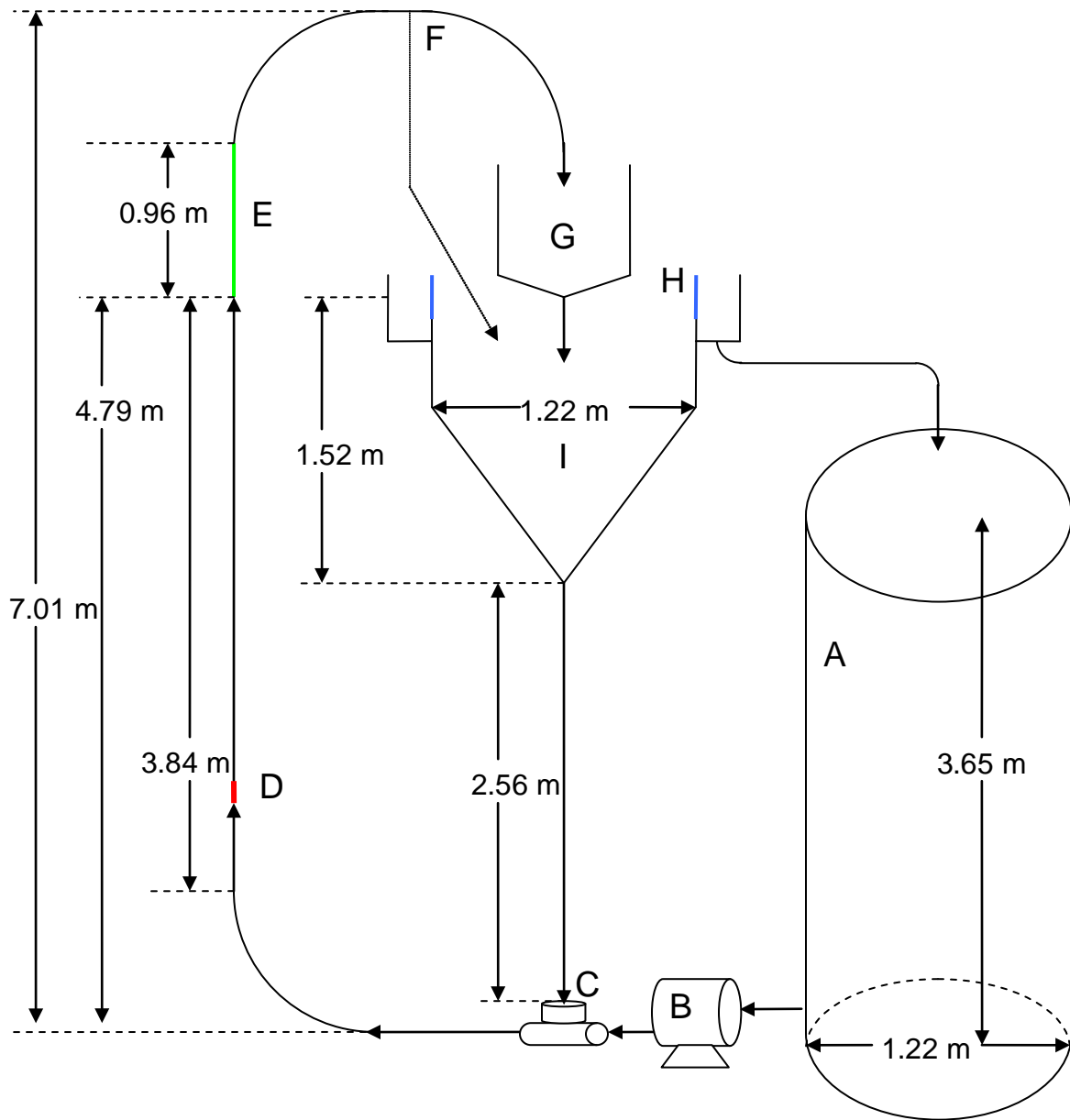


Figure 2-1. Flow loop. A) water tank, B) pump, C) venturi eductor, D) electromagnetic flow meter, E) test section, F) by-pass, G) sampling tank, H) particle screen and I) particle separator

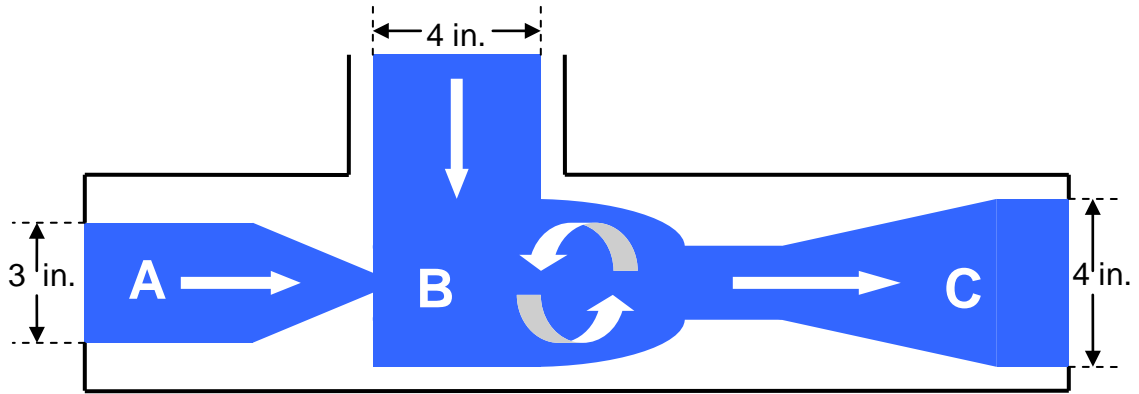


Figure 2-2. Venturi eductor. A) single-phase inlet, B) solids entrainment and mixing and C) slurry exit

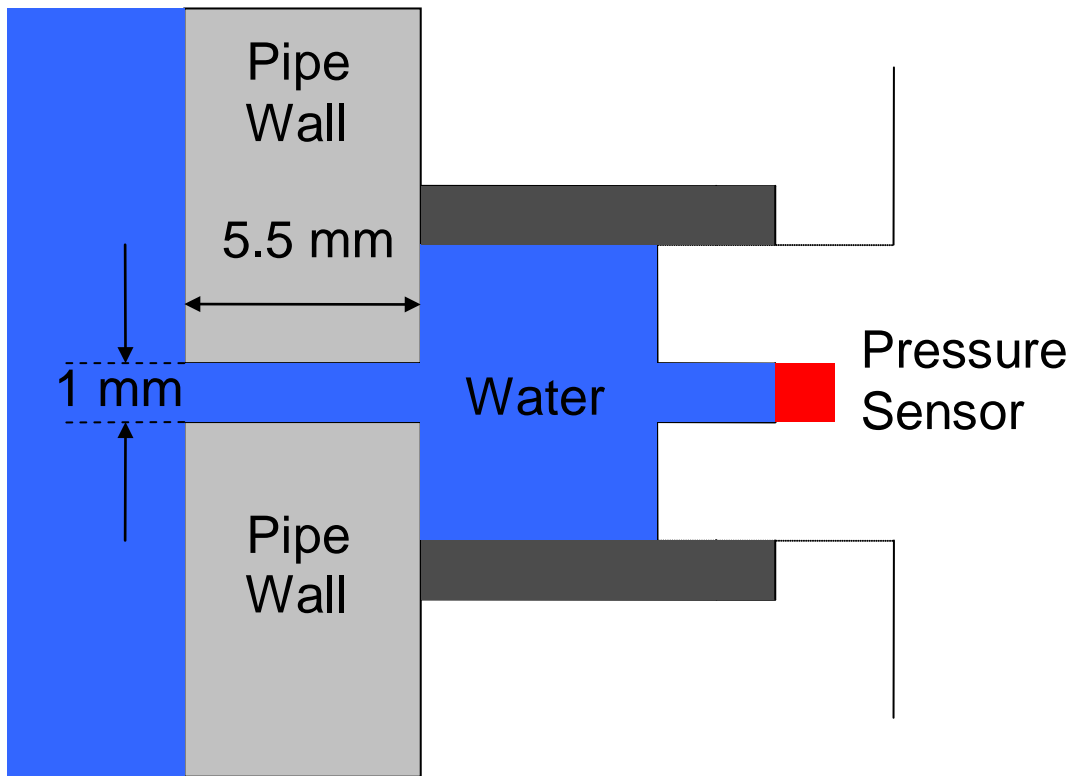


Figure 2-3. Configuration of pressure tap

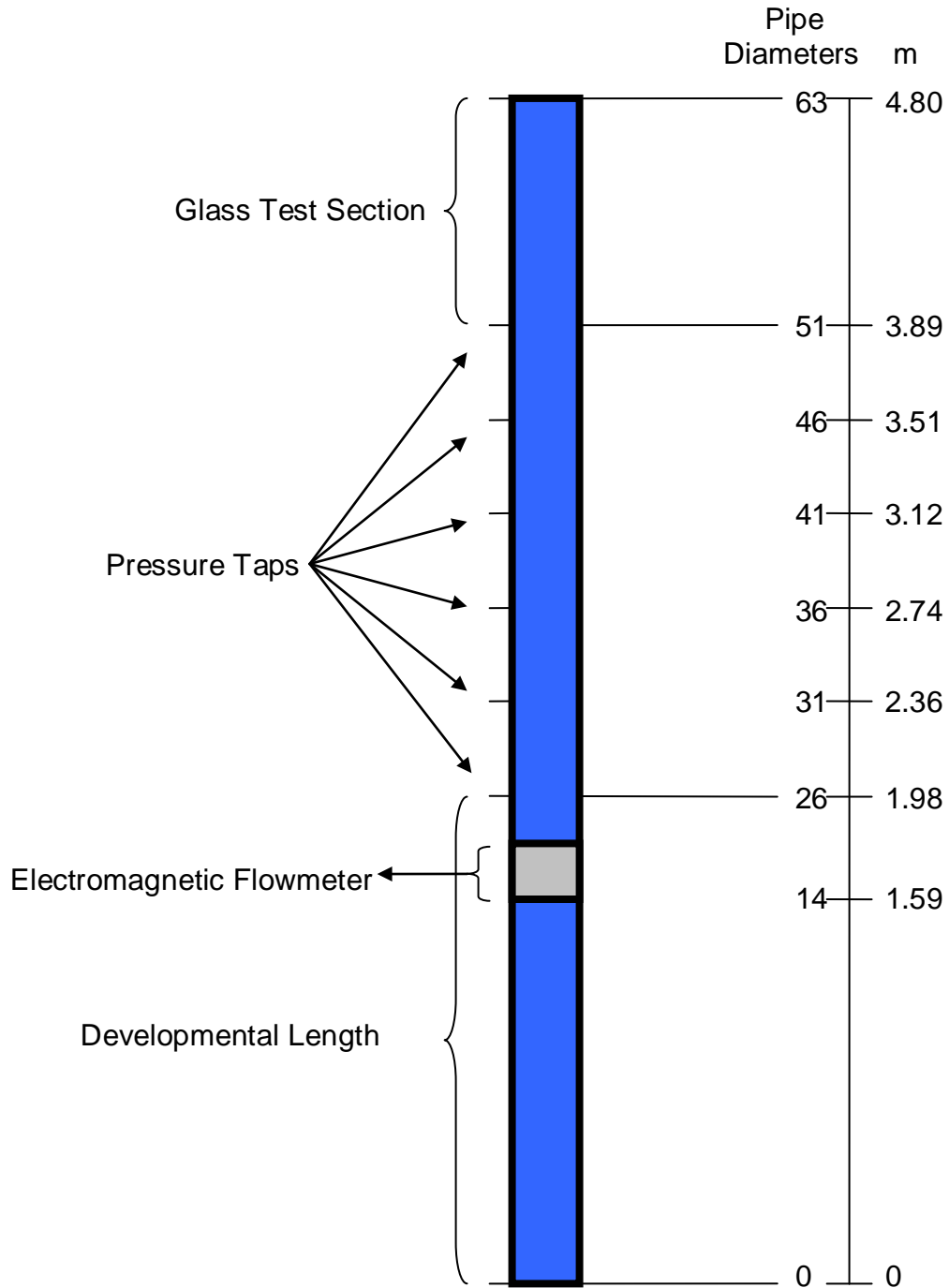
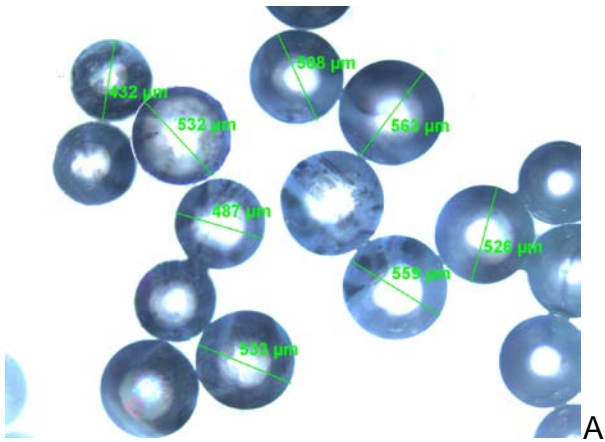
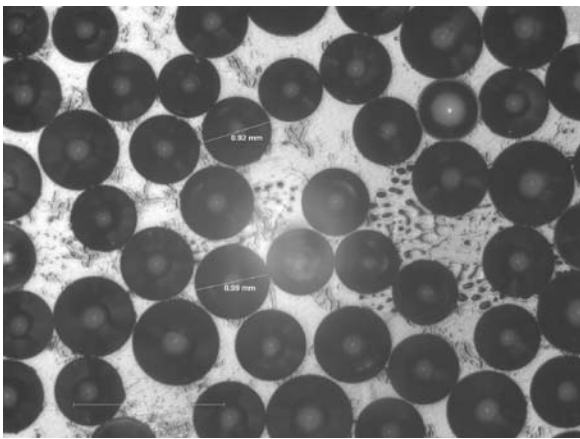


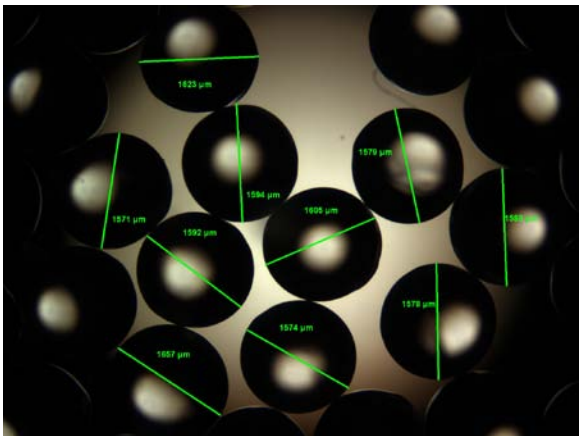
Figure 2-4. Vertical pipe dimensions



A



B



C

Figure 2-5. Experimental particles. A) 0.5 mm, B) 1.0 mm and C) 1.5 mm

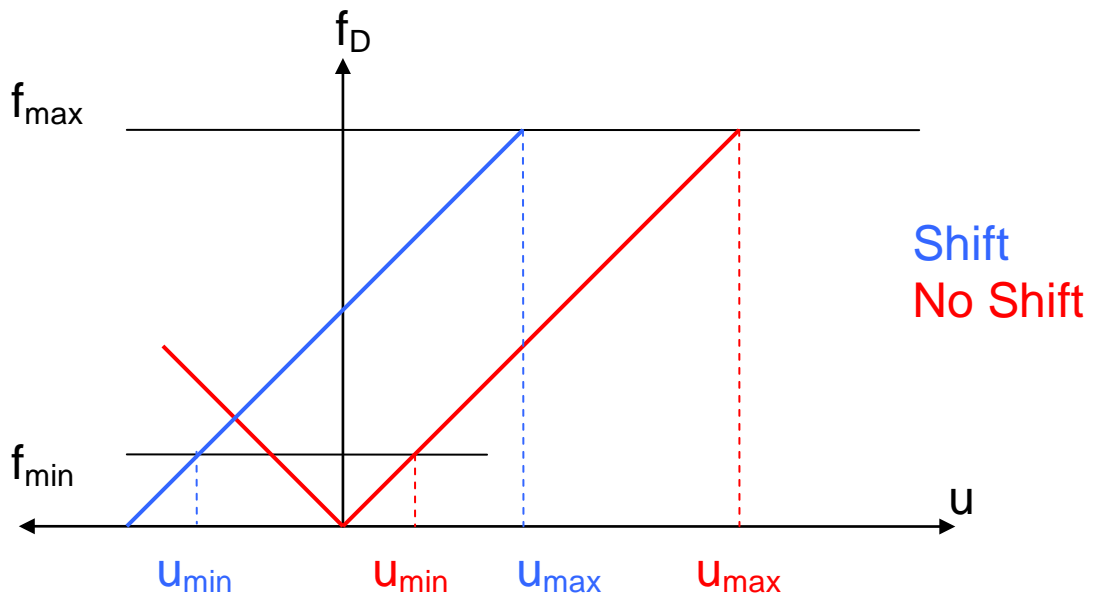


Figure 2-6. Resolving directional ambiguity with frequency shift

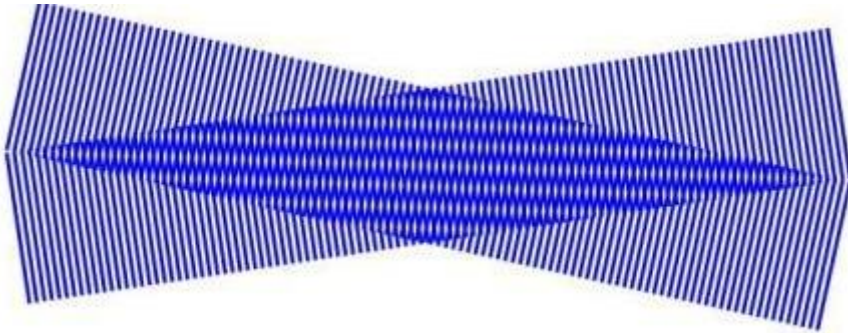


Figure 2-7. LDV probe volume fringes

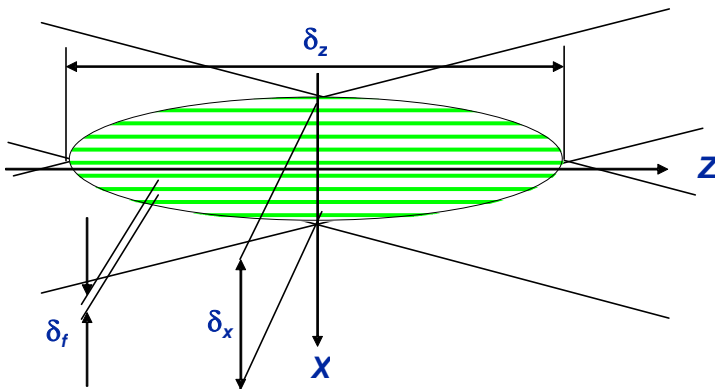


Figure 2-8. Experimental probe volume dimensions

Table 2-1. LDV/PDPA settings

	Liquid	1.0 mm Particles	0.5 mm Particles
Transmitting Optics			
Wavelength $\lambda$ (nm)	514.5	514.5	514.5
Focal Length (mm)	500	500	500
Fringe Spacing $\delta_f$ ( $\mu\text{m}$ )	6.4	12.9	6.4
Laser Beam Diameter (mm)	1.4	1.4	1.4
Laser Beam Intersection Angle	4.59°	2.29°	4.59°
Laser Beam Separation (mm)	40	20	40
Laser Beam Waist ( $\mu\text{m}$ )	234	468	234
Probe Volume Length $\delta_z$ (mm)	5.85	23.4	5.85
Probe Volume Height $\delta_x$ (mm)	0.234	0.468	0.234
Probe Volume Width $\delta_y$ (mm)	0.234	0.468	0.234
Receiving Optics			
Focal Length in air ( $\mu\text{m}$ )	521	521	521
Slit Aperture ( $\mu\text{m}$ )	400	400	400
Collection Angle	150°	150°	150°
Software Settings			
High Pass Filter (MHz)	20	20	20
Frequency Shift (MHz)	36	36	36
Sampling Rate (MHz)	10, 20	10, 20	10, 20
Low Pass Filter (MHz)	5, 10	5, 10	5, 10
Burst Threshold (mV)	0.2	0.2	0.2

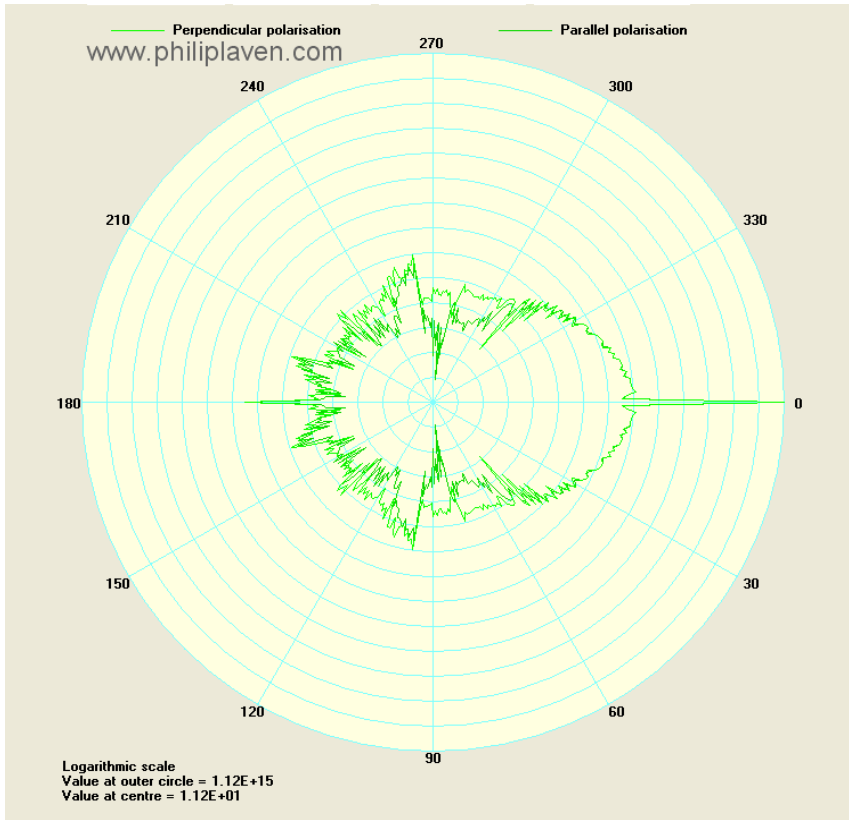


Figure 2-9. Light scattering intensity for 1 mm sphere for 514 nm light

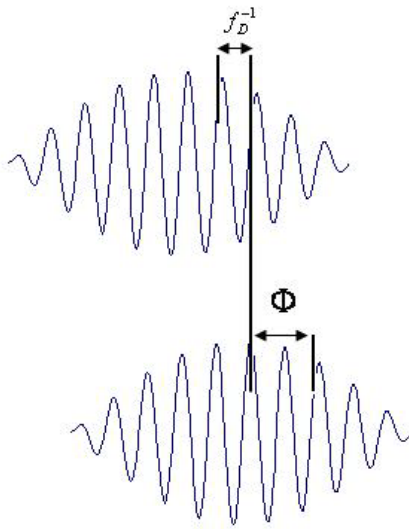


Figure 2-10. Frequency and phase measurements of a Doppler burst

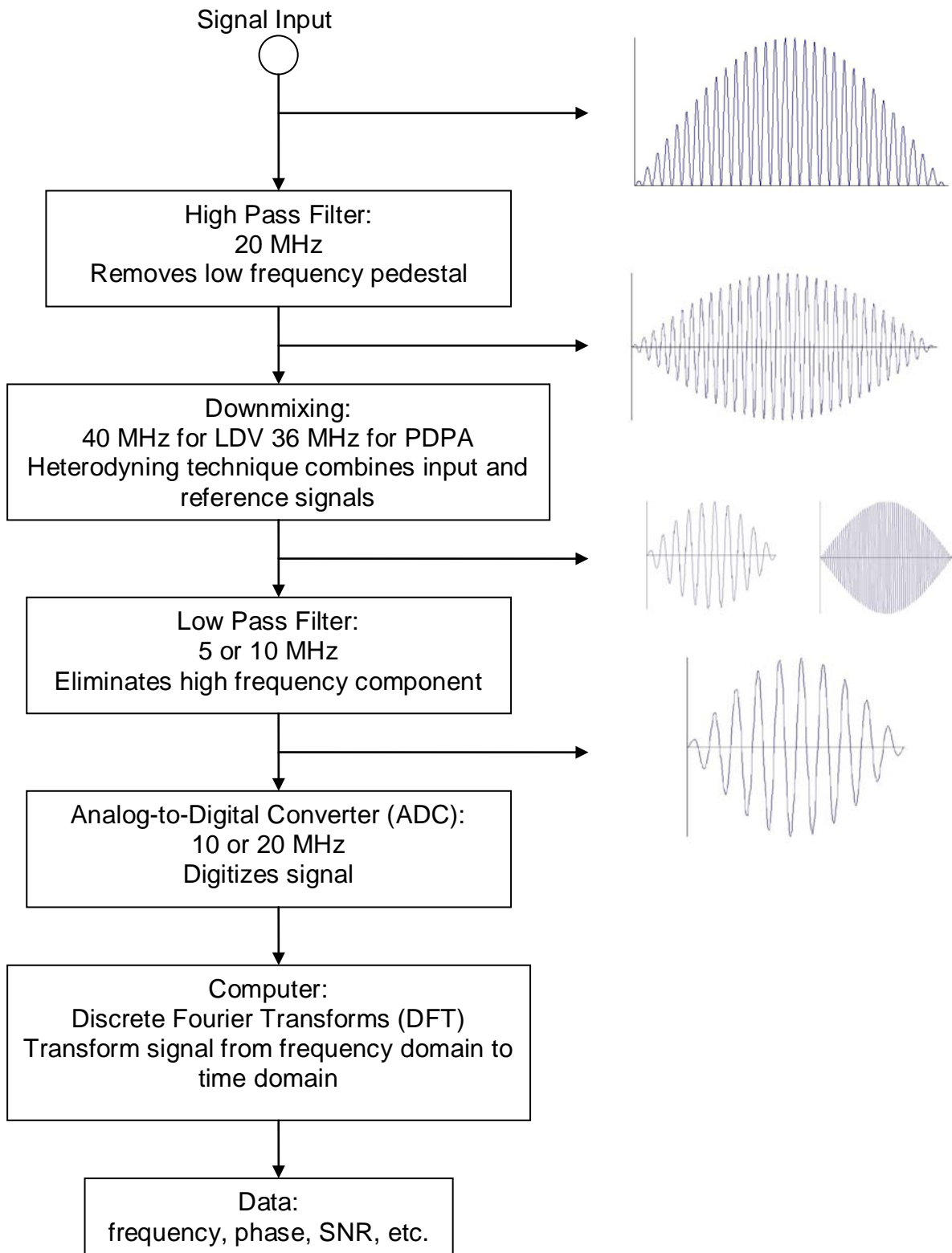


Figure 2-11. Signal processing flowchart

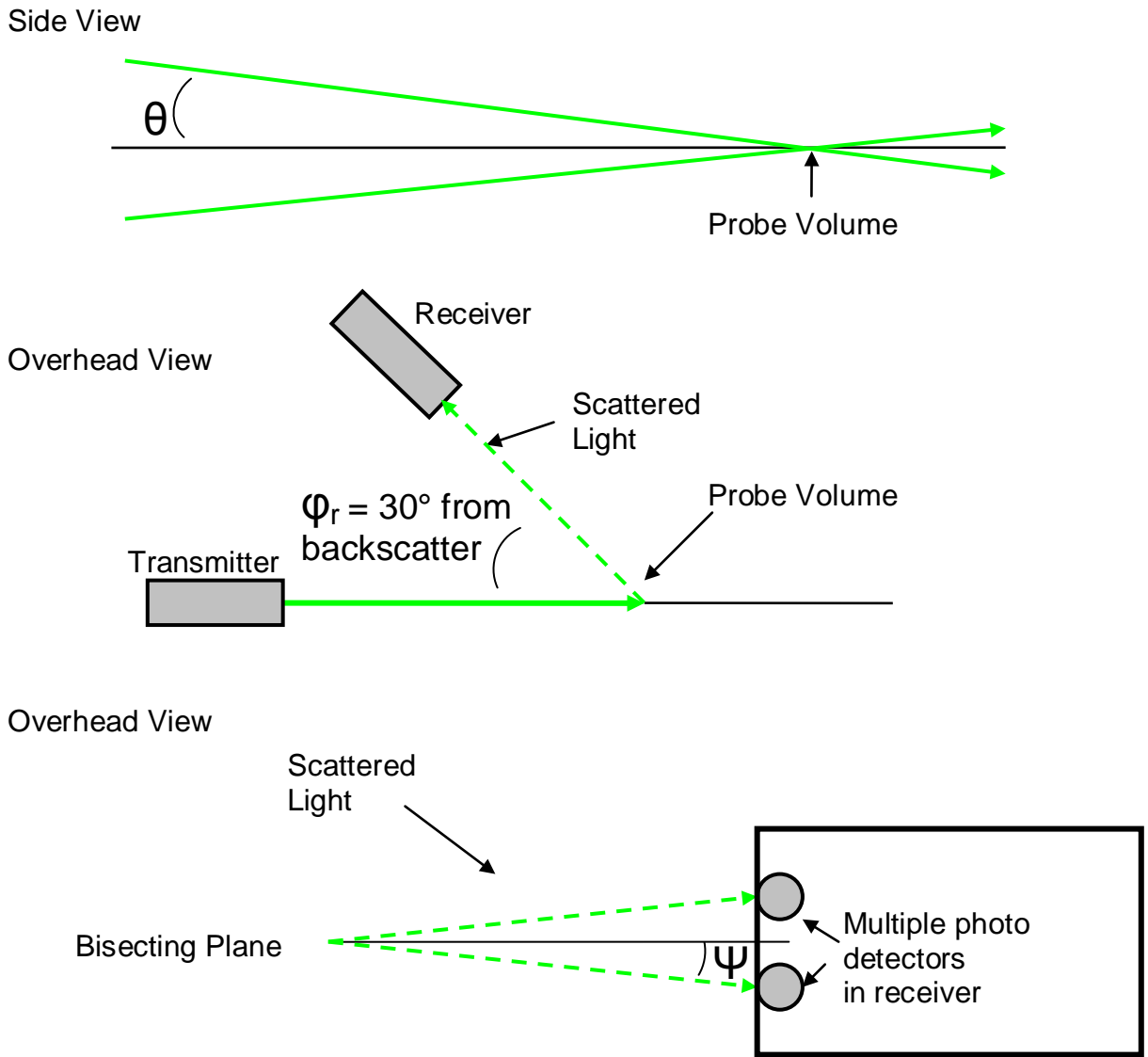


Figure 2-12. Phase Doppler setup. A) laser beams converging to probe volume, B) receiving probe and C) multiple photo detectors required to determine phase shift

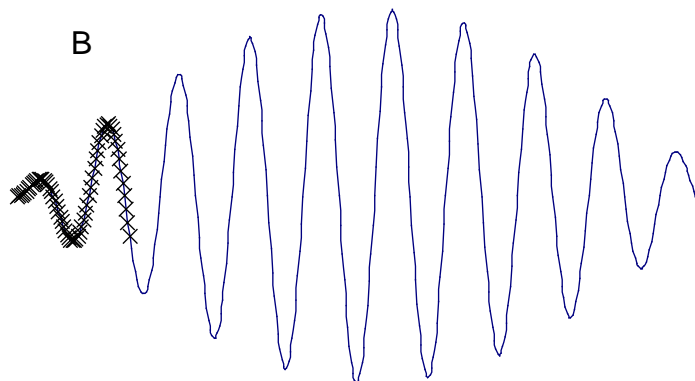
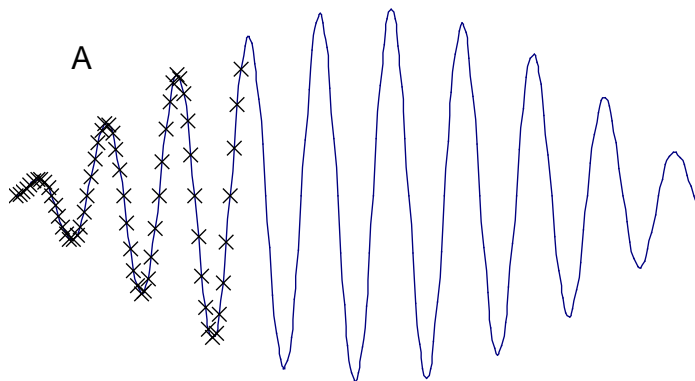


Figure 2-13. Sampling rate of Doppler burst. A) 64 points at rate X and B) 64 points at rate 2X.

## CHAPTER 3 TWO-PHASE MODEL

### **Kinetic Theory of Granular Flow**

State-of-the-art turbulent two-phase models involve mass and momentum balances for each phase and a fluctuating energy balance for the particle assembly. The mass and momentum balances originate from the work of Anderson and Jackson [42] and Lun and Savage's [60, 61] kinetic theory of granular flow is used for the particle stress and viscosity. The most rigorous treatment in two-fluid models employ Myong and Kasagi's [62] two equation  $k$ - $\epsilon$  model modified for the presence of a dilute particle phase.

The original kinetic theory of granular flow of Lun et al. [63] describes the transfer of momentum and kinetic energy between particles while neglecting the effects of the interstitial fluid. Lun and Savage [60, 61] later includes these effects by incorporating an additional stress exerted by the fluid on the particle through long-range interactions by means of fluid fluctuations. The theory of Lun et al. [63] was incorporated into a two-fluid model of a laminar gas-particle flow by Sinclair and Jackson [64]. Later, the kinetic theory of granular flow and gas turbulence were incorporated into a two-fluid model by Louge et al. [65], who used a one-equation turbulence model. This work was extended to a two-equation  $k$ - $\epsilon$  turbulence model by Bolio et al. [66]. The Bolio et al. [66] model was validated for various kinds of particles and particle sizes by the data of Tsuji et al. [5], Tsuji [67], and Jones [8]. However, the model has not been validated for liquid-solid flows in an inertia dominated regime.

When two particles in a fluid collide, two particle-particle interactions occur—direct collisions and interactions through the fluid. The direct collisions transfer momentum

and energy by elastic-plastic deformations while the fluid interactions occur via the fluid velocity gradient and pressure disturbances generated by the random motions of the particles. These random motions transfer momentum and energy through the fluid to neighboring particles. In Lun and Savage [60], particle-particle interactions occur through direct collisions only. Additionally, a particle undergoing an inelastic collision loses some of its fluctuating kinetic energy to heat. Further energy is dissipated into the fluid as the particle must expend energy to displace the fluid between the two particles.

The coefficient of restitution in a vacuum,  $e_s$ , can be measured experimentally with particle image tracking velocimetry, LDV, and other non-intrusive techniques. The velocities and trajectories of individual particles are tracked before and after collision. Values of  $e_s$  depend on the material properties of the colliding objects and are available for common materials.

### Governing Equations

Detailed explanation of two-fluid models that incorporate particle-particle interactions can be found in Bolio et al. [66]. Brief descriptions of the governing equations are outlined below. The fluid and solid continuity are given as

$$\frac{\partial[\rho_f(1-v)]}{\partial t} + \nabla \cdot [\rho_f(1-v)\mathbf{U}_f] = 0 \quad (3-1)$$

$$\frac{\partial[\rho_s v]}{\partial t} + \nabla \cdot [\rho_s v \mathbf{U}_s] = 0 \quad (3-2)$$

where  $v$  is the particle volume fraction,  $\rho_f$  and  $\rho_s$  are the fluid and solid density, and  $\mathbf{U}_f$  and  $\mathbf{U}_s$  are the fluid and solid velocity, respectively. Momentum balances are given as

$$\rho_f \left[ \frac{\partial \mathbf{U}_f}{\partial t} + \mathbf{U}_f \cdot \nabla \mathbf{U}_f \right] = -\nabla P - \nabla \cdot \boldsymbol{\tau}_f - \mathbf{F}_D + \rho_f \mathbf{g} \quad (3-3)$$

$$\rho_s v \left[ \frac{\partial \mathbf{U}_s}{\partial t} + \mathbf{U}_s \cdot \nabla \mathbf{U}_s \right] = -\nabla \cdot \boldsymbol{\sigma}_s + \mathbf{F}_D + \rho_f v \mathbf{g} - \rho_s v \mathbf{g} \quad (3-4)$$

The terms on the right side of the equation 3-3 are the pressure gradient, the fluid shear stress containing both viscous and Reynolds stress, the drag force of the fluid on the solids, and the gravitational force on the fluid, respectively. The terms on the right side of equation 3-4 are the particle stress, drag, buoyancy force, and gravitational force.

Equation 3-5 is the fluid turbulent kinetic energy  $k$  balance. Diffusion, generation by mean shear flow, and viscous-dissipation are the first three terms on the right side. The last term is the turbulence modulation that includes both collisional (Lun and Savage [60]) and fluctuating drag forces (Bolio et al. [66]).

$$\begin{aligned} \rho_f (1-v) \left[ \frac{\partial k}{\partial t} + \mathbf{U}_f \cdot \nabla k \right] &= \nabla \cdot \left[ (1-v) \left( \mu_{ef} + \frac{\mu_T}{\sigma_k} \right) \nabla k \right] + \\ (1-v) \tau_f^{REY} : \nabla \mathbf{U}_f^T - \rho_f (1-v) \epsilon - \mathbf{F}_{MOD} \end{aligned} \quad (3-5)$$

The rate of dissipation of the fluid turbulent kinetic energy  $\epsilon$  is:

$$\begin{aligned} \rho_f (1-v) \left[ \frac{\partial \epsilon}{\partial t} + \mathbf{U}_f \cdot \nabla \epsilon \right] &= \nabla \cdot \left[ (1-v) \left( \mu_{ef} + \frac{\mu_T}{\sigma_\epsilon} \right) \nabla \epsilon \right] + \\ c_1 f_1 \frac{\epsilon}{k} (1-v) \tau_f^{REY} : \nabla \mathbf{U}_f^T - c_2 f_2 \rho_f (1-v) \frac{\epsilon^2}{k} - c_3 f_2 \frac{\epsilon}{k} \mathbf{F}_{MOD} \end{aligned} \quad (3-6)$$

The terms on the right side of equation 3-6 represent the same contributions as in the  $k$ -equation. The  $c_i$ 's and  $f_i$ 's represent constants and functions, respectively, and are given in Myong and Kasagi [62].

The particle phase stress,  $\boldsymbol{\sigma}_s$ , depends on the granular temperature,  $T$ , and this can be found from a kinetic energy balance associated with the particle velocity fluctuations. This kinetic energy balance (or granular temperature balance or pseudo-thermal energy balance) can be found in Sinclair and Jackson [64]:

$$\rho_s v \left[ \frac{\partial E_{pt}}{\partial t} + \mathbf{U}_s \cdot \nabla E_{pt} \right] = -\nabla \cdot \mathbf{q}_{pt} - \sigma_s : \mathbf{U}_s - \gamma_{pt} + F_{KS} \quad (3-7)$$

where  $q_{pt}$  is the pseudo-thermal energy conductive flux,  $\sigma_s$  is the particle stress tensor,  $\gamma_{pt}$  the pseudo-thermal energy dissipation rate, and  $F_{KS}$  the interfacial energy flux by fluid-solid interactions. The detailed expression for these terms can be found in Lun et al. [63] and Lun and Savage [60,61].

### **Boundary Conditions and Model Solution**

No-slip boundary conditions are used at confining wall for the mean fluid velocity and the fluid turbulent kinetic energy  $k$ . The wall boundary condition for the turbulent kinetic energy dissipation rate,  $\varepsilon$  is determined from the  $k$  equation evaluated at the wall. For a full description of the  $\varepsilon$  wall boundary condition, see Bolio et al. [66]. The particle-phase mean velocity boundary condition is determined by equating the lateral momentum flux transmitted to the wall by particle-wall collisions with the tangential stress in the particle-phase next to the wall; Bolio et al. [66]. Similar to the particle velocity, the wall boundary condition for the pseudo-thermal temperature  $T$  is determined by equating the energy conducted to the wall by particle-particle collisions with the energy dissipation due to the inelastic particle-wall collisions and the energy generated by particle slip at the wall; Johnson and Jackson [68]. An adaptation of the implicit finite volume technique created by Patankar [69] can be used to solve the system of equations.

### **Results**

Figure 3-1 compares the Bolio model (which neglects lubrication effects) for predictions of the solids fluctuating velocity with the gas-solid experimental data of Tsuji [5]. The flow was comprised of 243  $\mu\text{m}$  particles with a density of 1020  $\text{kg/m}^3$  at a

loading of 3.4 and  $Re \sim 2.0 \times 10^5$ . This results in Bagnold and Stokes numbers of approximately 1500 and 58, respectively. The model does a good job predicting the solid turbulence under these conditions, which are dominated by the inertial forces of the solid particles.

Figure 3-2 compares the model solids fluctuating velocity with the liquid-solid experimental data of Alajbegović [16] at  $Re = 6.7 \times 10^4$ . In this case the solid-phase is glass particles of density  $2500 \text{ kg/m}^3$  and diameter of 2.32 mm. Under these conditions the Bagnold number is approximately 1000 and the Stokes number 38. The model now significantly over predicts the solid-phase turbulence due to the increase in viscous forces. As the flow moves more into a transitional regime where viscous forces become more significant, the model is no longer able to predict the flow. These two figures display the need for improved models and the experimental data with which they can be validated.

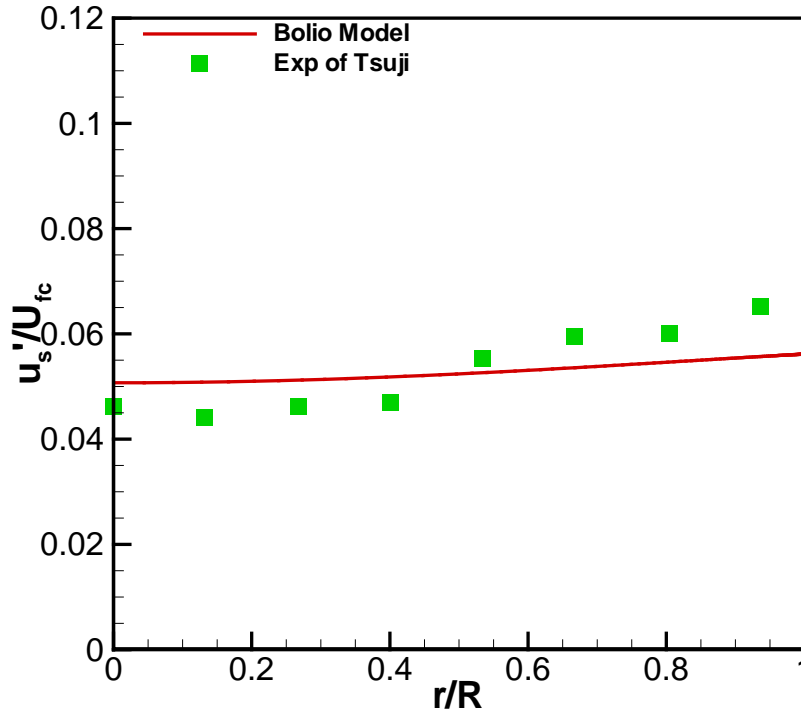


Figure 3-1. Solid fluctuating velocity of gas-solid flow of 243  $\mu\text{m}$  polystyrene particles at  $\text{Re} \sim 2.2 \times 10^4$  (Tsuji et al. [67])

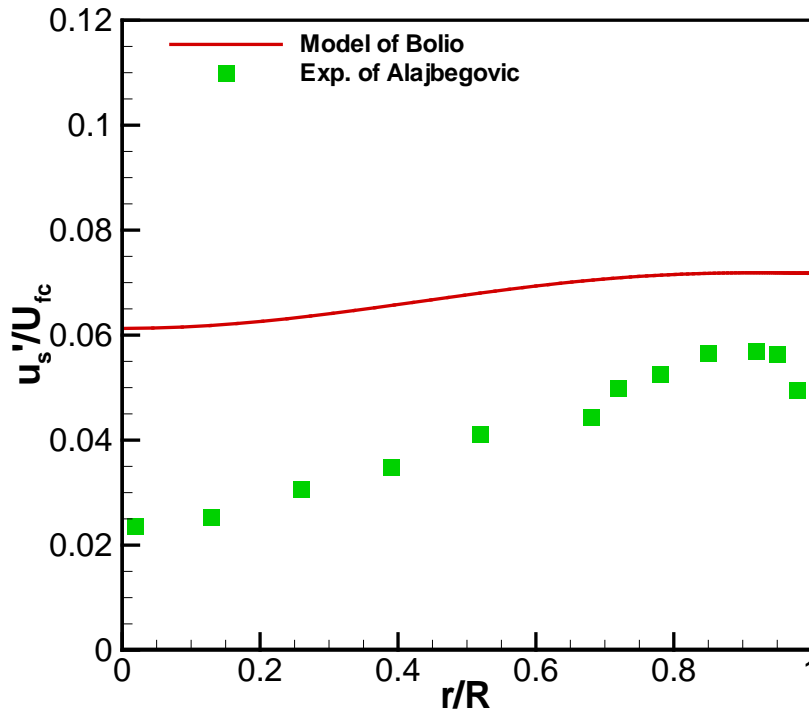


Figure 3-2. Solid fluctuating velocity of liquid-solid flow of 2.32 mm glass particles at  $\text{Re} = 6.7 \times 10^4$  (Alajbegović et al. [16])

## CHAPTER 4 PRESSURE LOSS IN PIPE BENDS OF LARGE CURVATURE AT HIGH RE

### Introduction

Curved pipes are ubiquitous in industrial and laboratory settings. Understanding fluid flow in bends is relevant to heating and air conditioning systems, engine intake and exhaust, heat exchangers, commercial pipelines, and blood flow through arteries. In comparison to a straight pipe, flow through a bend may experience a greater pressure drop over an equivalent pipe length due to flow separation. This flow separation is marked by secondary flow that moves the faster moving fluid to the outside of the bend and the slower to the inside—as dictated by an increase in pressure along the outer wall of the bend and a decrease in pressure along the inner wall. The sharper the bend, the more dramatic the flow separation, such that in very long radius bends, wall friction dominates and flow separation has a negligible effect on pressure loss. Over intermediate radii of curvature, both factors – wall friction and flow separation – are significant.

The flow through a bend is a function of the Reynolds number  $Re$  and the radius of curvature,  $R_b/R$ . (In this paper, ‘bend’ describes both elbows with  $R_b/R < 20$ , as well as curved pipes with  $R_b/R > 20$ .) Laminar and turbulent flow through pipe bends has been reviewed by Berger et al. [70] and Ito [71]. Pressure loss in a pipe bend is often characterized by the pressure loss coefficient  $K$  defined as

$$K = \frac{P - P_{ref}}{0.5\rho_f U_f^2} \quad (4-1)$$

where  $U_f$  is the mean fluid velocity,  $\rho_f$  the fluid density, and  $P_{ref}$  is a reference pressure measured upstream from the bend. Another method of characterizing pressure loss in a bend is the total bend loss coefficient  $k_t$

$$k_t = 2g \frac{\Delta h_t}{U_f^2} \quad (4-2)$$

where  $\Delta h_t$  is the change in pressure associated with points D and F on Figure 4-1 and  $g$  is gravity. Point F is the pressure at some location  $X^*$  downstream of the bend where the pressure gradient is the same as the pressure gradient upstream of the bend. Point D is the pressure at the same location  $X^*$  if the bend were not present.

$K$  and  $k_t$  are two different conventions for describing pressure loss in a pipe bend. The pressure loss coefficient  $K$  and the total bend loss coefficient  $k_t$  are employed in the present work to be consistent with other studies of flow in pipe bends, particularly Ito [72]. Figure 4-1 is included to give a physical description of  $k_t$  and is modeled after a similar figure in Ito [72].  $k_t$  gives a total bend loss and can be used to measure pressure loss as a function of  $Re$ ,  $R_b/R$ , or degree of bend.  $k_t$  is also the pressure loss computed in numerical correlations. The pressure loss coefficient  $K$  is a method of normalizing pressure data and shows the pressure profile in a bend.

Various experimental correlations have been proposed for the total bend loss coefficient. The empirical correlation of Ito [72] gives the total bend loss coefficient for  $Re(r/R)^2 > 91$  as

$$k_t = 0.00241\alpha\theta_b Re^{-0.17} \left( \frac{R_b}{r} \right)^{0.84} \quad (4-3)$$

where  $\theta$  is the bend angle in degrees and  $\alpha$  is an empirical factor which depends on the radius of curvature. For large curvature bends,  $R_b/rR > 19.7$ ,  $\alpha = 1$ . The Ito [72]

correlation is based on data in pipe bends with large curvature (up to 58) and  $Re < 3 \times 10^5$ . In addition, the correlation proposed by Miller [73] estimates  $k_t$  as

$$k_t = k_t^* \cdot C_{Re} \cdot C_o \cdot C_f \quad (4-4)$$

where  $k_t^*$  is a function of  $R_b/R$  and  $\theta$  at  $Re = 10^6$  and  $C_{Re}$ ,  $C_o$ , and  $C_f$  are correction factors based on  $Re$ , length of the downstream tangent, and pipe roughness, respectively. According to Miller [73], this correlation can be applied for pipe curvature  $R_b/R < 20$  over a range of  $Re (< 10^7)$ . Both the Ito [72] and the Miller [73] correlation predict that the total bend loss coefficient increases with increasing pipe curvature and decreasing  $Re$ . Another well known correlation for  $k_t$ , published by the Crane Company [74], predicts  $Re$  independence, assuming fully turbulent flow.

Table 4-1 gives a summary of published experimental data on flow in  $90^\circ$  and  $180^\circ$  pipe bends. Based on these data, a number of conclusions about flow and pressure loss in pipe bends have been developed. Ito [72] observed a decrease in the total bend loss coefficient  $k_t$  with increasing  $Re$  at a given radius of curvature, and an increase in  $k_t$  with increasing radius of curvature for a given  $Re$ . The length of the upstream and downstream tangents was also investigated, and 50 pipe diameters after the bend were required for the flow to return to a fully developed state, regardless of the bend geometry. Ito [72] also found that the total bend loss coefficient increased with increasing length of upstream tangent, with a minimum of 20 pipe diameters required for consistency with his empirical correlation given in equation 4-3. Rowe [75] mapped total pressure and fluid velocity in and downstream of a pipe bend. The pressure at the outside of the pipe bend was higher than on the inside of the pipe bend. Secondary flows reached a maximum at  $30^\circ$  and then decreased until  $90^\circ$ , where some local flow

reversal was observed. Anwer et al. [76], Anwer and So [77], and Sudo et al. [78, 79] investigated upstream effects associated with pipe bends. In each of these studies, only one set of operating conditions (Re and pipe curvature) was studied. Anwer et al. [76] observed mean flow asymmetry and an increase in all three components of the normal stress over the pipe one pipe diameter upstream of the bend. In addition, Anwer and So [77] identified the beginning of a nonlinear pressure gradient developing about 4 pipe diameters upstream of the bend, in line with the outside of the bend. Sudo et al. [78, 79] showed mean flow asymmetry and pressure gradient nonlinearity developing between 1 and 0.5 diameters upstream of a bend. Crawford et al. [80] also investigated upstream effects but over range of Re and pipe curvatures. They concluded that a nonlinear pressure gradient begins about five pipe diameters upstream of the bend, regardless of the radius of curvature. Crawford et al. [80] also found that the length of straight pipe required for fully developed flow in the downstream tangent increased with decreasing bend curvature ratio. Finally, their experimental data for total bend loss coefficient exceeded predictions based on Ito's [72] correlation. Coffield et al. [81] investigated flow in pipe bends at higher Reynolds numbers (up to  $2.5 \times 10^6$ ) than previous investigations. They found significant deviation between their measurements of total bend loss coefficients and predictions based on existing correlations (such as equation 4-3) which are designed for flows with lower Reynolds numbers. Hawthorne [82] determined that secondary flows in pipe bends are oscillatory, marked by periodic changes in the direction of circulation.

Despite all of these previous investigations, there is a lack of experimental data for flow in pipe bends of large curvature at high Reynolds number ( $Re > 3 \times 10^5$ ). While

Coffield et al. [81] investigated high Re flow in pipe bends, the radius of curvature in their experiments was low ( $< 3$ ). In addition, Coffield et al. [81] did not study upstream effects as in this present work. Furthermore, the present study looks into the influence of a sudden expansion at the outlet of a pipe bend—as opposed to a continuation of straight pipe section.

### **Experimental**

Water flow was investigated in a  $180^\circ$  vertical bend consisting of two  $90^\circ$  bends, each with  $R_b/R = 24$ . The water was unfiltered tap water at a temperature of  $23^\circ\text{C}$ . The two  $90^\circ$  bends were connected by a straight horizontal section seven pipe diameters in length. The pipe was three inch nominal (78 mm) schedule 40 stainless steel. The pipe bends were made by the roll bending method which produces very little cross sectional distortion. A diagram of the experimental setup is given in Figure 4-2. The Re was varied from  $3.68 \times 10^5$  to  $8.50 \times 10^5$ . Pressure taps were placed on the inside and outside of the first  $90^\circ$  bend at its entrance and every  $18^\circ$  thereafter—or approximately every four pipe diameters throughout the bend. Additionally, inside and outside taps were placed two diameters upstream, and two and seven diameters downstream, of the first  $90^\circ$  bend. Finally, taps were placed inline with the outside of the bend every 5 diameters upstream of the first  $90^\circ$  bend and provided pressure measurements up to 37 pipe diameters upstream. Before entering the bend, 67 pipe diameters allow the flow to become fully developed; this was confirmed via LDV measurements.

Pressure taps were 1.0 mm in diameter. Threaded couplings were welded over the holes, and pressure gauges were screwed into the couplings. The pipe wall thickness was over 5 times the tap diameter, so the water in contact with the gauge was assumed to be quiescent. The gauges had a range of 0–15 PSI (0–103 kPa) with a

digital readout to the hundredths place, an accuracy of  $\pm 0.1\%$  of the full scale and readings occurring at 3 Hz (smaller than the data point size on Figures 4-3 and 4-4). The pressure was determined by taking an average over 30 seconds. Pressure fluctuations increased with increasing Re, and were consistently less than 4%. The Re was determined by a magnetic flow meter. Fluctuations in the flow meter reading were always less than 2% of the mean flow. A 50 HP centrifugal pump pumped the water and was controlled via a variable frequency drive.

Experiments were conducted with two different pipe configurations downstream of the second 90° bend. Configuration A involved a continuation of the 78 mm I.D. stainless steel pipe used throughout the flow loop. Configuration B utilized a PVC pipe that expanded in diameter from 78 mm to 156 mm via two bushings, discharging the fluid to atmosphere. In both cases, the downstream tangent was 22 pipe diameters in length.

## Results and Discussion

Pressure measurements in Figures 4-3 and 4-4 are presented as pressure loss coefficients K with  $P_{ref}$  equal to the pressure 37 pipe diameters upstream of the first 90° bend. The pressure measurements are also adjusted to take into account the vertical height difference  $\Delta z$

$$P = P_{meas} - \rho_f g \Delta z \quad (4-5)$$

where  $P_{meas}$  is the measured tap pressure.

Figure 4-3A shows pressure loss coefficients upstream of the first 90° pipe bend as a function of Re for downstream Configuration A (continuation of the straight pipe section). At the lowest Re investigated, the pressure gradient is linear approaching the

first 90° bend and upstream effects are minimal, consistent with previous investigations. However, as the  $Re$  starts to increase, the loss coefficient profile begins to flatten approaching the bend. Hence, upstream effects (i.e. deviations from the linear pressure gradient associated with fully developed flow) become pronounced, increase significantly with increasing  $Re$ , and extend well beyond a few pipe diameters upstream of the bend. This result is in stark contrast with the results of previous investigations at lower  $Re$  which are summarized by Ward-Smith [83]—“variations in pressure due to the presence of the bend start to occur in the upstream tangent at a value...of between -1 and -2 [pipe diameters]”. Figure 4-3B gives the pressure loss coefficients upstream of the first 90° pipe bend for downstream Configuration B (sudden expansion at the outlet); these pressure loss coefficients are virtually identical to those with Configuration A. Hence, upstream effects significantly increase with increasing  $Re$ , regardless of downstream configuration.

As seen in Figures 4-3 and 4-4, the trend of increasing  $K$  as a function of  $Re$  is consistent with equation 4-1; there is a second order dependence on mean velocity in the pressure in the numerator. When combined with a first order dependence between pressure and velocity as described by the Navier-Stokes equation, an inversely linear relationship between  $Re$  and  $K$  results.

### **Influence of Downstream Tangent: Configuration A**

Figure 4A presents the loss coefficients through the pipe bend for downstream Configuration A. The vertical lines in the figure indicate the entrance and exit points of the bend. Throughout the pipe bend, the pressure on the inside of the pipe is less than that on the outside. This pressure difference is also present at the entrance to the bend. Previously published results (Crawford [80]) show that this pressure difference is

largely a function of pipe curvature; the present results also indicate a weak dependence on  $Re$ . The pressure difference between the inside and outside of the pipe increases slightly with increasing  $Re$ .

This difference between the inside and outside pressure decreases significantly approaching the bend exit. In the connecting pipe, the inside pressure becomes greater than the outside pressure. The reversal in pressure difference is likely associated with a reversal in the direction of the secondary flow, as identified by Rowe [75] and Hawthorne [82]. The present results indicate that this pressure difference downstream of the bend has a weak dependence on  $Re$ ; the pressure difference increases slightly with decreasing  $Re$ .

Despite the pressure drop evidence for the existence of secondary flow, there is a minimal contribution from the pipe curvature to the total bend pressure loss. The loss coefficient profile follows the pressure change associated with points B and E on Figure 4-1; the pressure gradient is approximately linear throughout the bend, regardless of  $Re$ . This result is consistent with Rowe [75] who observed secondary flows in pipe bends with large curvature ( $R_b/R = 24$ ) at a given (lower)  $Re$ , but noted that secondary flows did not contribute to the total bend pressure loss.

Comparisons of the measured total bend loss coefficient to the predictions from the empirical correlations of Ito [72], Miller [73], and the Crane Company [74] are displayed in Table 4-2. The total bend loss coefficients were determined via regression using an average of the inside and outside pressure at each location downstream from the bend entrance. All correlations significantly under predict the total bend loss. The correlations of Ito [72] and Miller [73] and the experiments show a decrease in total

bend loss coefficient with increasing  $Re$ , but the significant variation is not captured by the correlation. At the range of  $Re$  investigated in the present work, the correlations predict only a very slight decrease in  $k_t$  with increasing  $Re$  (Ito [72] and Miller[73]) or none at all (Crane Company [74]).

Ito [74] found good agreement with experiments in bends of  $45^\circ$ ,  $90^\circ$ , and  $180^\circ$  at  $Re$  from  $2 \times 10^4$  to  $4 \times 10^5$  and  $R_b/R$  values from 3.7 to 25. However, the  $Re$  range of the present investigation is outside the range of experimental data on which the correlation of Ito [72] is based. In addition, the pipe curvature employed in the present study,  $R_b/R = 24$ , is outside the range of the Miller [73] correlation. Unfortunately, Miller [73] and the Crane Company [74] did not compare their respective correlations with experimental data. From previous investigations (Ito [72]), it is known that  $k_t$  increases with increasing curvature. Crawford et al. [80] investigated larger pipe curvatures and also found that the correlation of Ito [72] under predicted the total bend loss coefficient.

### **Influence of Downstream Tangent: Configuration B**

Figure 4-4B presents the loss coefficients through the bend for Configuration B - the case where the water is allowed to freefall from the second  $90^\circ$  bend. The pressure measurements are consistent with those in Configuration A upstream of the bend and up to four diameters through the bend. However, at this point in the bend, the pressure on the inside of the pipe increases, such that it surpasses the pressure on the outside of the pipe by eight diameters through the bend.

By the next pressure tap, twelve diameters through the bend, the inside pressure is again lower than that on the outside. Finally, at sixteen pipe diameters through the bend, the inside pressure surpasses that on the outside and remains larger through the end of the bend and into the downstream tangent. This unusual pattern of pressure

reversal is likely associated with a highly complex secondary flow pattern in the bend. Since the pressure measurements in Configuration A (Figure 4-4A) and Configuration B (Figure 4-4B) were obtained at the same  $Re$ , the difference in flow behavior is associated with the change in the downstream configuration. In Configuration B, the loss coefficient—based on an average of the inside and outside pressures of the bend—also varies linearly throughout the bend as with Configuration A. Thus, even though the flow disruptions propagate throughout the bend, the secondary flows do not affect the overall pressure drop in the bend in a significant way.

### **Conclusion**

Pressure data are presented for flow in pipe bends at a novel combination of conditions - large pipe curvature with high  $Re$ . A number of interesting observations associated with these conditions are made:

Upstream effects occur well beyond a few pipe diameters prior to a pipe bend provided the  $Re$  is sufficiently high.

Through the pipe bend, as well as downstream of the pipe bend, the pressure difference between the outside and the inside of the pipe is weakly dependent on  $Re$ .

Correlations for total bend pressure loss significantly under predict the pressure drop in the bend and fail to capture a decrease in  $k_t$  with increasing  $Re$ .

In addition, the following conclusions result from the investigation of two different exit configurations:

Upstream effects are not dependent on the downstream exit configuration.

A sudden expansion downstream of a bend is associated with a complex outside and inside pressure pattern in the pipe bend.

Independent of exit configuration, the pressure on the outside of the bend increases, surpassing that of the pressure on the inside of the bend, at the bend exit and downstream of the bend.

Independent of exit configuration, the loss coefficient varies linearly throughout the bend, signifying that the effective length of the pipe is equal to its actual length, and wall friction is the dominant process contributing to pressure loss in bends of  $R/r \geq 24$ .

Table 4-1. Published experimental pressure loss data in pipe bends

Author	Re	$R_b/R$	$\theta$	In Bend	Angular Position	Upstream Locations	Downstream Locations
Ito [74]	$2 \times 10^4$ to $\sim 3.5 \times 10^5$	2	90	0	inside,	0, 7.8,	0, 9.3, 17.8,
		3.66	90	0	outside,	15.0,	27.6, 41.4,
		6.59	90	$\theta/2$	top,	22.2,	54.3, 61.6,
		3.68	180	0	bottom	30.8	71.6
		6.52	180	$\theta/3$			
Rowe [77]	$2.36 \times 10^5$	24	90 180	$\theta/4$ $\theta/6$	constant	0	1, 5, 29, 61
Anwer et al. [78] & Anwer and So [79]	$5.0 \times 10^4$	13	180	6 total	inside, outside	0, 1, 4, 18	9 total, up to 50
Sudo et al. [80]	$6.0 \times 10^4$	4	90	$\theta/3$	inside, outside, bottom	0, 0.5, 1	0, 0.5, 1, 2, 5
Sudo et al. [81]	$6.0 \times 10^4$	4	180	$\theta/12$	inside (90° 45°), outside (90° 45°), bottom	0, 0.5, 1	0, 0.5, 1, 2, 5
Crawford et al. [82]	$2.0 \times 10^4$ to $1.26 \times 10^5$	1.3 5 20	90 90 90	$\theta/2$ $\theta/2$ $\theta/4$	inside, outside	0, 5, 10, 50, 90	0, 5, 10, 20, 30, 40, 50, 60, 70, 90
Coffield et al. [83]	$1 \times 10^5$ to $2.5 \times 10^6$	2.4 3	90 90	$\theta/4$ $\theta/4$	inside, outside, bottom	0, 1, 2, 5, 10, 15, 19	0, 1, 4, 7, 10, 15, 20, 25, 20
Hawthorne [84]	$1.7 \times 10^5$	3 10	90 180	0 $\theta/6$	constant every 30°	0 0	0, 2.7, 7.3, 10, 16 0, 4.2

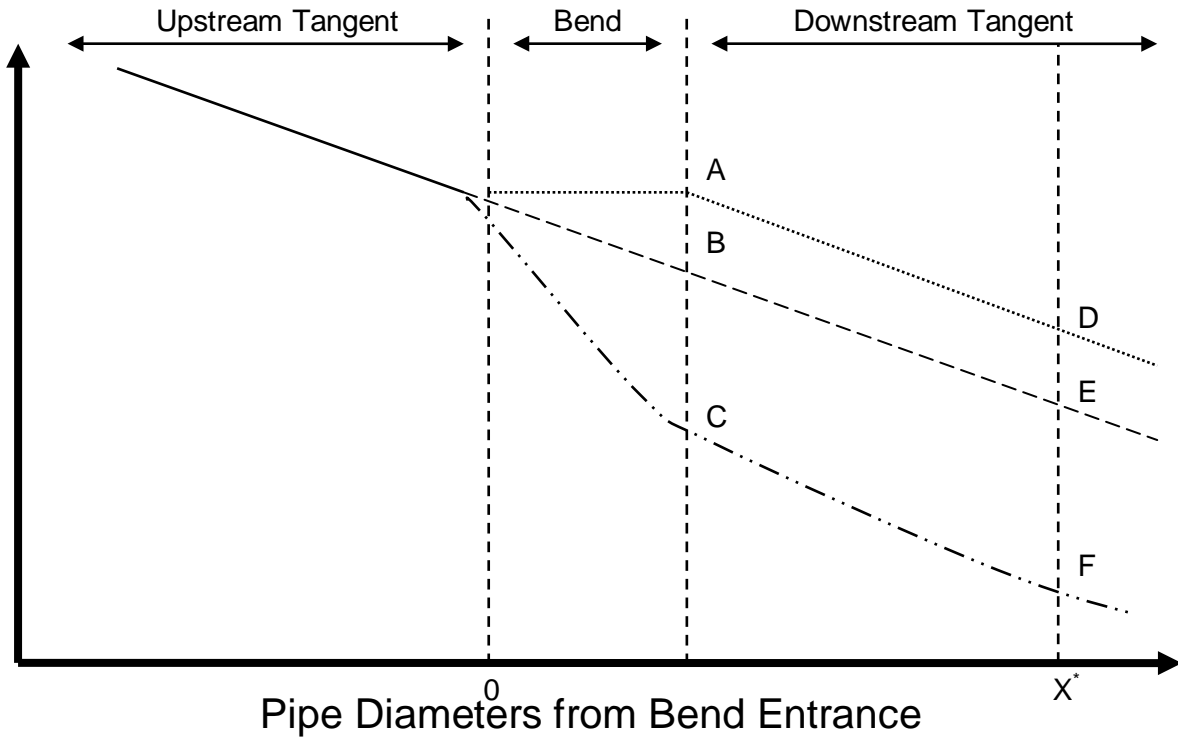


Figure 4-1. Loss coefficient profiles: (....) no bend present; (- - -) no additional pressure loss due to bend; (- .. - .. -) additional pressure loss due to bend

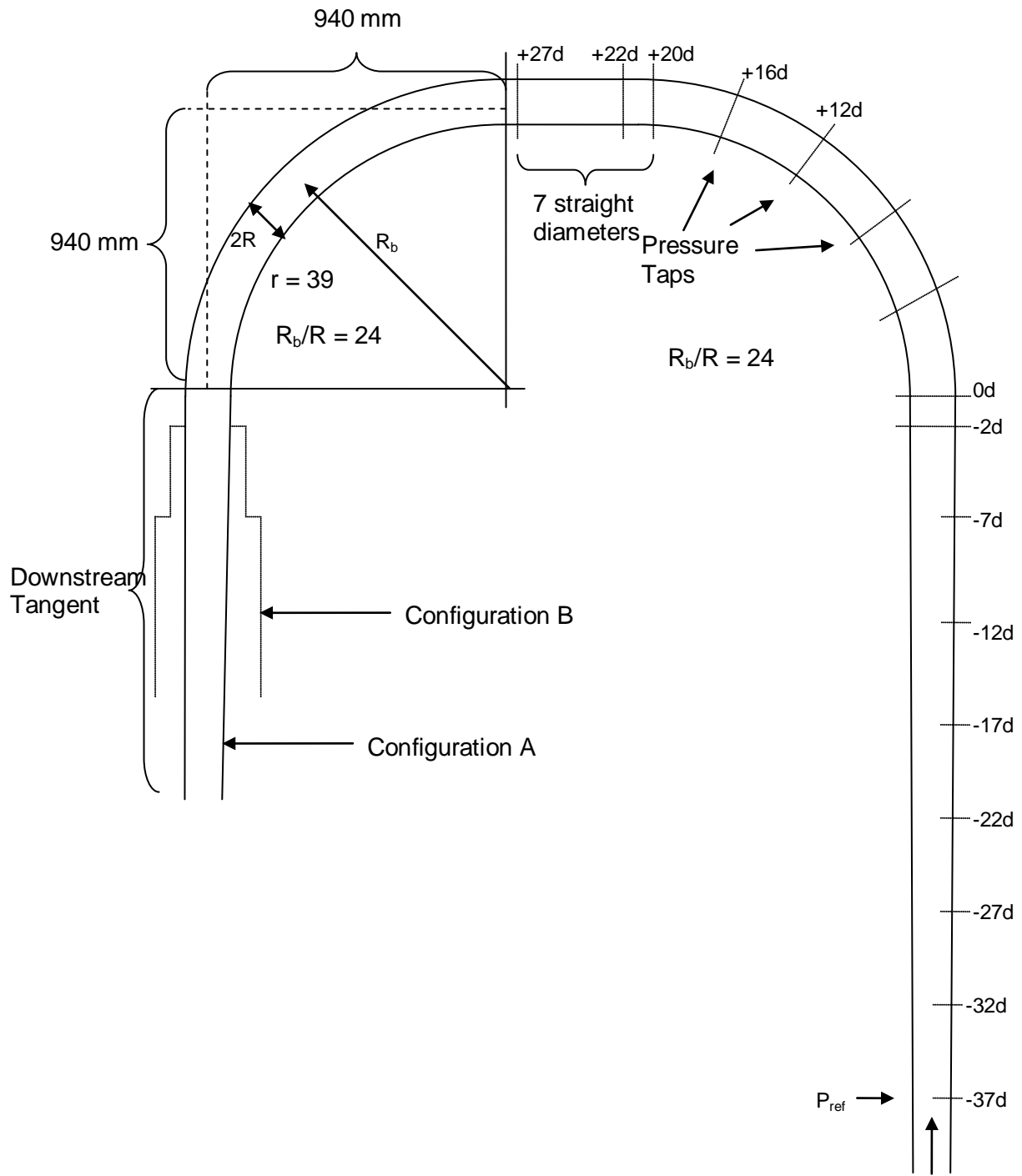


Figure 4-2. Bend geometry and discharge configurations

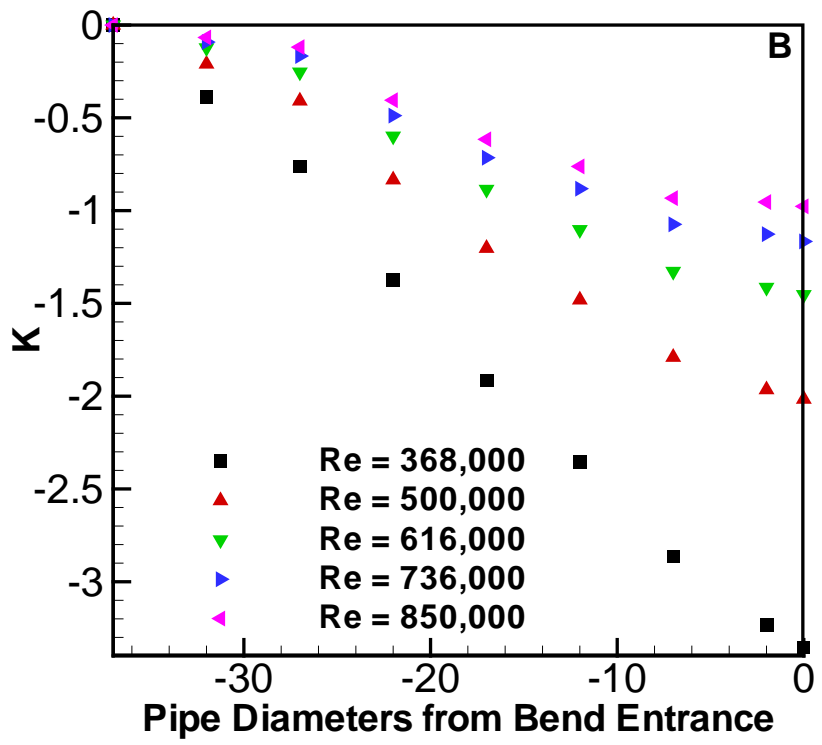
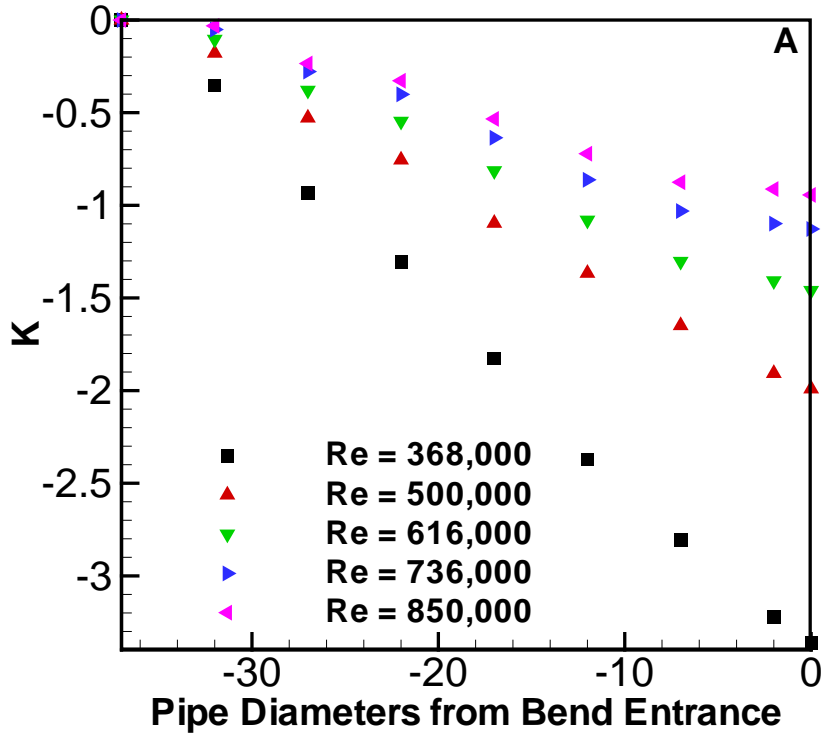


Figure 4-3. Loss coefficient upstream of bend entrance. A) Configuration A and B) Configuration B

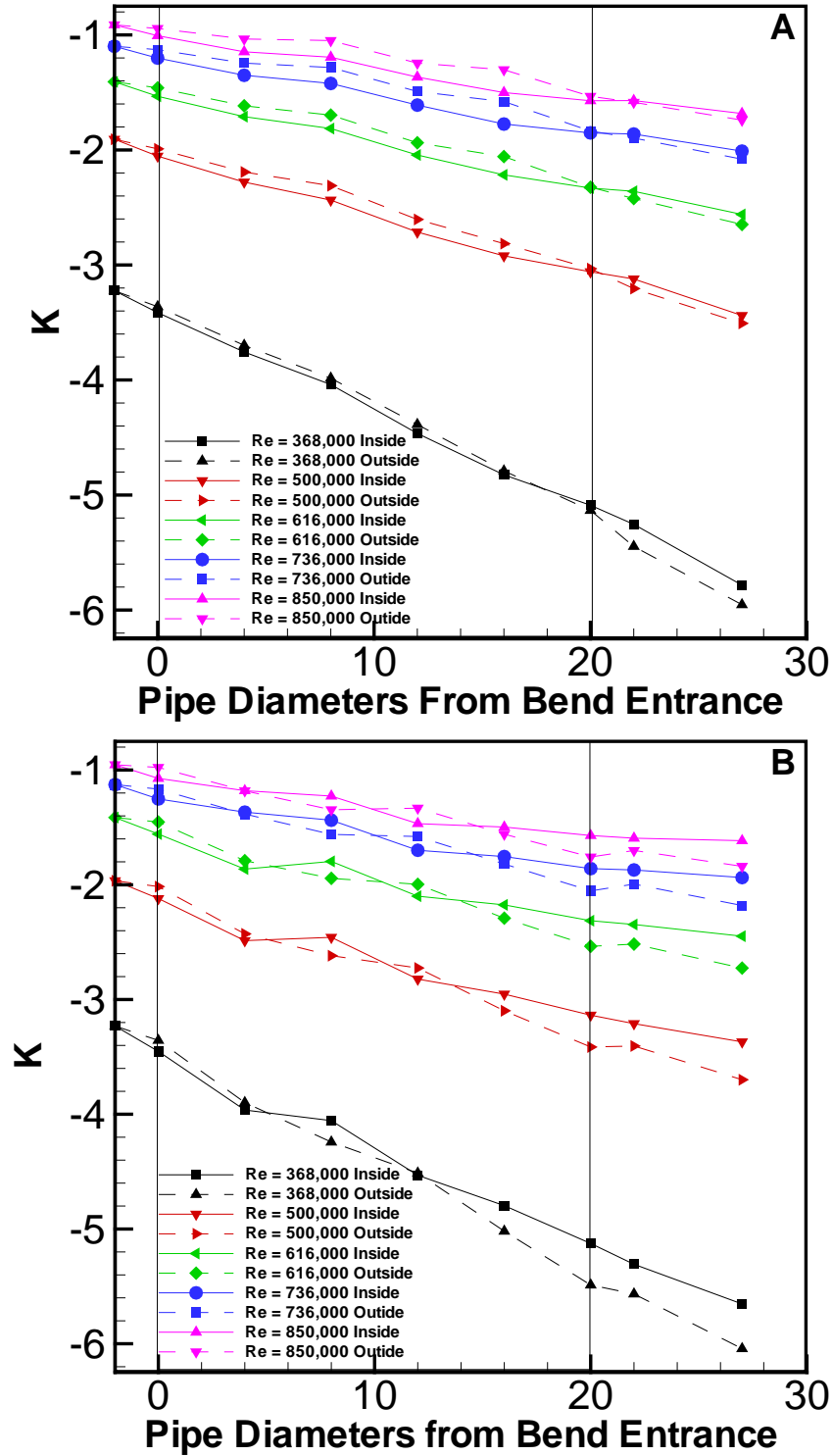


Figure 4-4. Loss coefficient through bend. A) Configuration A and B) Configuration B

Table 4-2. Total bend loss coefficient—comparison between experimental results and predictions from correlations

Re	$k_t$ (Present Work)	$k_t$ (Ito [74])	$k_t$ (Miller [75])	$k_t$ (Crane [76])
$3.68 \times 10^5$	1.81	0.35	0.31	0.61
$5.00 \times 10^5$	1.09	0.34	0.30	0.61
$6.16 \times 10^5$	0.82	0.33	0.29	0.61
$7.35 \times 10^5$	0.64	0.32	0.28	0.61
$8.50 \times 10^5$	0.54	0.31	0.28	0.61

## CHAPTER 5 SINGLE-PHASE VALIDATION

### Introduction

The veracity of current research investigating multiphase flow is often predicated on a single-phase “base-case.” This base-case validation has resulted in frequent citations of the work of Laufer [84] and other benchmark single-phase turbulence papers (Perry and Abell [85], Lawn [86], Schildknecht et al. [87]). Single-phase turbulence data are also available as base-case conditions for prominent two-phase investigations, both in gas (Tsuji [5], Lee and Durst [4]) and in liquid (Nouri et al. [15] and Theofanous and Sullivan [10]). Turbulence measurements using PIV (Van Doorne and Westerweel [88] and Fujiwara et al. [89]) have been made in lower Re flows and compared with available DNS data (Eggels et al. [90], Wu and Moin [91]). More recently, Zhao and Smits [92] and Morrison et al. [93] have conducted single-phase turbulence studies over a large range of Re, with a focus on the wall region. Tables 5-1 and 5-2 summarize the key publications which report single-phase turbulence measurements in air and water flows, respectively.

Perry and Abell [85] identified significant differences between the reported single-phase turbulence measurements currently available in the literature. They cited inconsistent hot-wire measurement techniques, among other factors, as the reason for these discrepancies. Since that time, a host of improved turbulence measurement techniques have been developed—most notably, the non-intrusive methods based on the Doppler Effect.

In this paper, we present an up-to-date review of turbulence measurements in single-phase flow in round pipes and show that significant differences in the reported

values of turbulent intensity persist. In fact, the variation between single-phase turbulence measurements can greatly exceed the magnitude of turbulence modulation, a common and important theme in many two-phase flow research studies. It is the aim of this paper to analyze the variations in these single-phase measurements and extract any common features based on experimental conditions. We focus on the central region of the pipe where the influence of Re and wall effects are minimized. Additionally, we supplement the published single-phase turbulence data by including laser Doppler velocimetry (LDV) measurements of single-phase flow in water at Re higher than previously investigated.

### **Experimental**

Laser Doppler velocimetry (LDV) was used to make single-phase flow experiments in water at five Re:  $1.5 \times 10^5$ ,  $2.27 \times 10^5$ ,  $3.36 \times 10^5$ ,  $5.0 \times 10^5$ , and  $6.16 \times 10^5$ . All the data were collected in a backscatter configuration. However, the distance from the wall was calibrated via a series of forward scatter experiments conducted to determine the wall shear stress and corresponding friction velocity. A lens of focal length 250 mm was used, resulting in a probe volume length (in water) of approximately 2 mm, depending on its location in the pipe.

At  $Re = 5.0 \times 10^5$  measurements were taken along three different radial chords, 90 degrees apart, and then repeated at two different vertical positions, separated by 8 pipe diameters, to verify that the flow was fully developed. The reproducibility between experiments was at least 95% at the fluctuating velocity level. Furthermore, the pressure gradient was constant at the entrance to the test section. Tap water produced an adequate measurement signal without extra seeding. Data were collected at 16 radial positions, with a greater density near the pipe wall. The friction velocity was

determined experimentally from wall shear stress measurements and pressure drop profiles and compared to a low Re k-ε CFD model and Prandtl's universal law of friction for smooth pipes (Prandtl [44]), see Table 5-3.

### Scaling

Unfortunately, the turbulence measurements from the various published works use different scaling to nondimensionalize their results. Hence, in order to compare one published work with another, a uniform scaling must be adopted. Here, the friction velocity is used since it is the most common scaling for turbulence measurements. In published works where the mean, centerline or local velocity are used to scale the turbulence measurements, rather than the friction velocity, its value is deduced from the reported Re using friction factor correlations.

The friction velocity is defined as

$$U_t = \sqrt{\frac{\tau_0}{\rho_f}} \quad (5-1)$$

where  $\rho_f$  is the fluid density and  $\tau_0$  is the wall shear stress, defined as:

$$\tau_0 = \frac{\lambda_s \rho_f U_f^2}{8} \quad (5-2)$$

Here  $\lambda_s$  is the Darcy friction factor and  $U_f$  is the mean fluid velocity. Combining equations 5-1 and 5-2

$$U_t = \sqrt{\frac{\lambda_s U_f^2}{8}} \quad (5-3)$$

The friction factor  $\lambda_s$  can be estimated via Prandtl's universal law of friction for smooth pipes (Prandtl [44]).

$$\frac{1}{\lambda_s} = 2.0 * \log\left(\frac{U_f D \rho_f}{\mu} * \sqrt{\lambda_s}\right) - 0.8 \quad (5-4)$$

where  $D (=2R)$  is the pipe diameter and  $\mu$  is the fluid viscosity. Conditions were assumed to be standard ambient conditions when they were not reported—1 atm pressure and 20°C.

In the cases where the measurements of the turbulent velocity were scaled by the local fluid velocity or the maximum fluid velocity, those values were estimated from the standard turbulent velocity profile (Schlichting [94]).

$$\frac{u}{U_{max}} = \left(\frac{r}{R}\right)^{\frac{1}{n}} \quad (5-5)$$

where  $u$  is the local mean fluid velocity at radial position  $r$ . The value of  $n$  is a relatively weak function of  $Re$  as given in Table 5-4. From equation 5-5, the ratio of the mean to maximum fluid velocity can be derived:

$$\frac{U}{U_{max}} = \frac{2n^2}{(n+1)(2n+1)} \quad (5-6)$$

While the friction velocity affects the magnitude of the reported turbulence measurements, it does not influence the shape of the turbulent velocity fluctuation profiles. By normalizing the scaled fluctuating velocity profiles with their respective centerline values, the shape of the turbulent velocity fluctuation profiles can be easily compared.

## Results

The measurements presented in Tables 5-1 and 5-2 encompass a range of experimental techniques including hot-wire, LDV, particle image velocimetry (PIV), 3-D conical probe, and hot-film anemometry. Table 5-5 lists two well known DNS results to which the experimental data was compared. Pipe diameters range from 15 mm to 302 mm. While the number of radial measurements varies among these published works,

most report an increase in measurement density near the wall and a value for the centerline turbulence intensity. We use various factors to compare and analyze these published data—whether the measurements were made in air or water, whether the measurement were made using intrusive or non-intrusive experimental techniques, as well as other factors including Re and pipe diameter.

### **Effect of Re**

Figures 5-1A and B present axial turbulent velocity measurements in air as a function of distance from the wall  $y$  ( $y=R-r$ ) based on the work of Laufer [84] and Zhao and Smits [92], respectively. Both of these studies show negligible effect of Re on the magnitude of the scaled turbulent velocity fluctuations in the far wall region. The measurements of Perry and Abel [85] (not shown) are also consistent with this observation.

However, in the single-phase flow of water, this observation of Re independence is not the case. Figures 5-2A, B, and C present axial turbulent velocity measurements in water as a function of radial position  $r$  based on the work of Wang et al. [11], Hu et al. [12], and the present study. Although there is no consistent trend in the magnitude of the turbulent velocity fluctuations as a function of Re, in general, the scaled turbulent fluctuations tend to decrease with increasing Re. Unfortunately, the turbulence measurements in water of Toonder and Niewstadt [95] are inconclusive in this regard as their measurements do not uniformly extend into the pipe core.

### **Turbulence Measurements in Air using Hot-Wire**

Although the reported magnitude of the scaled gas turbulent velocity fluctuations in the far wall region does not vary with Re for a given investigation, there are significant variations in the magnitude of the scaled fluctuations between investigations in the

various published works. Figure 5-3 presents measurements of the turbulent velocity profile in air using only hot-wire. In this figure, no estimation for the friction velocity was necessary as all the published works scaled their turbulence measurements with  $U_t$ . The specific measurements shown are those conducted at the highest  $Re$  for each investigation. Also included in this plot are the direct numerical simulation (DNS) results of Wu and Moin [91] at  $Re = 4.46 \times 10^4$ . Between hot wire investigations, there is considerable deviation in the magnitude of the scaled turbulent velocity. The level of these deviations exceed the typical error (5-6%) associated with turbulence velocity measurements using hot wire (Comte-Bellot [95]). In addition, the level of these deviations are on the order of or greater than the magnitude of the turbulent modulation often investigated in multiphase research studies. The deviations in the reported magnitude of the turbulent velocity do not show any trend with pipe diameter or  $Re$ . The DNS results exhibit the lowest velocity fluctuations with the measurements of Laufer [84] at  $Re = 5.0 \times 10^5$  most closely following the DNS results.

### **LDV vs Hot-wire Measurements in Air Flow**

Figure 5-4 shows hot-wire measurements of Figure 5-3 (in gray) along with the LDV measurements in air. Overall, the axial fluctuations measured with LDV are lower than those obtained with hot-wire. This is especially true in the middle of the radius, resulting in velocity profiles obtained using LDV tending to be flatter than profiles obtained using hot-wire. The turbulent velocity data obtained using LDV are more consistent, except for the LDV measurements of Tsuji [5]. Nevertheless, the variation between all of these sets of data is outside of the range of the typical error associated with LDV measurements of fluctuating velocity (4%) (Yanta and Smith [58]). In addition, these LDV data are not in line with the DNS results, except for the measurements of

Tsuji. LDV validation and post-processing techniques are likely responsible for these variations in the data. The validation and post-processing greatly affect which individual seed velocity measurements are included in the final reported measurement for the turbulent velocity.

### **Turbulence Measurements in Water**

Figure 5-5 displays the turbulent velocity profiles in water from nine different sets of measurements. There is significant variation between these measurements at all radial locations. The level of these variations exceeds those in turbulent gas flow measurements. The scaled fluctuations in water vary from 0.8 to 1.2 at the centerline and from 1.4 to 2.0 at  $r/R=0.6$ , with more inconsistency in the measurements at the pipe centerline.

The SPIV (stereoscopic PIV) data of Van Doorne and Westerweel [88] are very similar to the DNS data of Eggels et al. [92] at  $Re = 5.3 \times 10^3$  with the lowest centerline turbulence. However, the PIV data of Fujiwara et al. [90] at  $Re = 1.1 \times 10^4$  are significantly different, with a scaled centerline turbulence velocity that is 44% greater than the measurements of van Doorne and Westerweel [88].

The profiles obtained via a hot-film device by Shawkat et al. [97] and Hu et al. [12] are significantly less smooth than the turbulence profiles obtaining using other experimental techniques. The LDV measurements of Theofanous and Sullivan [10] and Nouri et al. [15] produced the largest values for the turbulent velocity, with the data of Theofanous and Sullivan [10] being well outside the range of all other experimental measurements. Both of these sets of LDV measurements report considerably larger turbulence velocities than the present LDV data; the present data are in the middle of the range of previous investigations. For the LDV data sets, which report turbulence

measurements scaled with the friction velocity, the variations in the turbulence measurements are likely due to the difficulty of measurement of the friction velocity in water. Typically, pressure drop measurements are used to determine the friction velocity. For example, in vertical flow, pressure drop measurements in water are subject to more variations than in air since the wall shear stress contributes much less to the overall pressure drop due to the gravitational force. The importance of an accurate determination of the friction velocity  $U_t$  has also been noted by van Doorne and Westerweel [88] and Eggels et al. [90] among others, because the measurement of  $U_t$  systematically influences the magnitude of the reported measurements.

Figure 5-6 combines all of the turbulence measurements—those conducted in air denoted by pink lines and those conducted in water denoted by blue lines. The DNS results of Wu and Moin [91] are represented with a black line. In general, measurements of turbulent velocity fluctuations in water flow are higher than in air flow.

### **Conclusion**

There is significant variation in the reported values of single-phase gas turbulence intensity among the commonly cited references of these measurements. In both gas and liquid flow, this variation exceeds typical errors associated with the flow measurement techniques. The magnitude of the turbulence velocity fluctuations in water is consistently higher than in air at the same  $Re$ . In addition, the magnitude of the variations in the measurements of turbulent velocity is greater in liquid versus gas flow. In air, the turbulent velocity exhibits no  $Re$  dependence far from the wall; in water, there is a  $Re$  dependency. Finally, due to the intrusive nature of the hot-wire probes, there is a bias in the LDV versus hot-wire measurements. In air, turbulent velocity profiles

measured using LDV are consistently flatter than those obtained from hot wire measurements.

Based on these conclusions the single-phase measurements were deemed to be in agreement with established values, proving the suitability of the experimental flow facility and instrumentation for two-phase experiments.

Table 5-1. Turbulence measurements in air

	Re	Pipe D. (mm)	Fluid	Method	Scaling Quantity
Zhao and Smits [92]	6,100,000 4,300,000 1,100,000 480,000 230,000 140,000 110,000	129	Air	Hot-Wire	$U_t$
Laufer [84]	500,000 50,000	254	Air	Hot-Wire	$U_t$
Perry and Abell [85]	257,000 173,000 133,000 78,000	111	Air	Hot-Wire	$U_t$
Lawn [86]	250,000 164,000 90,000 38,000	144.3	Air	Hot-Wire	$U_t$
Schildknecht et al. [87]	17,250	50	Air	Hot-Wire & Pitot	$U_t$
Sheen et al. [6]	32,500	52	Air	LDV	Mean Velocity
Tsuji et al. [5]	22,000	30	Air	LDV	Centerline Velocity
Maeda et al. [3].	20,000	56	Air	LDV	Local Velocity
Lee and Durst [4]	13,000	41.8	Air	LDV	Centerline Velocity

Table 5-2. Turbulence measurements in water

	Re	Pipe D. (mm)	Fluid	Method	Scaling Quantity
Present Data	610,000 500,000 360,000 220,000 110,000	76	Water	LDV	Ut
Shawkat et al. [97]	148,000 43,500	200	Water	Hot-film	Local Velocity
Nouri et al. [15]	59,200	25.4	Water	LDV	Mean Velocity
Hu et al. [12]	57,000 38,000	38	Water	Hot-film	Centerline Velocity
Toonder and Nieuwstadt [95]	24,600 17,800 10,000 4,900	40	Water	LDV	Ut
Wang et al. [11]	44,000 34,000 23,000	57.15	Water	3-D Conical Probe	None
Theofanous and Sullivan [10]	14,000	57	Water	LDV	Local Velocity
Fujiwara et al. [89]	11,000	44	Water	PIV/LIF	Ut
Van Doorne and Westerweel [88]	5,300	40	Water	SPIV	Ut

Table 5-3. Comparison of friction velocity values

Re	$dp/dz$ (m/s)	Law of Wall (m/s)	Prandtl [44] (m/s)
$2.2 \times 10^5$	0.112	0.108	0.112
$3.6 \times 10^5$	0.185	0.168	0.181
$5.0 \times 10^5$	0.255	0.225	0.239
$6.1 \times 10^5$	0.313	0.268	0.293

Table 5-4. Ratio of mean to maximum velocity, power law exponent

$n=f(Re)$	6	7	8	9	10
U/U <sub>max</sub>	0.791	0.817	0.837	0.852	0.865

Table 5-5. DNS turbulence data

	Re	Pipe D. (mm)	Fluid	Method	Scaling Quantity
Eggels et al. [90]	5,300	DNS	DNS	DNS	$U_t$
Wu and Moin [91]	44,600	DNS	DNS	DNS	$U_t$

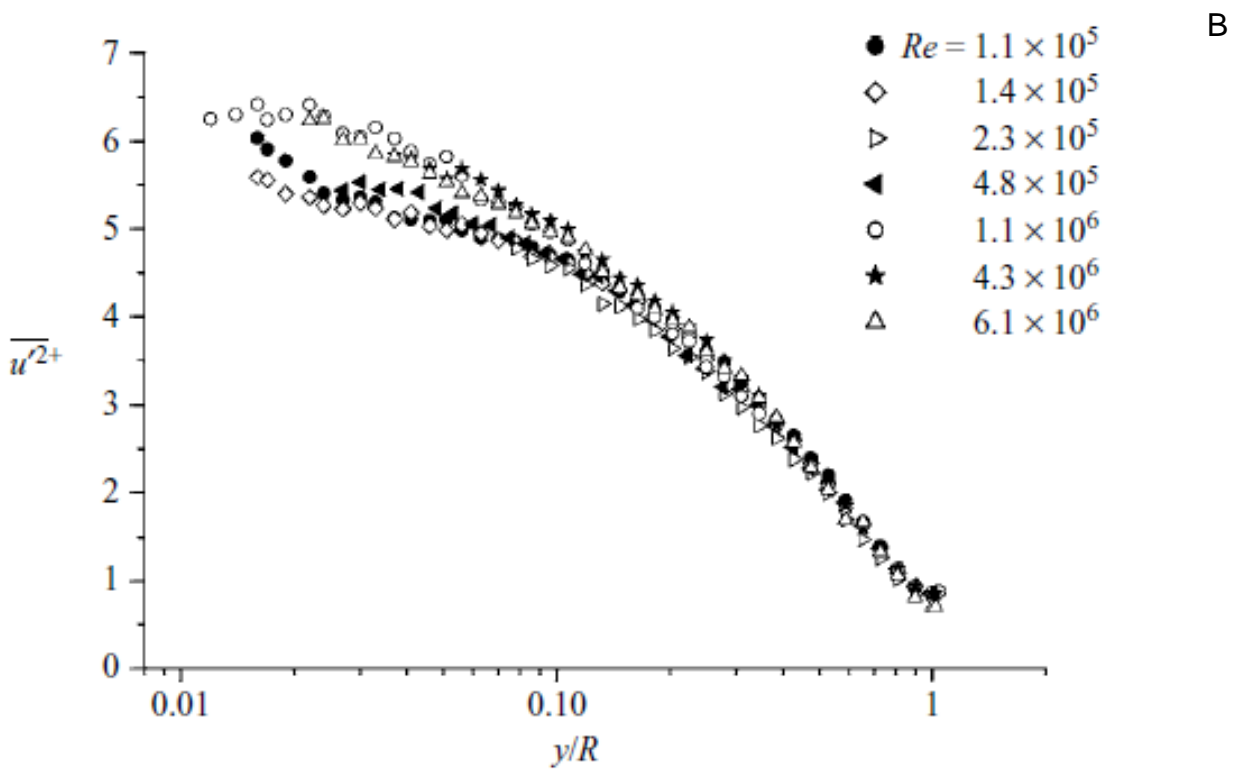
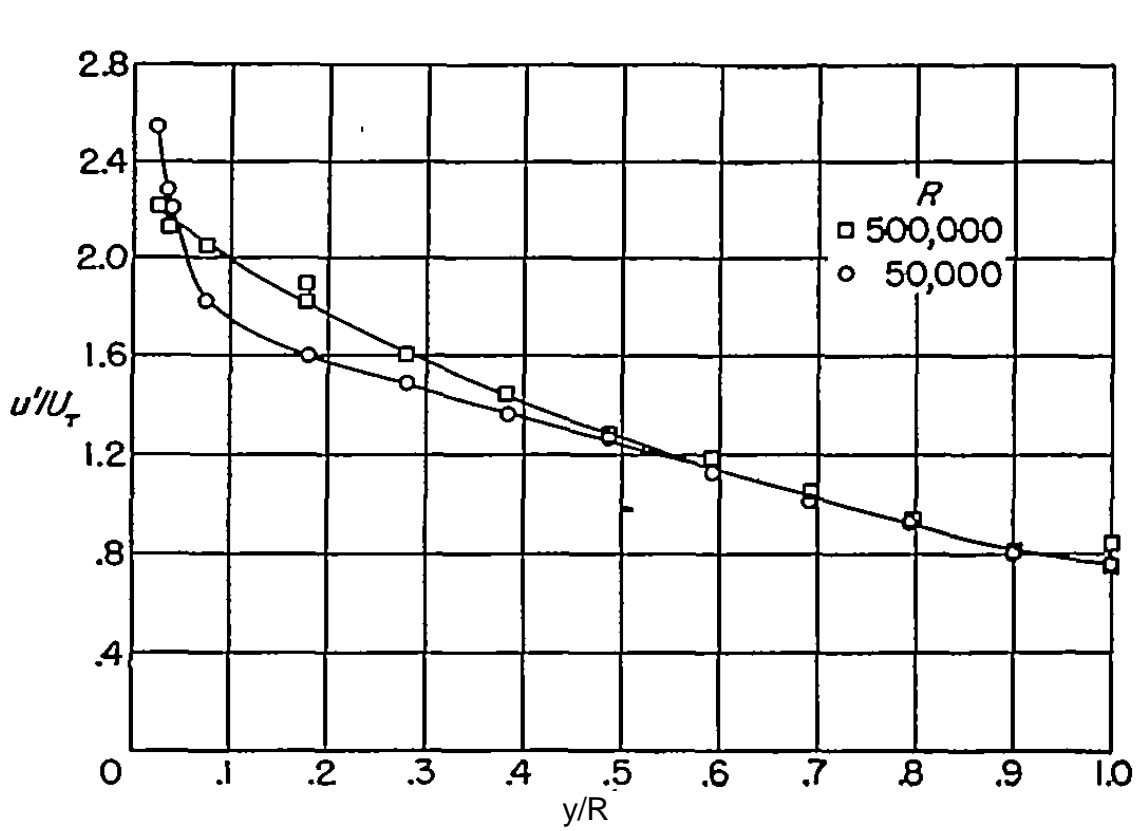


Figure 5-1. Effect of Reynolds number in air measurements. A) Laufer [84] and B) Zhao and Smits [92]

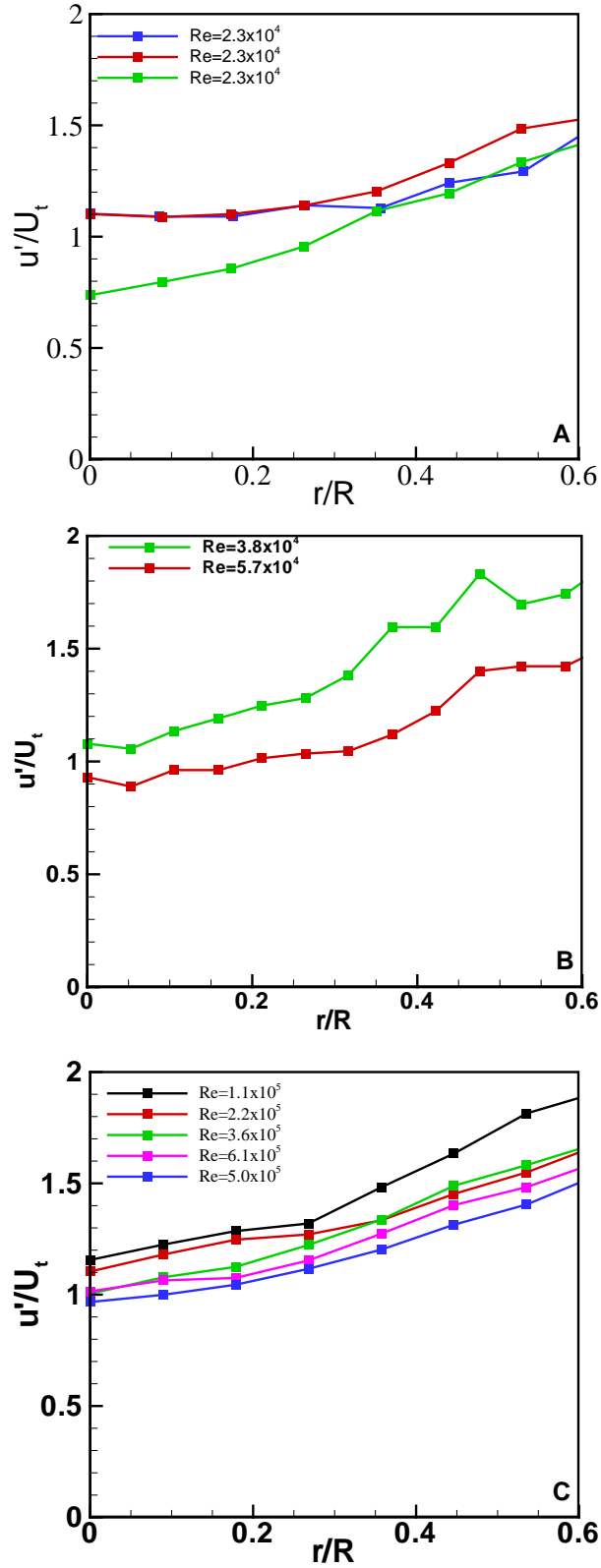


Figure 5-2. Effect of Re in water measurements. A) Wang et al. [11], B) Hu et al. [12] and C) present data

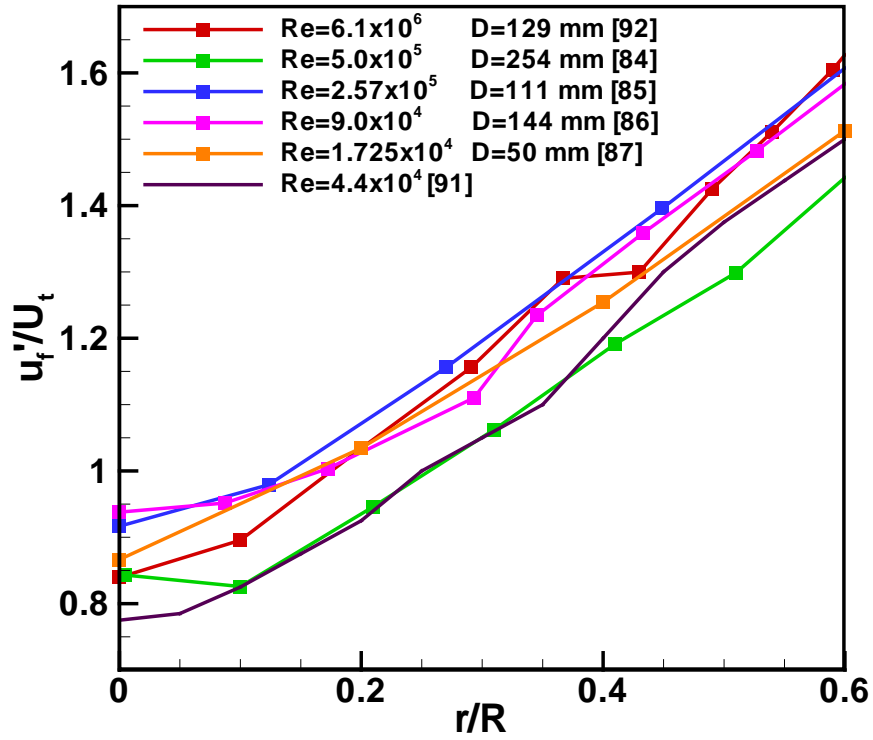


Figure 5-3. Effect of pipe diameter

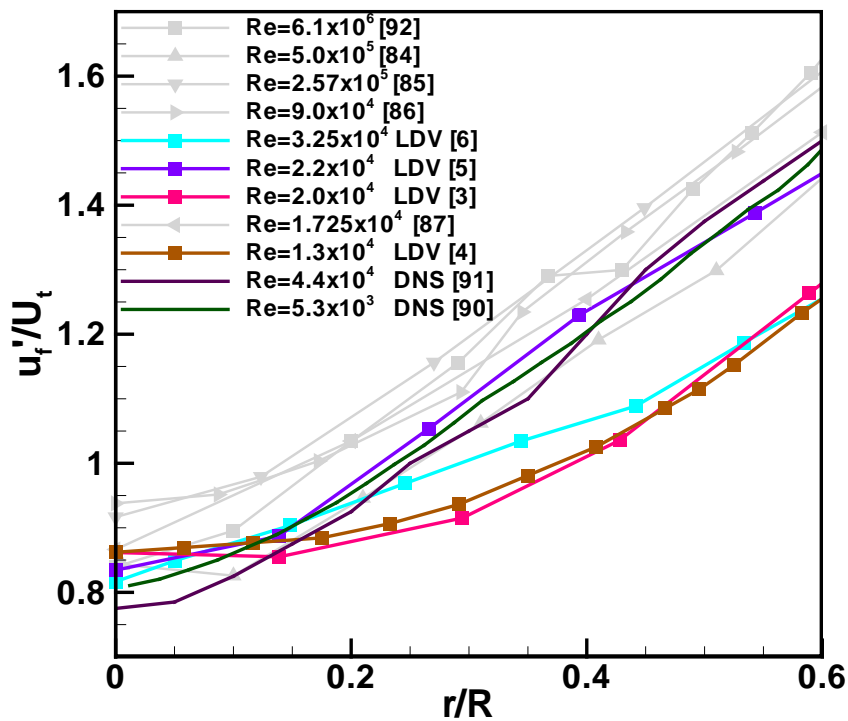


Figure 5-4. LDV vs. hot-wire measurements in air

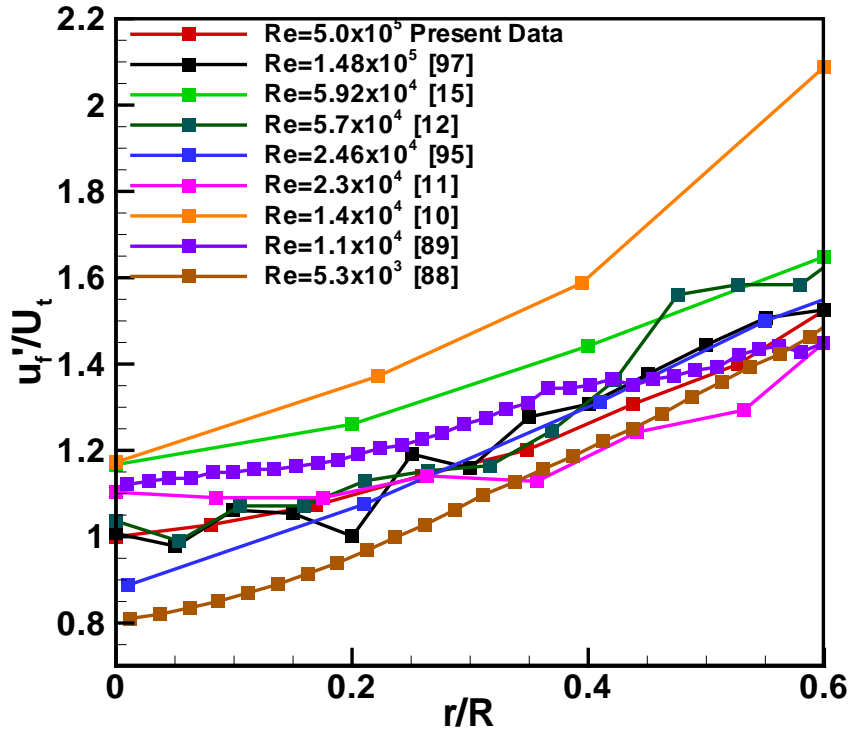


Figure 5-5. Turbulence measurements in water

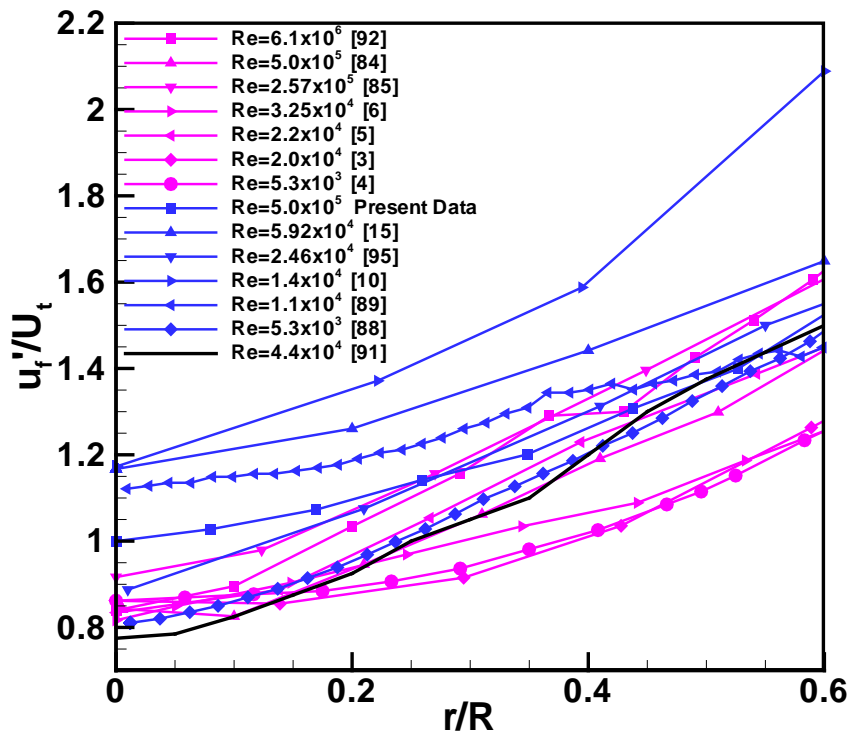


Figure 5-6. Turbulence measurements in air (pink) and water (blue)

## CHAPTER 6 LIQUID-SOLID FLOW

### Pressure Drop

The pressure drop per unit length of a fully developed single-phase fluid in a pipe can be defined as

$$\frac{dP}{dz} = \frac{4\tau_f}{D} = i_f \rho_f g \quad (6-1)$$

where  $i_f$  is the hydraulic gradient in length of fluid per length of pipe and  $\tau_f$  is the wall shear stress. Various methods exist to measure the wall shear stress, but of greater interest here is the ability to infer the wall shear stress, and thus the pressure drop, based on mean flow properties. This is well established in single-phase flows via well known friction factors. In two-phase flows, however, both the measurement of the wall shear stress and the development of correlations to predict the pressure drop, are more challenging. Although there is no established method of predicting two-phase pressure drop, various correlations have been formulated.

Bagnold [23] decomposed the total shear stress of the two-phase mixture into fluid and solid components

$$\tau_m = \tau_f + \tau_s \quad (6-2)$$

And assumed the two-phase pressure can be determined by

$$\frac{dP}{dz_m} = \frac{4\tau_m}{D} = i_m \rho_m g \quad (6-3)$$

where  $\rho_m$  is the volume average density of the two-phase flow. Assuming the fluid is Newtonian, the fluid shear stress is

$$\tau_f = \mu \left( \frac{dU_f}{dr} \right) \Big|_{\text{wall}} \quad (6-4)$$

The shear stress of the solid-phase is more difficult to determine and requires certain assumptions. Based on his experimental results, Bagnold [23] proposed that the solid stress varies based on the flow-regime

$$\tau_s = K_v \mu \lambda_w^{3/2} \left( \frac{dU_s}{dr} \right) \Big|_{\text{wall}} \quad \text{Ba} < 40 \quad (6-5)$$

$$\tau_s = K_i \rho_s d^2 \lambda_w^2 \left( \frac{dU_s}{dr} \right)^2 \Big|_{\text{wall}} \quad \text{Ba} > 450 \quad (6-6)$$

where  $\lambda_w$  is the linear concentration at the wall, defined in equation 1-5. Bagnold [23] determined the viscous and inertial coefficients,  $K_v$  and  $K_i$ , to be 0.013 and 2.2, respectively. However, Bagnold's [23] experiments were conducted in a rotating couette device with a rotating outer cylinder.

## Correlations

### Bartosik

Sumner et al. [98] performed slurry-flow experiments in vertical pipes, utilizing a wide range of particles, varying density, diameter, and concentration, in vertical pipes. They found that slurries of particles less than 0.8 mm in diameter at solids concentrations less than about 20% by volume exhibited no increase in pressure drop over the single-phase fluid. Additional radial solids concentration measurements revealed a very low concentration of particles near the wall, making the two-phase wall shear stress equivalent to that of the single-phase, which helped to explain the lack of increase in the pressure drop. However, Sumner et al. [98] found that at particle diameters greater than 1 mm and at higher solids concentrations, the slurry pressure drop increased over that of the single-phase flow. To investigate these differences, Shook and Bartosik [99] conducted experiments with sand and polystyrene particles

between 1.37 and 3.4 mm in diameter in vertical pipes. They found that the total slurry wall shear stress was equal to that of the single-phase fluid under conditions with particle diameters of approximately 1.5 mm at solids concentration  $\leq 10\%$ .

Shook and Bartosik [99] found no enhancement of the wall shear stress under conditions in the macro-viscous regime, varying particle diameter, concentration, and flow rate. Enhancement occurred in the inertial regime but exhibited a Re dependence. To account for this they modified equation 6-6, replacing  $K_i$  with

$$A = Re_f^{-1.8} \quad (6-7)$$

where  $Re_f$  is the Re based on the mean fluid velocity. Additionally, they simplified equation 6-6 by proposing that the solid velocity gradient be equal to the fluid velocity gradient at the wall. This assumption was partly motivated by the difficulty of obtaining reliable solid velocity measurements at the wall. Furthermore, this assumption eliminates the need to measure the fluid velocity gradient at the wall by relating the two-phase hydraulic gradient to that of the single-phase, and then substituting

$$\left( \frac{dU_f}{dr} \right)_{\text{wall}} = \frac{\tau_f}{\mu} \quad (6-8)$$

Equation 6-7 was further modified Bartosik [100] to the form

$$\frac{A}{D^2} = \frac{8.3018 \times 10^7}{Re_f^{2.317}} \quad (6-9)$$

Bartosik also assumed that the fluid density and slurry density were equal and substituted Bagnold's linear concentration near the wall ( $\lambda_w^2$ ) with that of the bulk slurry ( $\lambda_L^{1.5}$ ). Combining equations 6-1, 6-2, 6-6, 6-8, and 6-9 yields the hydraulic gradient for the slurry obtained by Bartosik [100]

$$i_m = i_f \left( 1 + \frac{8.3018 \times 10^7 \rho_s d^2 \lambda_L^{3/2} \rho_f g D^3 i_f}{4 \mu^2 Re_f^{2.317}} \right) \quad (6-10)$$

where  $i_m$  and  $i_f$  are the hydraulic gradient for the two-phase mixture and single-phase fluid (in units of length of slurry or fluid per length of pipe), respectively. The pressure drop can then be determined with equation 6-3.

Matoušek [101] found that this correlation significantly under predicted the increase in pressure drop caused by sand particles > 0.4 mm in diameter over that of single-phase water. Matoušek [102] concluded that under these conditions the solid-phase affected the wall shear stress directly through collisions with the wall and not simply through an increase density of the two-phase fluid over that of the fluid alone.

### **Littman and Paccione**

Another correlation was developed by Littman and Paccione [103] who derived a solid-phase friction factor,  $f_s$ , based on the assumption that it is a function of the Froude number

$$Fr = \frac{gD}{U_s^2} \quad (6-11)$$

and a turbulence response parameter

$$\frac{t_R}{t_e} = \frac{40}{3C_d} \left( \frac{\rho_s + 0.5\rho_f}{\rho_f} \right) \frac{d}{D} \frac{U_t}{u_r} \quad (6-12)$$

where  $t_R$  and  $t_e$  are the particle relaxation time and the lifetime of the most energetic eddy, respectively.  $U_t$  is the friction velocity and  $C_d$  is the coefficient of drag

$$C_d = \frac{24}{Re_p} \left( 1 + 0.15 Re_p^{0.687} \right) \quad (6-13)$$

and  $U_T$  the terminal velocity

$$U_T = \sqrt{\frac{4}{3C_d} \frac{\rho_s - \rho_f}{\rho_f} g d} \quad (6-14)$$

Their final correlation takes the form

$$\frac{dP}{dz_m} = \frac{dP}{dz_f} \left[ 1 + v \frac{0.295 C_d Re_f^{0.25} \frac{\rho_s}{\rho_s - \rho_f} \frac{D}{d}}{\left(\frac{U_f}{U_T}\right)^2 \left(1 + e^{\frac{t_R}{30t_e}}\right)} \right] \quad (6-15)$$

The two-phase pressure drop is equal to the single-phase multiplied by a correction factor weighted by the concentration of the solid-phase.

### Ferre and Shook

The two previous correlations are based on mean flow properties but still require the hydraulic gradient of the single-phase flow. Ferre and Shook [105] developed a method of predicting the pressure drop in slurry flow, that does not require a measurement of the single-phase pressure drop by utilizing friction factors for both phases.

$$\tau_m = 0.5 U_m^2 (f_f \rho_f + f_s \rho_s) \quad (6-16)$$

where  $f_f$  and  $f_s$  are the fluid and solid friction factors, respectively. The fluid friction factor can be estimated from the Re and surface roughness following the correlation of Churchill [104]

$$f_f = 2 \left[ \left( \frac{8}{Re} \right)^{12} + (A + B)^{-1.5} \right]^{\frac{1}{12}} \quad (6-17)$$

With and A and B defined as

$$A = \left\{ -2.457 \ln \left[ \left( \frac{7}{Re} \right)^{0.9} + 0.27 \left( \frac{k_r}{D} \right) \right] \right\}^{16} \quad (6-18)$$

$$B = \left( \frac{37530}{Re} \right)^{16} \quad (6-19)$$

where  $k_r$  is the surface roughness. The solid-phase friction factor was derived by Ferre and Shook [105] who measured 1.8 and 4.6 mm glass particles in water and ethylene glycol in a 40.9 mm diameter vertical pipe

$$f_s = 0.0428 \left( \frac{dU_m \rho_s}{\mu} \right)^{-0.36} \left( \frac{d}{D} \right)^{0.99} \lambda_L^{1.31} \quad (6-20)$$

Their final correlation can be found by combining equations 6-2, 6-3, and 6-16 through 6-20. They found that the slurry wall friction diverged from that of the single-phase fluid only at solids concentrations above 25% by volume for the 1.8 mm particles while differences were noticeable at the lowest concentration, 9%, for the 4.6 mm particles.

## Results

### Experimental

The hydraulic gradient as a function of mean fluid velocity for each solids concentration and particle diameter can be found in Figures 6-1 through 6-3. Each figure displays the experimental results as well as the pressure predicted by the correlations of Ferre and Shook [105], Bartosik [100], and Littman and Paccione [103]. The error bars on the experimental data represent a 95% confidence interval. The experimental results and correlations are all very similar at the lower two  $Re$  for all concentrations, except for the 0.5 mm particles where the correlation of Littman and Paccione [103] significantly over predicts the pressure. This over prediction is the result of very small  $Re_p$  resulting from a very small slip velocity.

At the highest velocity the experimental results for the 1.0 mm particles at 0.7% and 1.7% solids are significantly lower than predicted. This was true to a lesser extent

for the 0.5 mm particles under the same conditions, though the prediction was within a 95% confidence. In light of this the pressure drop measurements for the 1.0 mm particles at the highest Re were repeated, with very similar results. The radial solids concentration profiles of Alajbegović et al. [16] show the solid-phase moving toward the pipe center with increasing Re at solids concentrations of approximately 2.3% by volume. As the particles move toward the pipe center there is a decrease in the solids contribution to the wall friction. However, the same results should then be expected for the 1.5 mm particles, but were not observed. Why the two-phase pressure is less than that of the clear fluid at the highest Re is not certain, but could be an example of drag reduction.

Drag reduction is a well documented phenomenon in solid-liquid systems when the solid-phase is high aspect ratio fibers or with the addition of polymers or solvents. However, drag reduction has also been observed in water-solid flows with more spherical particles. Sifferman and Greenkorn [106] found drag reduction in sand-water flows of about 1% sand by volume, average diameter of 350  $\mu\text{m}$ , at Re from  $5 \times 10^4$  to  $4 \times 10^5$ . Zandi [107] found drag reduction in solid-liquid flows over a range of solid concentrations of clay, coal, fly ash, and activated charcoal slurries—with a maximum of 57% reduction for clay approximately 500  $\mu\text{m}$  in diameter at  $\text{Re} = 1.0 \times 10^5$ . Many other examples of drag-reduction at specific Re have also been observed (Radin et al. [108]).

Drag reduction has also been observed for smooth spherical particles in gas-solid systems. In these cases the particle diameter is typically much smaller than the particles presently tested. Radin et al. [108] tested a range of spherical particles in water with diameters up to 420  $\mu\text{m}$ , at solids concentrations up to about 1% by volume

and  $Re$  up to  $3.94 \times 10^5$ , but found no drag reduction. Where the current experimental conditions overlap with the experiments of Radin et al. [108], namely at the lower  $Re$ , no drag reduction was observed. However, no data exists for liquid-solid flow of spherical particles at  $Re \geq 5.0 \times 10^5$ . Also noteworthy is that Sifferman and Greenkorn [106] found certain oil-water-sand mixtures to be drag enhancing at low  $Re$  and drag reducing at high  $Re$ , clearly showing a  $Re$  dependence. It is consistent with theory that the apparent reduction occurred at lower solids concentrations and at higher  $Re$ . Consequently, the possibility of drag reduction under these conditions exists and further investigation is needed to quantify the phenomena.

### **Correlations**

No correlation accurately predicts all the experimental results. The correlation of Ferre and Shook [105] consistently over predicts  $dP/dz$  for the 1.0 mm particles. However, for the 1.5 mm particles the correlation of Bartosik [100], with its  $D^3$  term, over predicts the pressure drop at the lower two  $Re$ . Overall, the correlation of Littman and Paccione [103] does the best job of predicting the pressure drop over the range of conditions. The correlations of Littman and Paccione [103] and Bartosik [100] utilize the experimental single-phase hydraulic gradient while that of Ferre and Shook [105] does not. This helps explain while the values predicted by Ferre and Shook [105] show greater deviation than the other two correlations.

The large error bars can be misleading. As explained in the error analysis section of Chapter 2, the dilute nature of the two-phase flow suggests it should be similar to single-phase flow—as the correlations of Littman and Paccione [103] and Bartosik [100] clearly show. Single-phase pressure drop is well understood and can be accurately predicted. Our experimental single-phase measurements were very similar to

established values. Additionally, the single-phase friction velocity determined via the pressure profile was in good agreement with that determined via LDV measurements of the near wall velocity gradient.

### **Velocity Measurements**

A total of 27 mean and fluctuating velocity profiles were completed. Three particles sizes, 0.5 mm, 1.0 mm, and 1.5 mm; at three flow rates,  $Re = 2.0 \times 10^5$ ,  $3.35 \times 10^5$ , and  $5.0 \times 10^5$ ; and three solids concentrations, 0.7%, 1.7%, and 3% solids by volume. Only the fluid mean and fluctuating velocities were obtained for the slurry composed of 1.5 mm particles. Additionally, measurements of the 0.5 mm solids and the fluid in their presence were limited to  $r/R \geq 0.45$ . In all cases the raw velocity is normalized by the mean fluid centerline velocity,  $U_{fc}$ . In the case of the 0.5 mm particles at 3% solids, where the measurements were limited to  $r/R \geq 0.45$ , the mean centerline fluid in the presence of the 0.5 mm particles is estimated by assuming the ratio of fluid centerline velocity to fluid velocity at  $r/R = 0.46$  for the 0.5 mm particles is equal to that of the 1.0 mm particles, at each respective  $Re$ .

Table 6-1 outlines these conditions and gives Bagnold, Stokes, and particle Reynolds numbers for all conditions. Determination of  $Re_p$  requires a mean solid velocity and is consequently not calculated for the 1.5 mm particles and the 0.5 mm particles at 3% solids. Figure 6-4 presents the data in Table 6-1 and shows that the Bagnold and Stokes numbers increase continuously with no significant overlap as conditions change for the 0.5 mm and 1.0 mm particles; first for increasing solids concentration for a given  $Re$  and particle diameter, then by increasing  $Re$ , and lastly by particle diameter. The Bagnold and Stokes numbers of the 1.5 mm particles at the lowest  $Re$  overlap with those of the 1.0 mm particles at the highest  $Re$ . Particle

Reynolds numbers experience the greatest change with changing conditions (specifically particle diameter) and are consequently plotted on a log scale.

### **Fully Developed Flow and Reproducibility of Data**

Measurements of the solid and liquid velocity over two radii, 90° apart, and at two axial locations, separated by 6 pipe diameters were made to verify that the slurry was fully developed. The solid-phase was composed of 0.5 mm particles at a concentration of 0.7% by volume and at  $Re = 2.0 \times 10^5$ . The results can be found in Figure 6-5.

Additionally, the pressure at six vertical locations prior to the test section at these same conditions can be found in Figure 6-6. A linear regression through these six points is how the hydraulic gradient was determined—for this specific case  $R^2=0.9999$ . The profile is clearly linear, another indication that the flow is fully developed.

Additionally, the reproducibility of the measurements was examined. The measurements of the velocity of the 1.0 mm particles at 0.7% solids and  $Re = 2.0 \times 10^5$  were repeated three times. The results can be found in Figure 6-7A. Run 1 was conducted almost a year prior to runs 2 and 3. Runs 2 and 3 were completed hours apart, though the pump and LDV were shutdown between measurements. The figure depicts the high degree of reproducibility of the measurements. Figure 6-7B shows the average value with the error bars representing  $\pm$  one standard deviation. The 3 runs, along with all other measurements, were conducted at the top of the pipe over the north radius.

The small amount of variation in the velocity measurements in Figures 6-5 and 6-7 are less than the effects observed by manipulating the experimental variables. Consequently, changes in the mean and fluctuating velocity profiles observed when

adjusting particles size, solids concentration, and Re can be confidently regarded as the result of that adjustment.

### **Mean Velocity**

Figures 6-8 through 6-10 show the effects of Re and solids loading on the mean fluid velocity for all particle sizes. The maximum velocity of both phases was always found at the pipe center. Examining the shape of the profiles shows that the mean fluid velocity is very similar in shape to that of the single-phase fluid for all flow conditions. The profiles have the flat shape characteristic of turbulent flow. This shape does not change significantly with changes in Re, Ba, or St.

The mean solid velocity profiles are presented in Figures 6-11 through 6-13. The most obvious difference is the increased slip velocity, the velocity difference between two phases, between the 0.5 mm and 1.0 mm particles. As expected, the larger particles have a larger slip. The slip between the fluid and 0.5 mm particles is very small; no more than 1% in all cases with no significant trends as conditions were changed. Additionally, as evident by the small slip, the profile of the 0.5 mm particles is also very similar to that of the single-phase fluid. Tsuji et al. [5] also found that 200  $\mu\text{m}$  particles exhibited a curved profile while 500  $\mu\text{m}$  were flat. However, Tsuji's 200  $\mu\text{m}$  particles were still in the grain-inertia flow regime, according to the Bagnold number.

The 1.0 mm particles exhibit a flatter, more linear profile across the pipe radius. The degree of flatness increases slightly with increasing solids loading. In some cases, like in Figure 6-13A the solid velocity exceeds that of the fluid near the wall. The negative slip is the result of solid slip near the wall, while the fluid does not slip. No prominent trends regarding the negative slip near the wall were found. The 1.0 mm particles exhibit an increase in slip as solids concentration increases, a result opposite

that of Hardalupas [20]. Interestingly, there is a decrease in slip from  $Re = 2.0 \times 10^5$  to  $Re = 3.35 \times 10^5$  and then an increase again at  $Re = 5.0 \times 10^5$ . Overall, the slip at the highest  $Re$  is greater than at the lowest  $Re$  which is in agreement with the results of Jones [8]. However, this is the opposite of the result of Chemloul and Benrabah [29] who found a decrease in slip with increasing  $Re$  with 0.5 mm and 1.0 mm glass particles at  $Re$  between  $9.4 \times 10^3$  and  $2.48 \times 10^4$ . Thus the lack of a trend regarding the impact of  $Re$  on particle slip in the present data is consistent with the various findings in the literature. Increasing the solids concentration has a greater effect than increasing the  $Re$  on the slip velocity in the range of conditions tested. However, the solids concentration has a significantly smaller influence on  $Ba$ ,  $St$ , and  $Re_p$ , than  $Re$  or particle diameter, indicating that these parameters fail to capture the flow behavior under conditions of increasing solids.

## **Fluctuating Velocity**

### **Effect of $Re$**

Figures showing the fluctuating velocity of the liquid in the presence of each particle size are presented in Figures 6-14 through 6-16. The fluctuating velocity of the 0.5 mm and 1.0 mm solid-phases' are shown in Figures 6-17 through 6-19. Generally, the fluid fluctuations increase with increasing particle size, especially near the wall. The effect of particle size on fluid fluctuations diminishes as the center of the pipe is approached. Increasing fluid fluctuations with increasing particle size is characteristic of collision-dominated flow and opposite that of viscous-dominated flow. The fluid fluctuations decrease with increasing  $Re$  across the pipe, which is characteristic of viscous-dominated flow and opposite that of collision-dominated flow. The fluid fluctuating velocity becomes more flat at  $r/R < 0.5$  as  $Re$  increases, such that at  $Re =$

$5.0 \times 10^5$  there is very little change in this region of the pipe. The presence of the solid-phase damps the fluid turbulence near the pipe center at the lower two Re and slightly enhances it at the highest Re, for all particles sizes.

The solid fluctuating velocity of the 1.0 mm particles is significantly greater than that of the 0.5 mm particles for all conditions, a trend found in both viscous-dominated and collision-dominated flow. In comparison with the single-phase fluid, the 1.0 mm particle fluctuating velocity is always greater, while that of the 0.5 mm particles is less than or equal, except very near the wall. At each respective Re, the solids fluctuations for the 1.0 mm particles are greater than those of the fluid in their presence, except very near the wall where they become similar. Conversely, the solids fluctuations for the 0.5 mm particles are less than those of the fluid in their presence. The difference in turbulence between the two phases decreases with increasing Re.

The solid-phase turbulence profile also becomes increasingly flat with increasing Re at the lower two solids concentrations for both particles sizes. For example, at 1.7% solids the turbulence of both phases changes very little at  $Re = 5.0 \times 10^5$  at  $r/R < 0.5$ . At 3% solids, increasing the Re increases the turbulence of the solid-phases in the middle of the radius. This has the effect of decreasing the flatness of the profile. It is reasonable to expect a flat profile to develop at  $r/R < 0.5$  with increasing Re for the 0.5 mm particles, as it did at 1.7% solids.

Similar to the decrease in slip at  $Re = 3.35 \times 10^5$ , the magnitude of the solid turbulence at the pipe center decreases as the Re is increased from  $2.0 \times 10^5$  to  $3.35 \times 10^5$ , and then increases again at  $Re = 5.0 \times 10^5$ . The magnitude at the two Re extremes are similar. This is true for both particles sizes at 0.7% and 1.7% solids. The

centerline solid turbulence of the 1.0 mm particles at 3% solids at all three Re are similar.

These findings could be explained by a reduction in turbulence with increasing Re by a redistribution of the solids more evenly across the pipe. However, at the highest Re, there is a significant increase in  $Re_p$ , from  $< 200$  to  $> 300$  for all loadings. This increase in  $Re_p$  is indicative of an increase in slip. The increase in slip suggests a significant increase in vortex shedding that enhances both fluid and solid fluctuations.

### **Effect of solids concentration**

The effects of altering the solids concentration on the fluid turbulence are most prominent at the lowest Re. At the two higher Re, there is little change in the fluid turbulence across the pipe. There are two main exceptions to this, both at  $Re = 5.0 \times 10^5$ ; the fluid in the presence of the 0.5 mm particles increases and becomes flat as solids concentration increases and near the wall there is an increase in fluid turbulence in the presence of the 1.0 and 1.5 mm particles with increasing solids concentration.

At  $Re = 2.0 \times 10^5$  the fluid fluctuations near the wall decrease with increasing solids concentration for the 0.5 mm and 1.0 mm particles. This decrease includes a change from turbulence enhancement to turbulence damping with respect to the single-phase fluid. The fluid in the presence of the 1.5 mm particles shows an increase in turbulence near the wall at the highest loading. The fluid turbulence near the center of the pipe increases and becomes more flat with increasing solids content at the lowest Re, a trend consistent with collision-dominated flow and opposite that of viscous-dominated flow. This increase at the pipe center again includes a change from minor turbulence damping to minor enhancement. At  $Re = 3.35 \times 10^5$  the two-phase fluid turbulence is very similar to that of the single-phase turbulence. Minor enhancement occurs at the

wall and damping near the pipe center. At  $Re = 5.0 \times 10^5$  the presence of the solid-phase enhances the turbulence at the wall and center.

The effects of changing the solids concentration on the solid turbulence are most evident at the lowest  $Re$ ,  $2.0 \times 10^5$ . At this  $Re$  the solid fluctuations of the 1.0 mm particles decrease with increasing solids concentration, except near the pipe center, where it remains relatively constant. At the higher two  $Re$  the decrease in solid turbulence is only evident near the wall. The solid fluctuations near the wall for the 0.5 mm particles decrease with increasing solids concentration and remain largely unchanged away from the wall. The only increase in solid fluctuations with increasing solids concentration occurs at 3% solids and  $Re = 5.0 \times 10^5$ . The increase in solid turbulence under these conditions is indicative of a collision-dominated flow, which makes sense considering these conditions represent the highest Bagnold number at which solid velocity data was gained.

The solid turbulence profile becomes more flat with increasing solids concentration for the 1.0 mm particles. At the pipe center the solid turbulence does not change significantly with solids loading. This constant level, when combined with an overall decrease in turbulence throughout the middle of the radius results in the profile becoming more flat with increasing solids content at each  $Re$ .

The solid turbulence profiles at 0.7% and 1.7% are similar in shape. With the 1.0 mm particles the solid fluctuations are similar in magnitude to that of the fluid near the center of the pipe. Otherwise, the solid fluctuations are greater than the fluid fluctuations. In the case of the 0.5 mm particles, increasing the solids concentration decreases the difference in turbulence between the two phases.

To summarize, the results show trends characteristic of both collision-dominated and viscous-dominated flow, clearly showing the flow is in a transitional regime. For both particle sizes, the effects of changing the  $Re$  are greater than the effects of changing the solids loading, as expected, because increasing the  $Re$  results in a greater change in Stokes and Bagnold numbers than increasing the solids loading. The most significant changes occur at the highest  $Re$  and solids concentration for the 1.0 mm particles. This is expected, because under these conditions the Bagnold and Stokes numbers are largest. The similarity in the fluid and solid profiles for the 0.5 mm particles, at both the mean and fluctuating level are also as expected. The Stokes numbers for the 0.5 mm particles range from 1.3 to 3.2, indicating a solid-phase that is not totally independent of the fluid. The Bagnold numbers range from 25 to 90, indicative of viscous-dominated flow. The 1.0 mm particles experience a greater change in turbulence profile over the solids loadings and Reynold's numbers tested, which is again expected as they cover the greatest range of Bagnold numbers, from 94 to 299.

Gore and Crowe [34] stated that when  $d/0.2R > 0.1$  fluid turbulence enhancement should be expected. Based on this ratio, the 0.5 mm particles should damp turbulence while the 1.0 and 1.5 mm particles should enhance the fluid turbulence. The results show that this trend is generally true—the larger particles have a greater tendency to enhance turbulence—but not a sufficient predictor. Hetsroni [35] suggested that the  $Re_p$  was a better predictor and argued that  $Re_p > 400$  will result in turbulence enhancement via vortex shedding and wake formation. Sheen et al. [6] found this to be

true at  $Re_p > 100$ . The present data suggest that turbulence enhancement via wake formation occurred at  $Re_p > 300$ .

However, the results also show that predicting changes in the fluid turbulence is more complicated than either of these two predictors. For example, near the wall, where the slip between the two phases is generally small, producing a small  $Re_p$ , significant turbulence enhancement is found, even in the presence of the 0.5 mm particles. Likewise, increased slip (larger  $Re_p$ ) does not necessarily produce greater turbulence enhancement. At the pipe center the 1.0 mm particles at 1.7% solids and  $Re = 2.0 \times 10^5$  and  $5.0 \times 10^5$  have similar slip (Figure 6-12A,C), but the fluid turbulence at the lower  $Re$  is slightly damped while at the higher  $Re$  it is slightly enhanced (Figure 6-15A,C). Finally, the results also show a clear  $Re$  dependence, in agreement with Hadinoto et al. [9].

### **Error Analysis**

Based on equation (2-21) there is negligible error in the mean velocity measurements. For example, with turbulence intensity of 0.1 and an ensemble size of 500 measurements at 95% confidence the error is 0.88%. Based on equation (2-22) the error in the fluctuating velocity measurements depends only on the number of data points. For example, at 95% confidence 500 data points results in an uncertainty of  $\pm 6.2\%$ . Figure 6-20 shows the fluid fluctuating velocity with error bars based on equation (2-21) for 1 mm particles at  $r/R = 0.82$  for  $Re = 5.0 \times 10^5$  and 3% solids. Furthermore, Figure 6-21 depicts the evolution of the standard deviation with data count, showing that the standard deviation is flat and no significant changes would be expected with additional hits. There were generally several thousand measurements for each solid velocity, making their error very small, on the order of the size of the data point. To

further illustrate this, Figure 6-22 shows the evolution of the standard deviation for 0.5 mm particles at  $r/R = 0.91$  for 0.7% solids and  $Re = 3.35 \times 10^5$ . Under these conditions more than  $2.0 \times 10^4$  velocity measurements were recorded. The figure shows the small changes in  $u_s'/U_{fc}$  after various data counts.

Another method of quantifying error in the fluctuating velocity measurements is to calculate the standard deviation of the fluctuating velocity after a certain minimum number of measurements are recorded—in this case 250. Figure 6-23 represents the same conditions as Figure 6-20, except the error bars denote  $\pm$  one standard deviation of  $u_f'/U_{fc}$  determined from velocity measurements 251 and above. In almost all cases the error bars are smaller than the data markers.

### **Conclusion**

Measurements of the mean and fluctuating velocity of a turbulent liquid-solid flow composed of 0.5, 1.0, or 1.5 mm glass spheres in water at solids concentrations of 0.7%, 1.7%, and 3% and  $Re$  of  $2.0 \times 10^5$ ,  $3.35 \times 10^5$ , and  $5.0 \times 10^5$  were made with LDV/PDPA. Additionally, the hydraulic gradient as a function of  $Re$  was measured for each particle size and solids concentration. The data constitute a unique contribution to the field of multiphase flow, as the range of conditions measured span the transition from a viscous-dominated to an inertia-dominated flow.

The major results are:

Drag reduction for the 1.0 mm particles at the highest  $Re$  occurs while the other pressure gradient for the other two-phase conditions is similar to each respective single-phase flow.

For all particle sizes,  $Re$ , and solids concentrations the mean fluid velocity is very similar in shape to that of the single-phase fluid.

The slip between the fluid and 0.5 mm particles is very small while the 1.0 mm particles exhibit an increase in slip as solids concentration increases.

Trends characteristic of both collision-dominant and viscous-dominated flow are evident, clearly showing the flow is in a transitional regime.

Generally, the 0.5 mm particles damp the fluid turbulence while the 1.0 mm and 1.5 mm particles are either neutral or enhance the turbulence.

The solid turbulence of the 1.5 mm particles exceeds that of the fluid in their presence, while the solid-phase turbulence of the 0.5 mm particles is less than the fluid in their presence.

The turbulence of both phases becomes increasingly flat near the center of the pipe with increasing  $Re$  and solids loading. This is in agreement with the flat profiles of both fluid and solid turbulence in inertia-dominated gas-solid flows.

There is a decrease in turbulence with increasing  $Re$  until vortex shedding and wake formation increases turbulence at  $Re_p > 300$ .

The effects of changing the  $Re$  are greater than the effects of changing the solids loading.

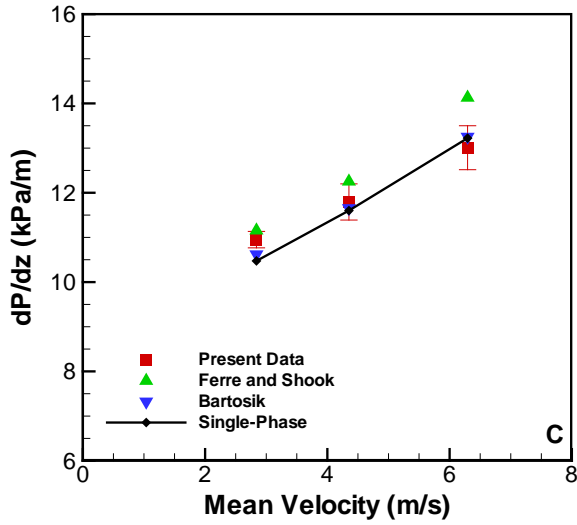
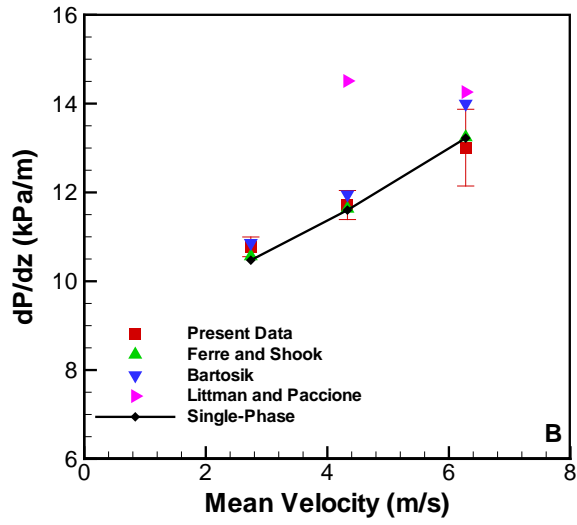
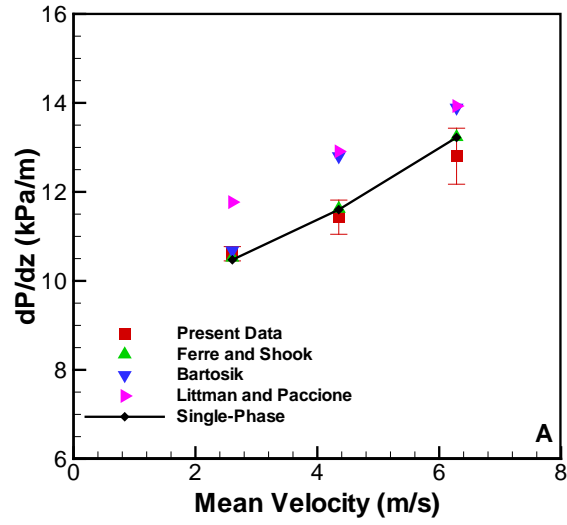


Figure 6-1. Pressure drop with 0.5 mm particles. A) 0.7% solids, B) 1.7% solids and C) 3% Solids

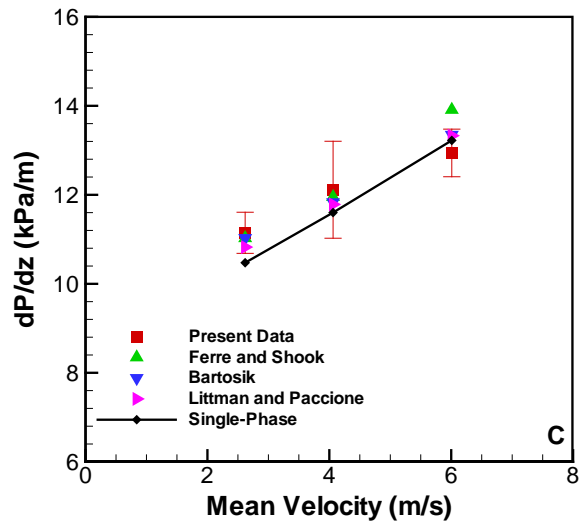
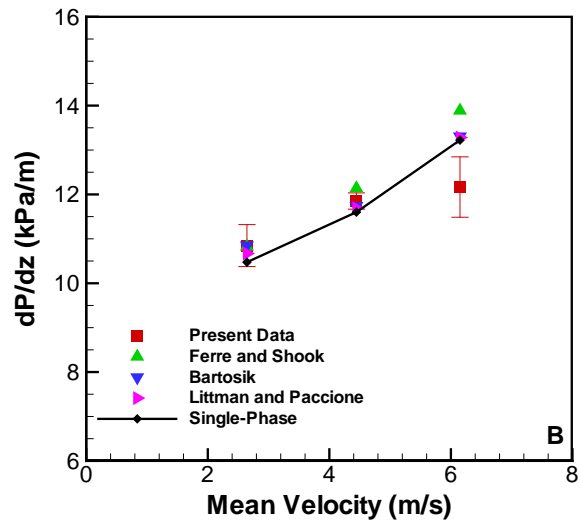
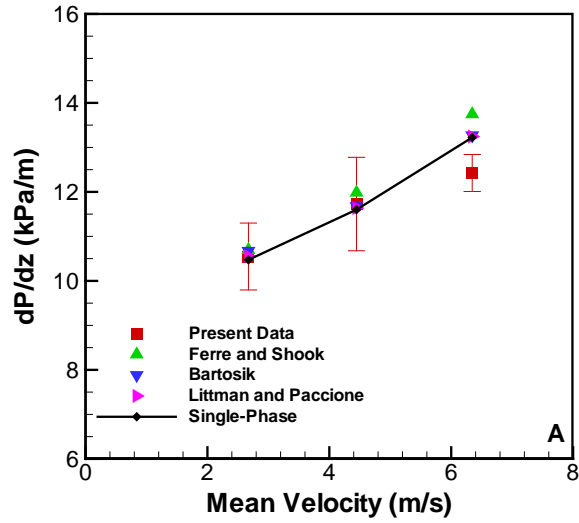


Figure 6-2. Pressure drop with 1.0 mm particles. A) 0.7% solids, B) 1.7% solids and C) 3% Solids

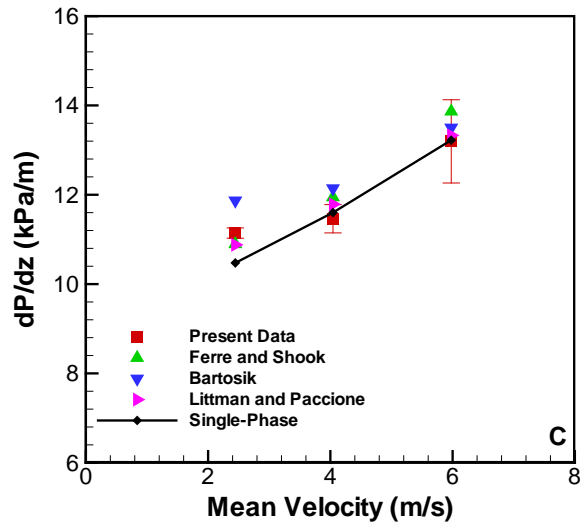
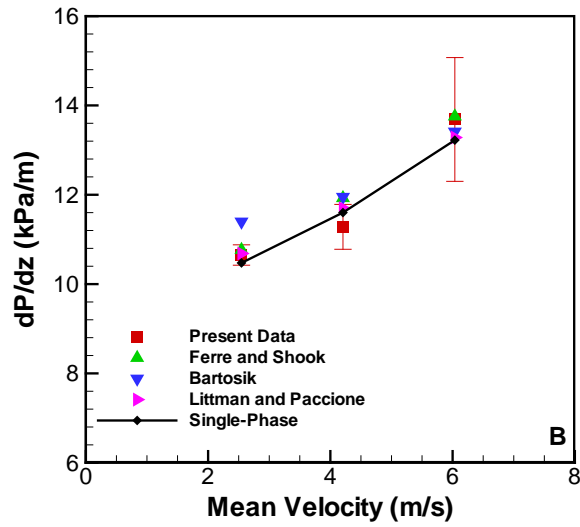
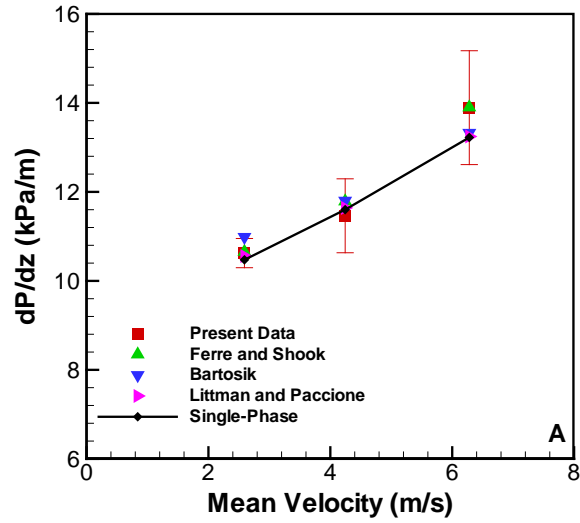


Figure 6-3. Pressure drop with 1.5 mm particles. A) 0.7% solids, B) 1.7% solids and C) 3% Solids

Table 6-1. Experimental parameters in dimensionless numbers

Re	% Solids	$d_p$ (mm)	Ba	St	$Re_p$
$2.0 \times 10^5$	0.7	0.5	25	1.3	2.6
$2.0 \times 10^5$	1.7	0.5	31	1.3	0.3
$2.0 \times 10^5$	3	0.5	38	1.4	
$3.35 \times 10^5$	0.7	0.5	42	2.2	6.3
$3.35 \times 10^5$	1.7	0.5	49	2.1	3.4
$3.35 \times 10^5$	3	0.5	58	2.1	
$5.0 \times 10^5$	0.7	0.5	62	3.2	6.7
$5.0 \times 10^5$	1.7	0.5	77	3.3	14.0
$5.0 \times 10^5$	3	0.5	87	3.2	

Re	% Solids	$d_p$ (mm)	Ba	St	$Re_p$
$2.0 \times 10^5$	0.7	1.0	97	5.6	21
$2.0 \times 10^5$	1.7	1.0	122	5.7	155
$2.0 \times 10^5$	3	1.0	139	5.5	90
$3.35 \times 10^5$	0.7	1.0	163	9.4	87
$3.35 \times 10^5$	1.7	1.0	205	9.4	124
$3.35 \times 10^5$	3	1.0	221	9.3	175
$5.0 \times 10^5$	0.7	1.0	259	15.4	306
$5.0 \times 10^5$	1.7	1.0	303	14.5	334
$5.0 \times 10^5$	3	1.0	341	14.2	596

Re	% Solids	$d_p$ (mm)	Ba	St	$Re_p$
$2.0 \times 10^5$	0.7	1.5	230	13.3	
$2.0 \times 10^5$	1.7	1.5	276	13.1	
$2.0 \times 10^5$	3	1.5	305	12.6	
$3.35 \times 10^5$	0.7	1.5	385	22.5	
$3.35 \times 10^5$	1.7	1.5	461	21.9	
$3.35 \times 10^5$	3	1.5	516	21.5	
$5.0 \times 10^5$	0.7	1.5	570	33.3	
$5.0 \times 10^5$	1.7	1.5	677	32.5	
$5.0 \times 10^5$	3	1.5	763	31.7	

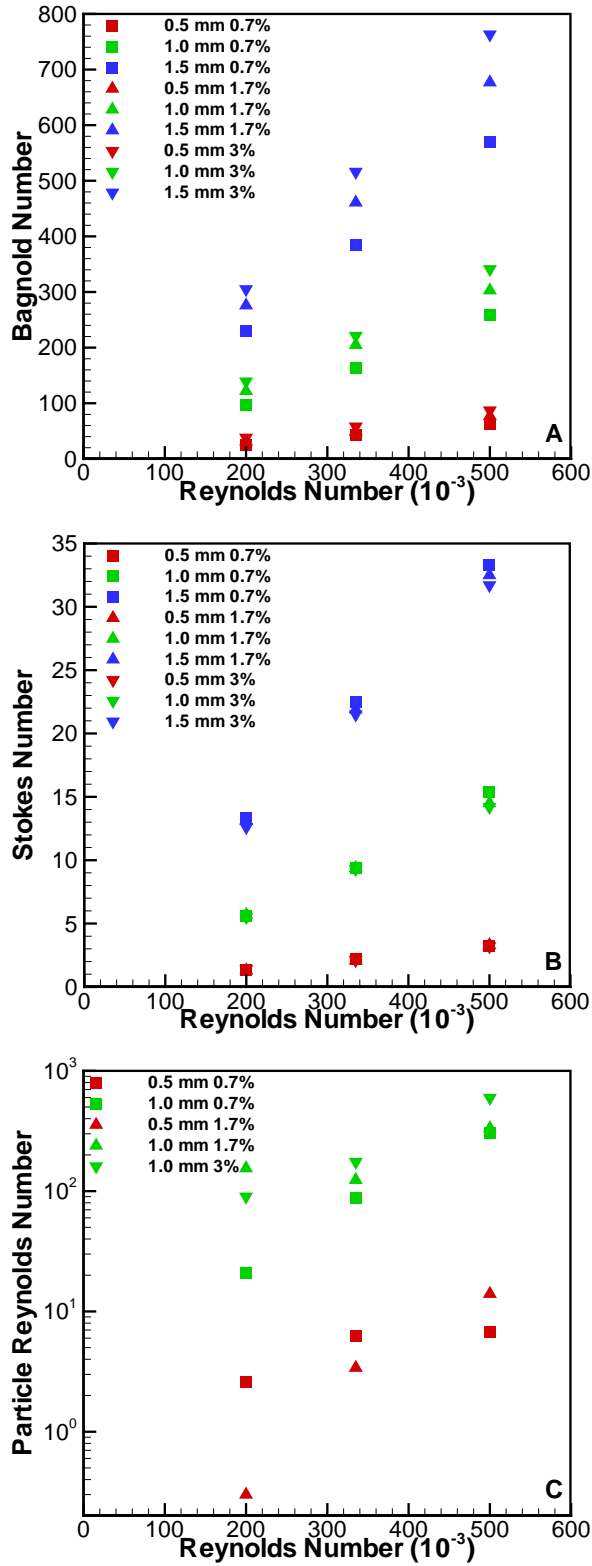


Figure 6-4. Dimensionless parameters of experiments. A) Bagnold number, B) Stokes number and C) particle Reynolds Number

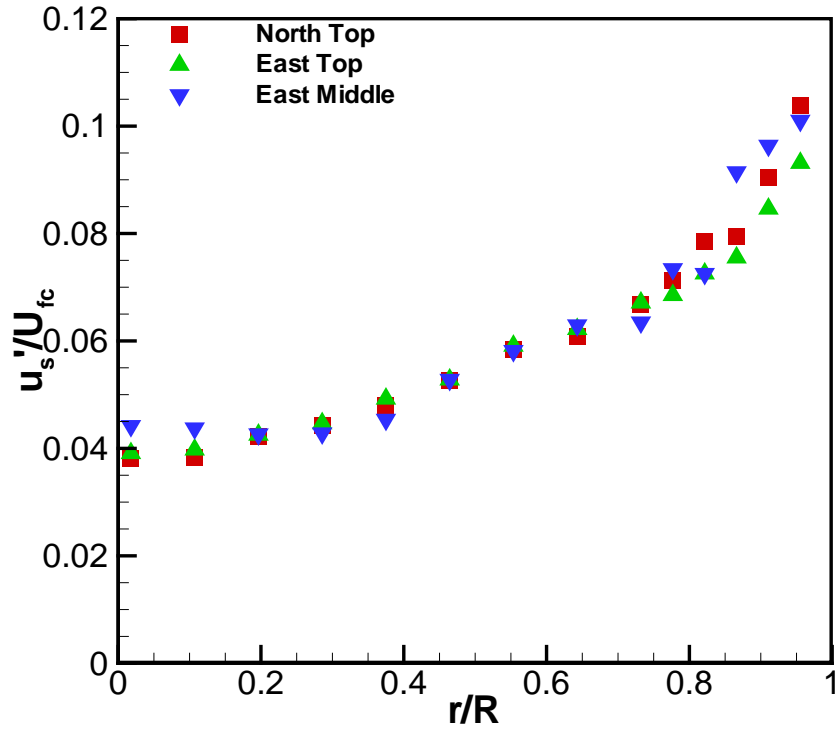


Figure 6-5. Fully developed flow, solid fluctuating velocity at two radii and two developmental lengths for 0.5 mm particles at 0.7% solids and  $Re = 2.0 \times 10^5$

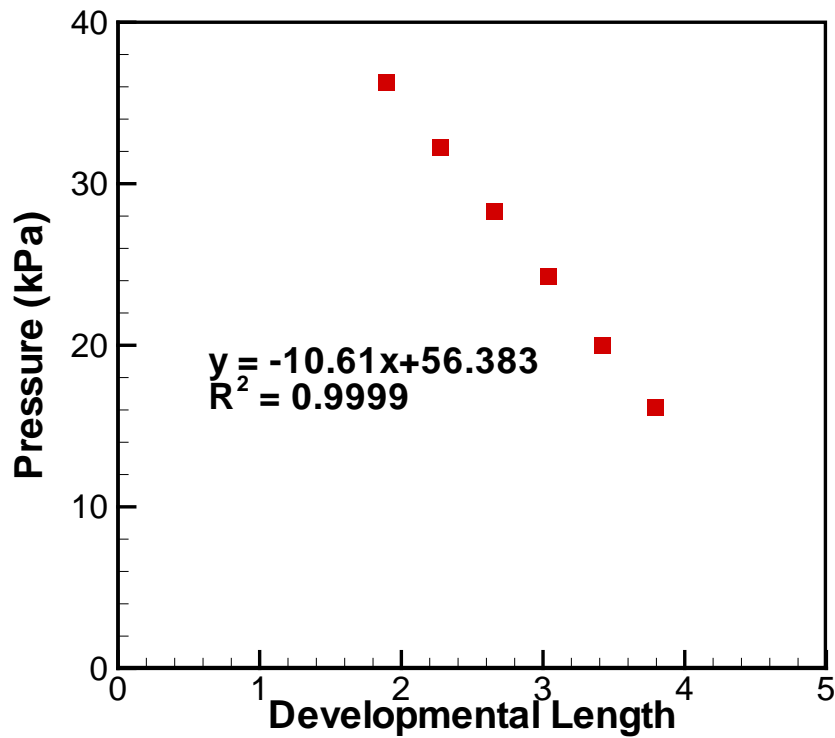


Figure 6-6. Linear pressure profile for 0.5 mm particles at 0.7% solids and  $Re = 2.0 \times 10^5$

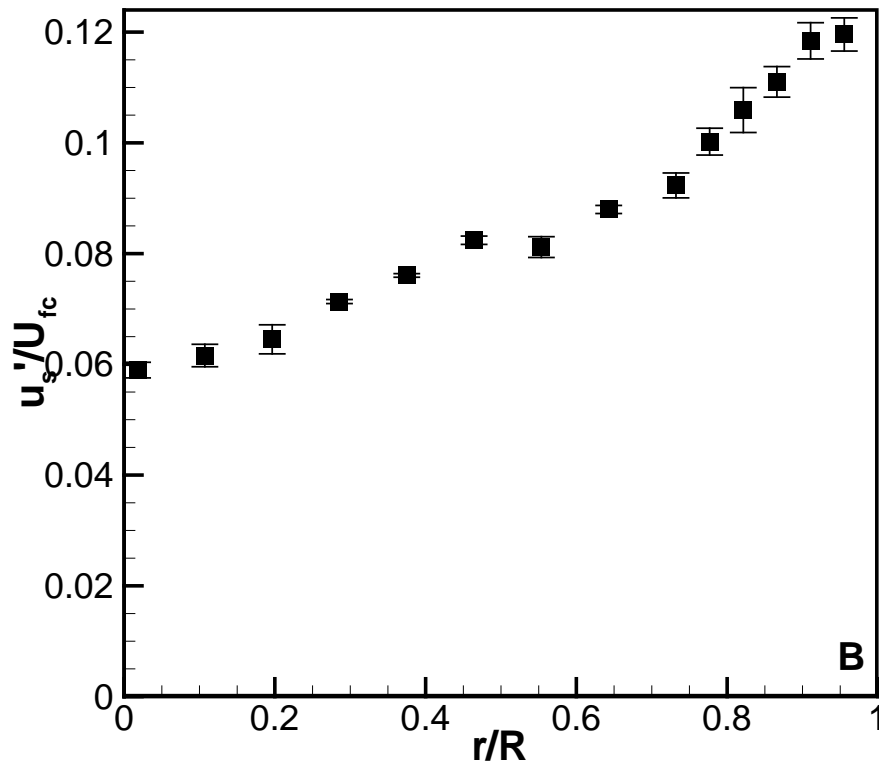
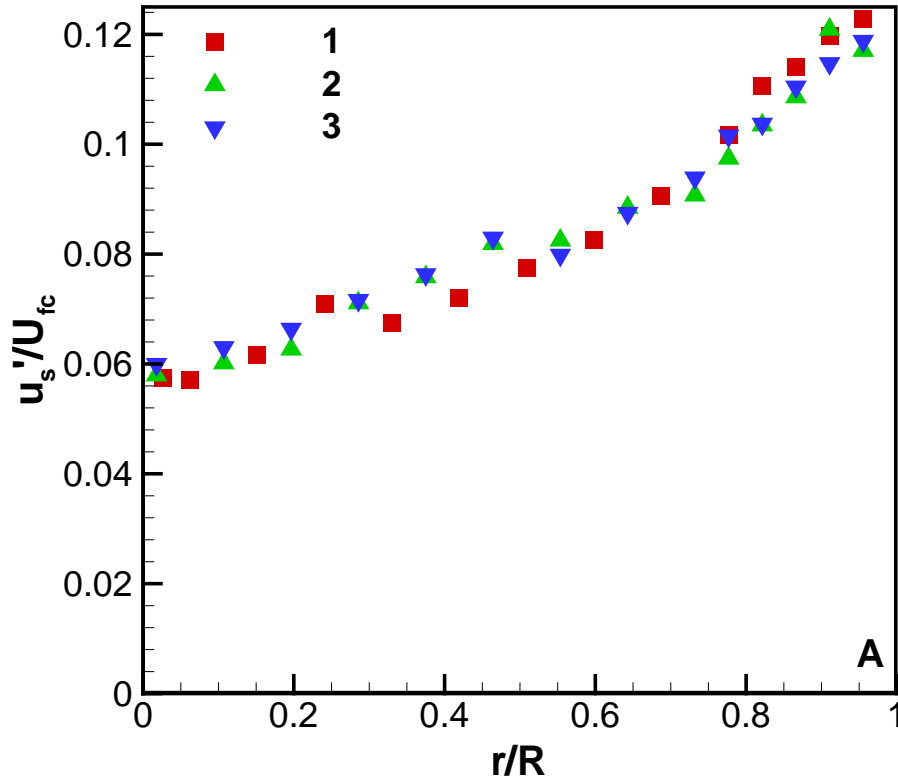


Figure 6-7. Reproducibility of measurements; solid fluctuating velocity of 1.0 mm particles at 0.7% solids and  $Re = 2.0 \times 10^5$ . A) individual measurements B) average and standard deviation

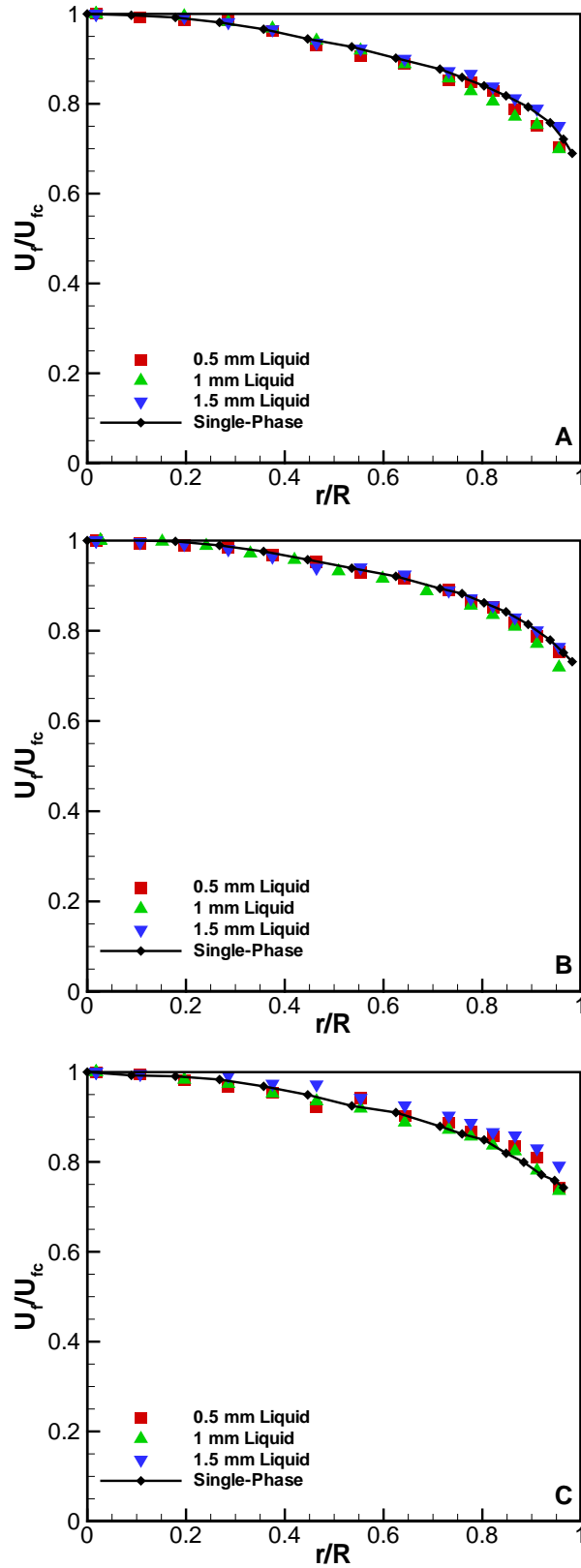


Figure 6-8. Fluid mean velocity at 0.7% solids. A)  $Re = 2.0 \times 10^5$ , B)  $Re = 3.35 \times 10^5$  and C)  $Re = 5.0 \times 10^5$

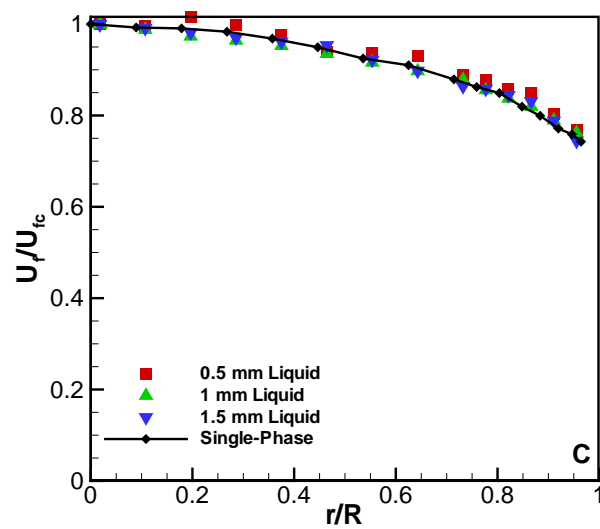
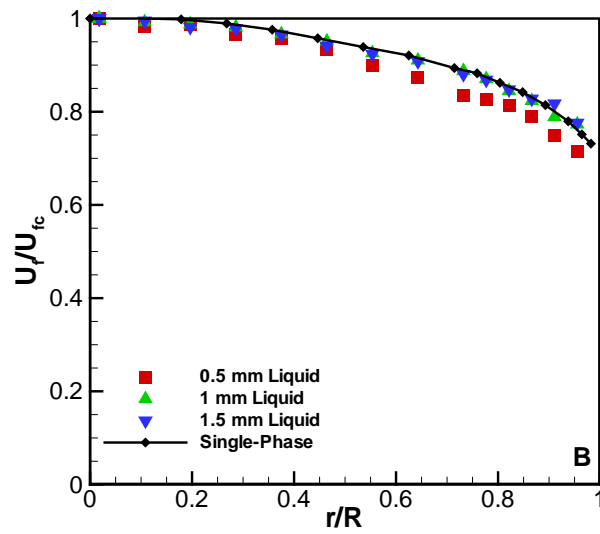
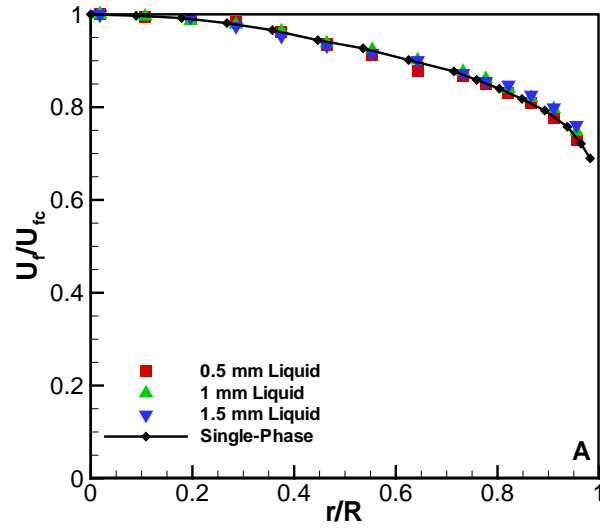


Figure 6-9. Fluid mean velocity at 1.7% solids. A)  $Re = 2.0 \times 10^5$ , B)  $Re = 3.35 \times 10^5$  and C)  $Re = 5.0 \times 10^5$

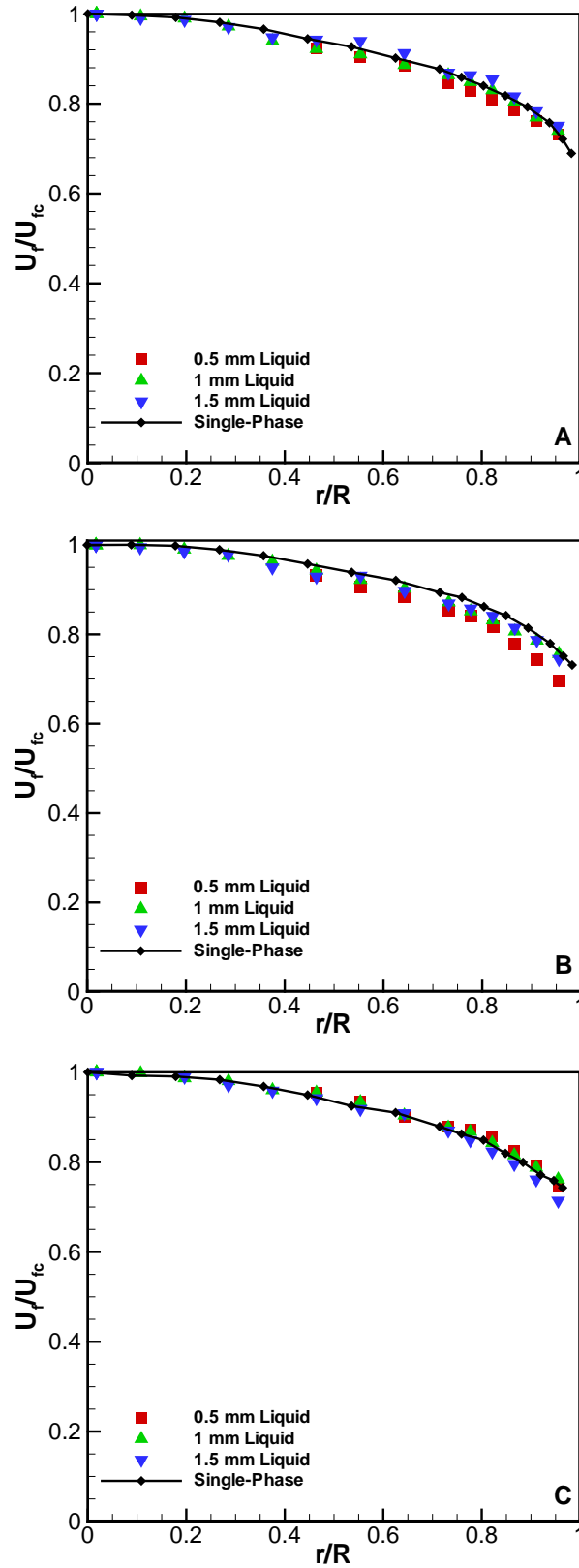


Figure 6-10. Fluid mean velocity at 3% solids. A)  $Re = 2.0 \times 10^5$ , B)  $Re = 3.35 \times 10^5$  and C)  $Re = 5.0 \times 10^5$

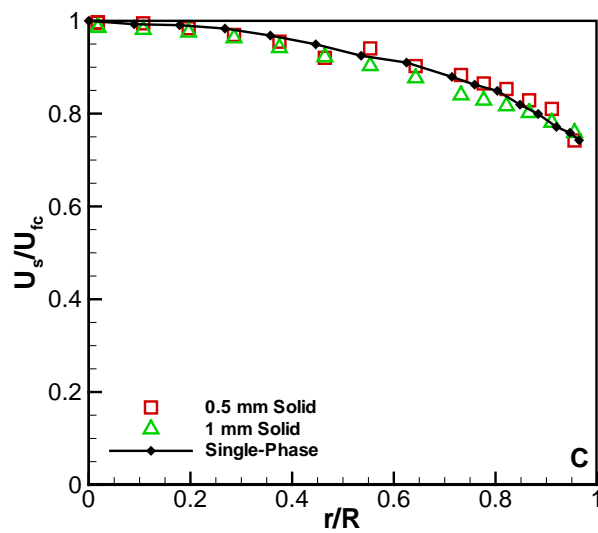
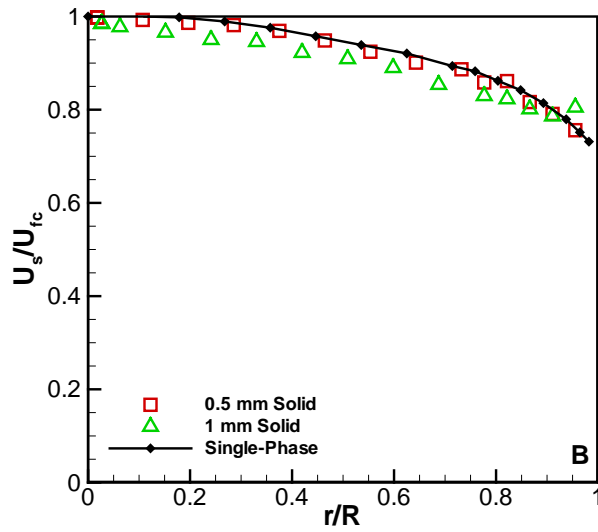
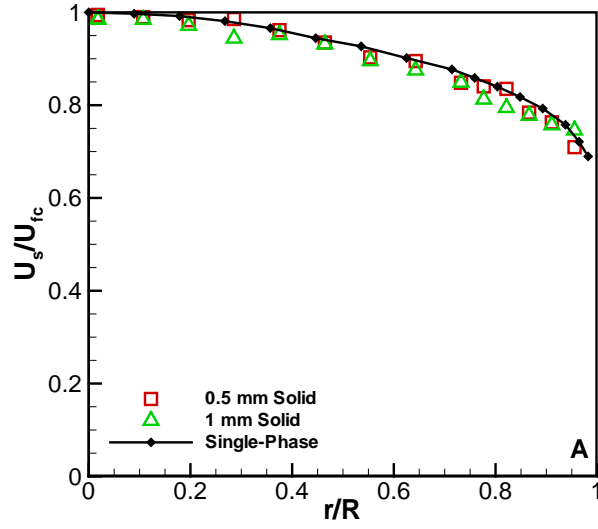


Figure 6-11. Solid mean velocity at 0.7% solids. A)  $Re = 2.0 \times 10^5$ , B)  $Re = 3.35 \times 10^5$  and C)  $Re = 5.0 \times 10^5$

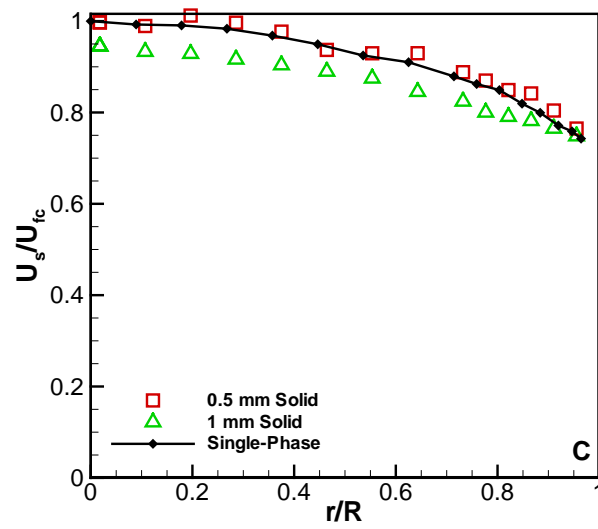
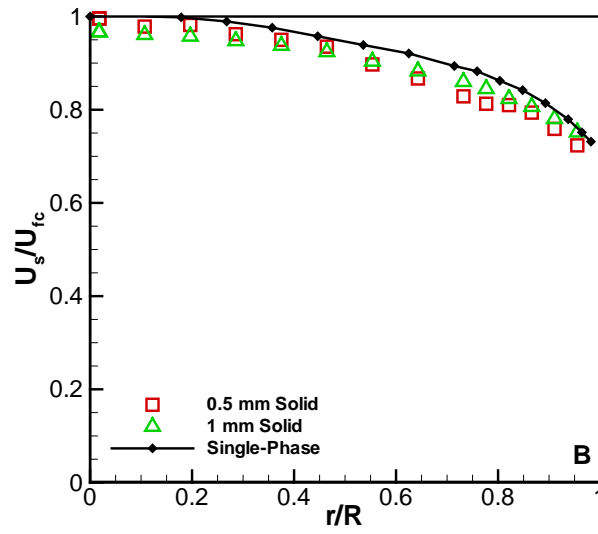
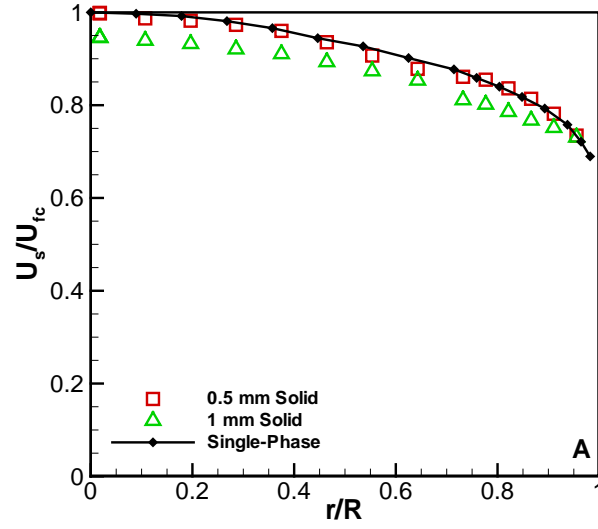


Figure 6-12. Solid mean velocity at 1.7% solids. A)  $Re = 2.0 \times 10^5$ , B)  $Re = 3.35 \times 10^5$  and C)  $Re = 5.0 \times 10^5$

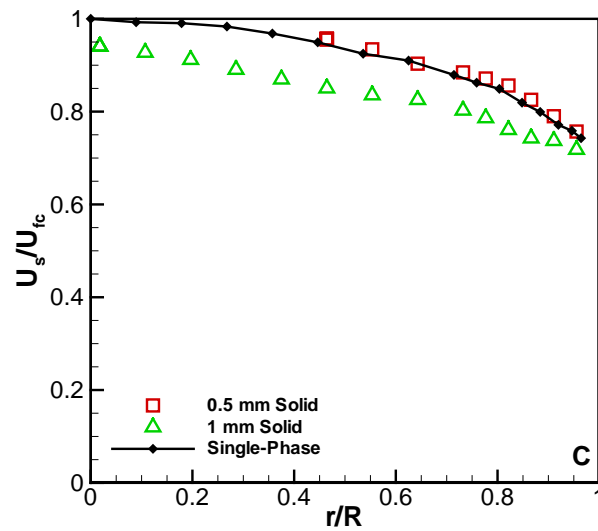
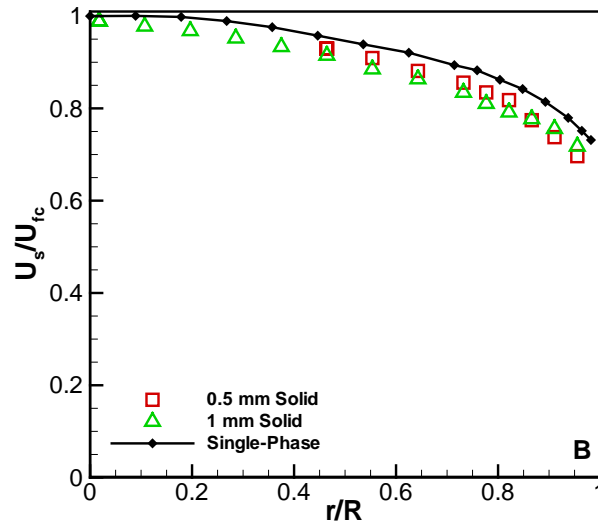
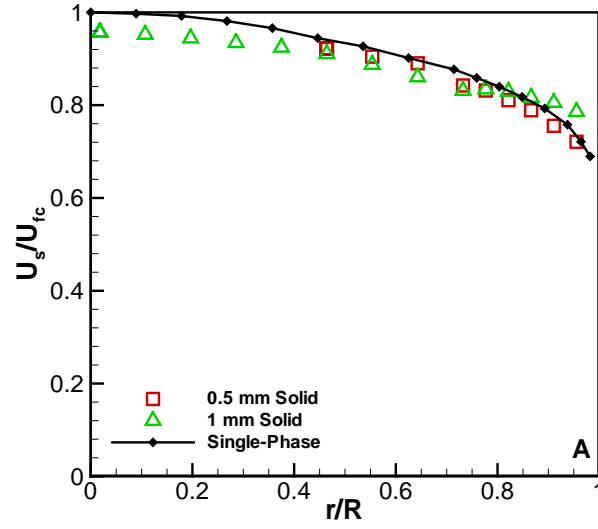


Figure 6-13. Solid mean velocity at 3% solids. A)  $Re = 2.0 \times 10^5$ , B)  $Re = 3.35 \times 10^5$  and C)  $Re = 5.0 \times 10^5$

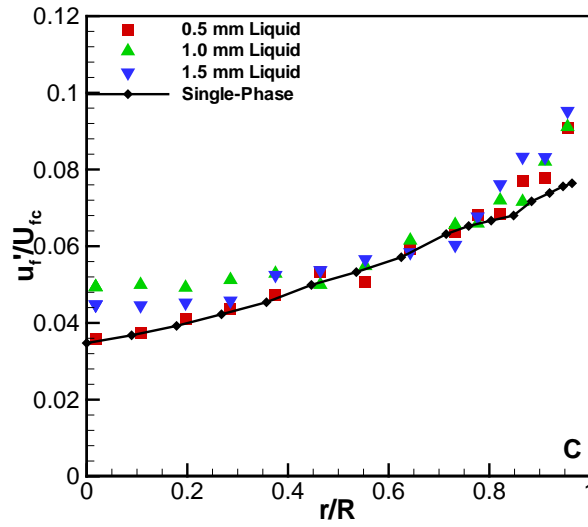
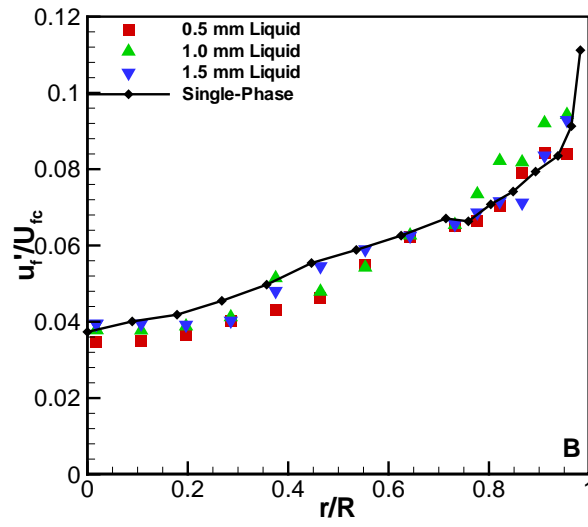
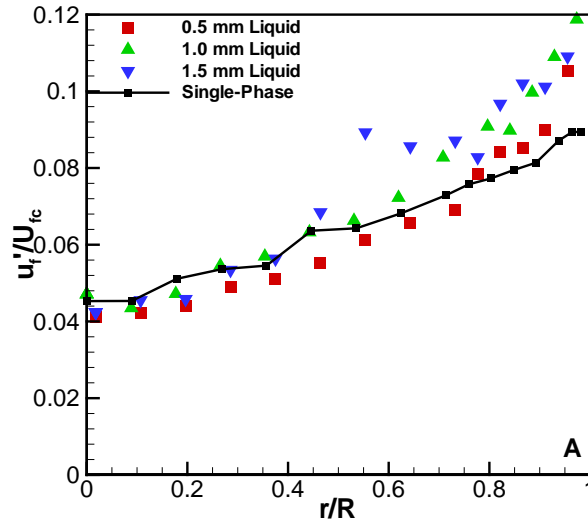


Figure 6-14. Fluid fluctuating velocity at 0.7% solids. A)  $Re = 2.0 \times 10^5$ , B)  $Re = 3.35 \times 10^5$  and C)  $Re = 5.0 \times 10^5$

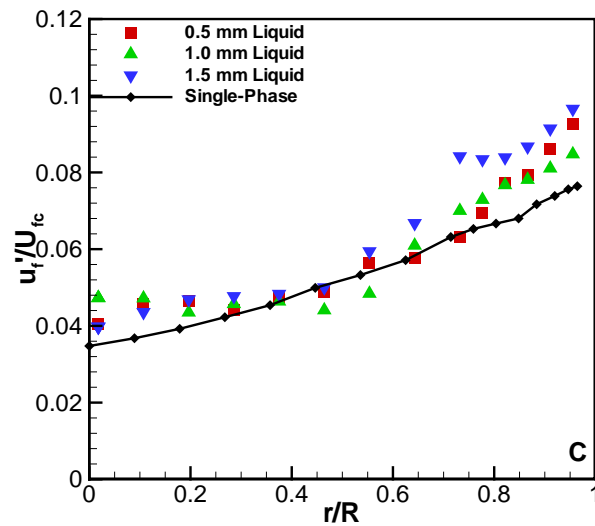
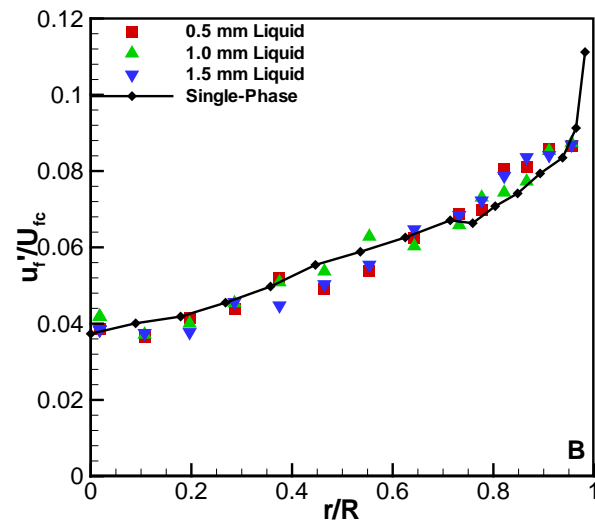
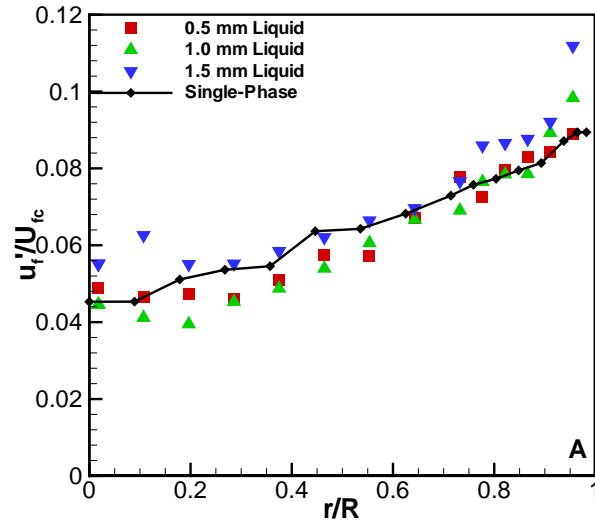


Figure 6-15. Fluid fluctuating velocity at 1.7% solids. A)  $Re = 2.0 \times 10^5$ , B)  $Re = 3.35 \times 10^5$  and C)  $Re = 5.0 \times 10^5$

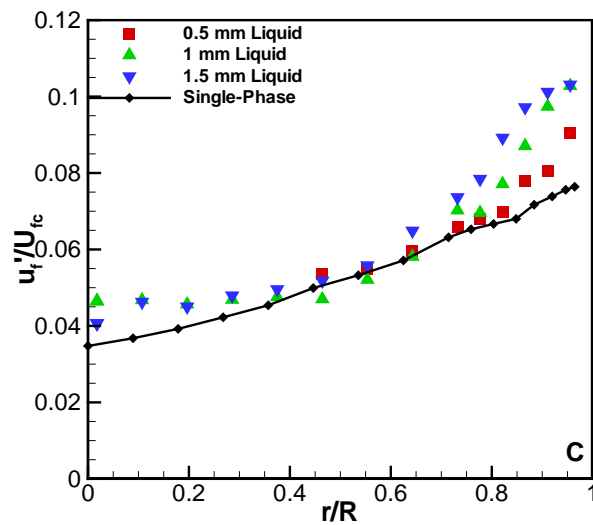
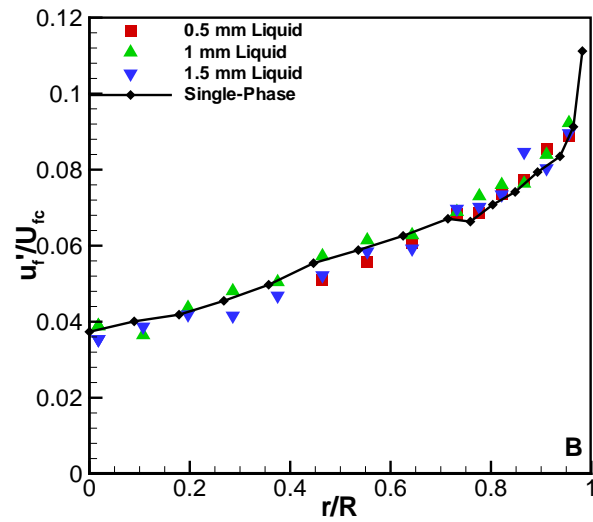
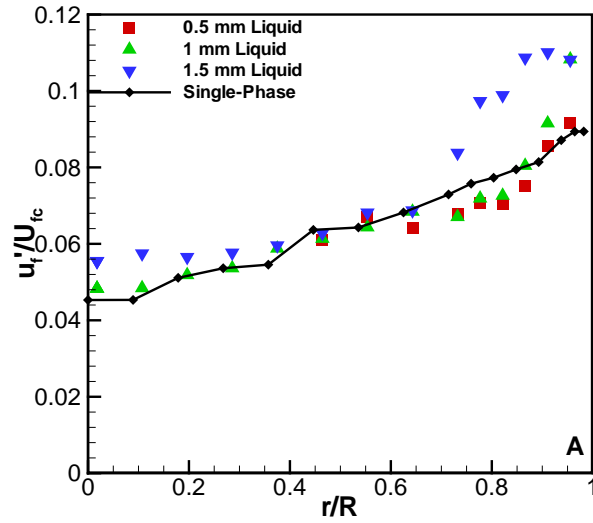


Figure 6-16. Fluid fluctuating velocity at 3% solids. A)  $Re = 2.0 \times 10^5$ , B)  $Re = 3.35 \times 10^5$  and C)  $Re = 5.0 \times 10^5$

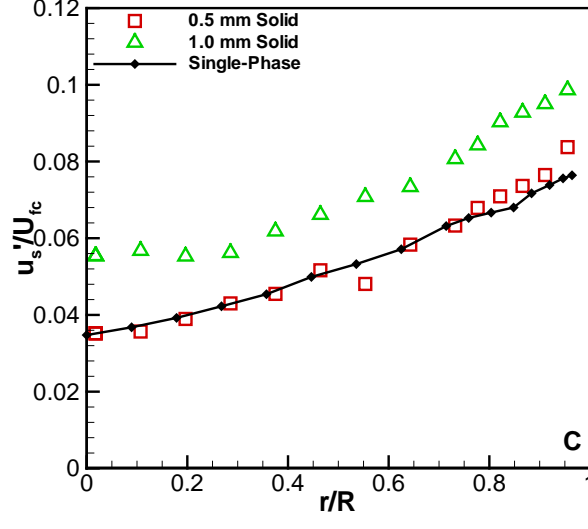
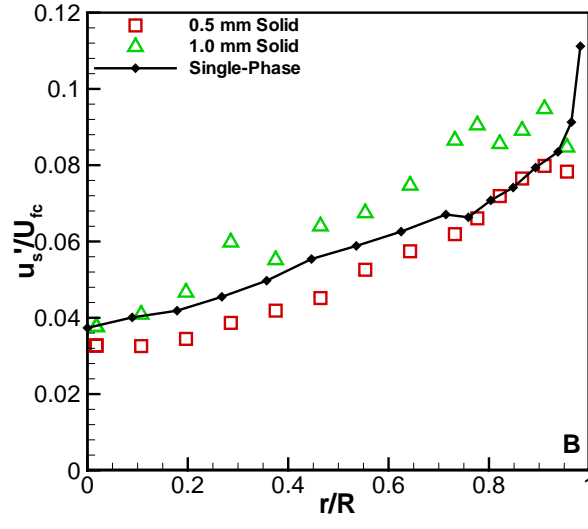
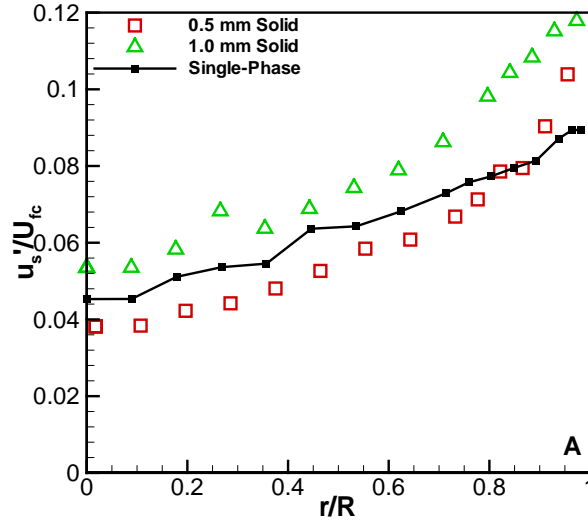


Figure 6-17. Solid fluctuating velocity at 0.7% solids. A)  $Re = 2.0 \times 10^5$ , B)  $Re = 3.35 \times 10^5$  and C)  $Re = 5.0 \times 10^5$

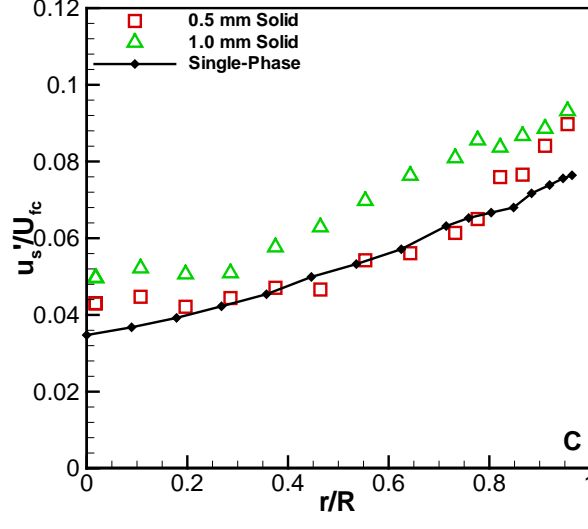
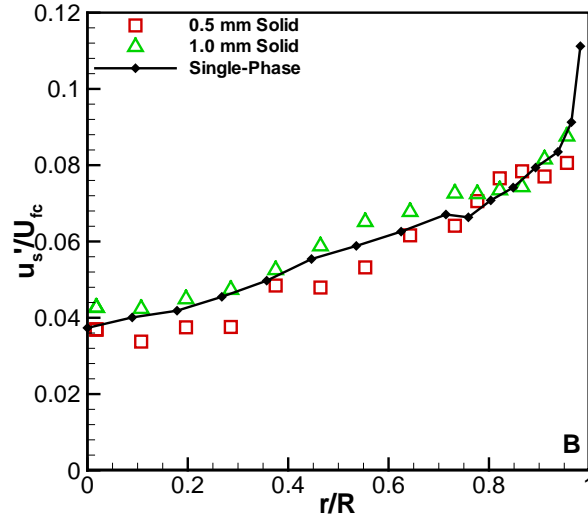
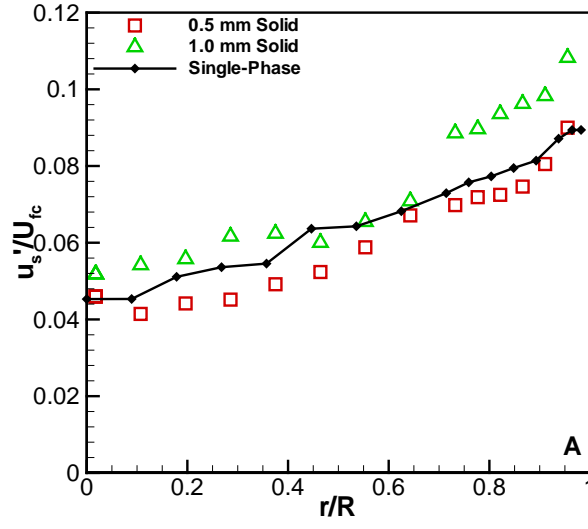


Figure 6-18. Solid fluctuating velocity 1.7% solids. A)  $Re = 2.0 \times 10^5$ , B)  $Re = 3.35 \times 10^5$  and C)  $Re = 5.0 \times 10^5$

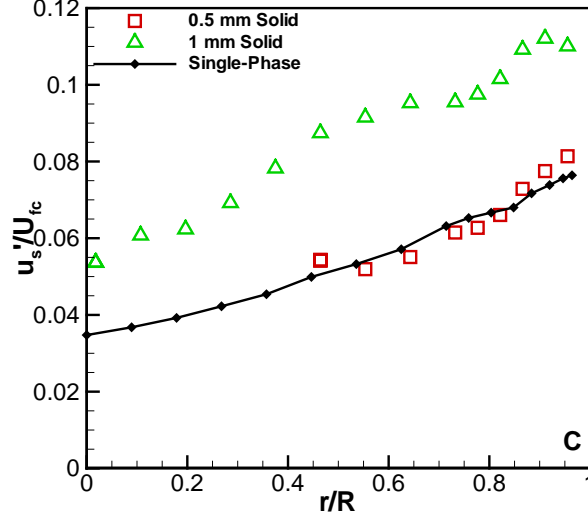
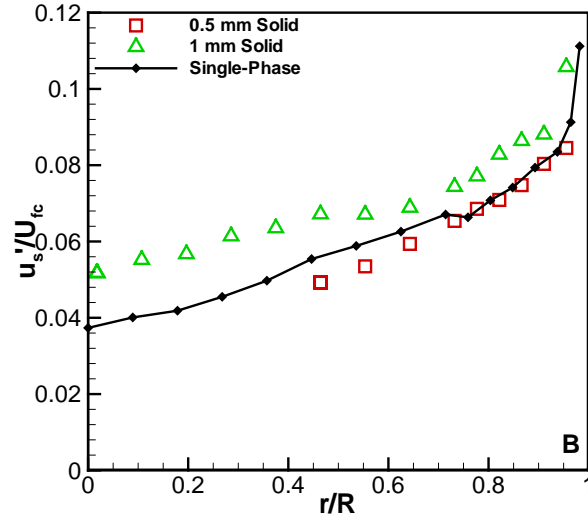
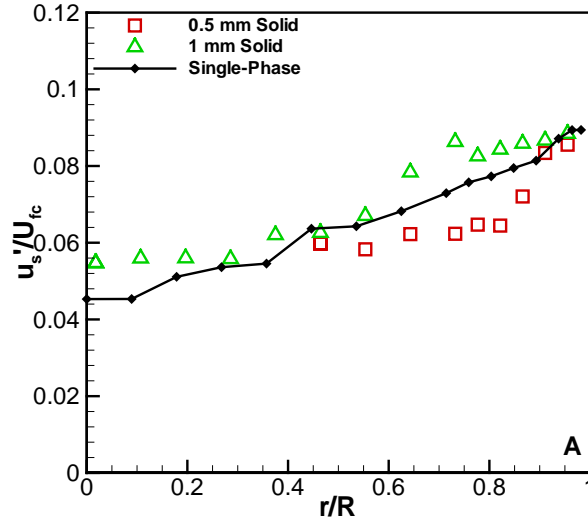


Figure 6-19. Solid fluctuating velocity at 3% solids. A)  $Re = 2.0 \times 10^5$ , B)  $Re = 3.35 \times 10^5$  and C)  $Re = 5.0 \times 10^5$

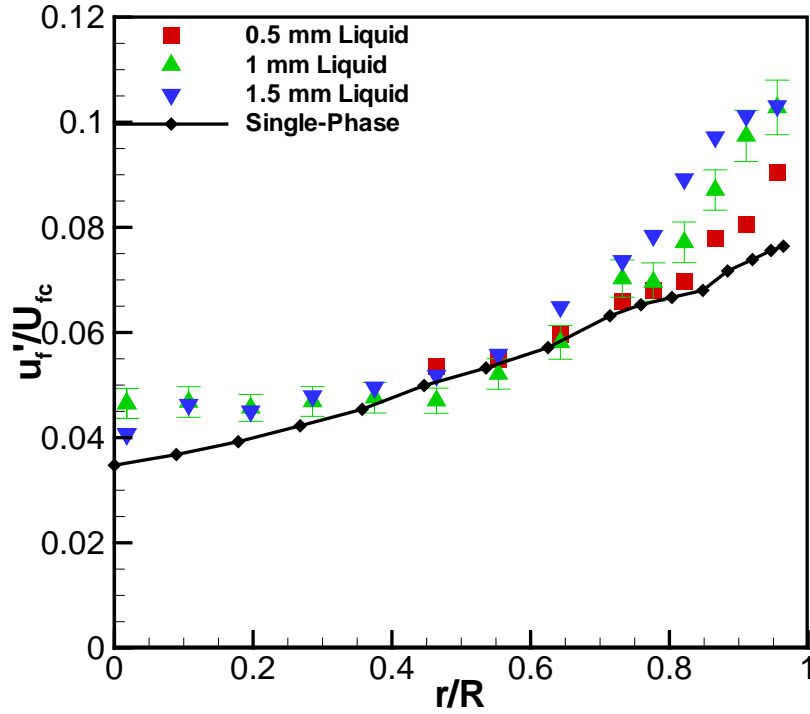


Figure 6-20. Fluid fluctuating velocity error based on ensemble size for 3% solids at  $Re=5.0 \times 10^5$

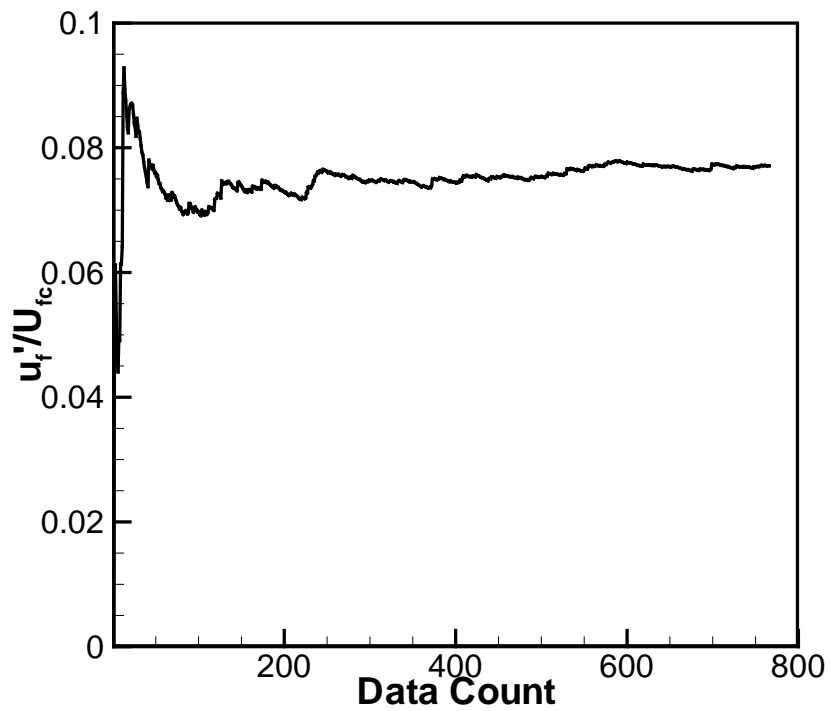


Figure 6-21. Evolution of  $u'_f$  with data count for 1 mm particles at  $r/R=0.82$  for 3% solids at  $Re=5.0 \times 10^5$

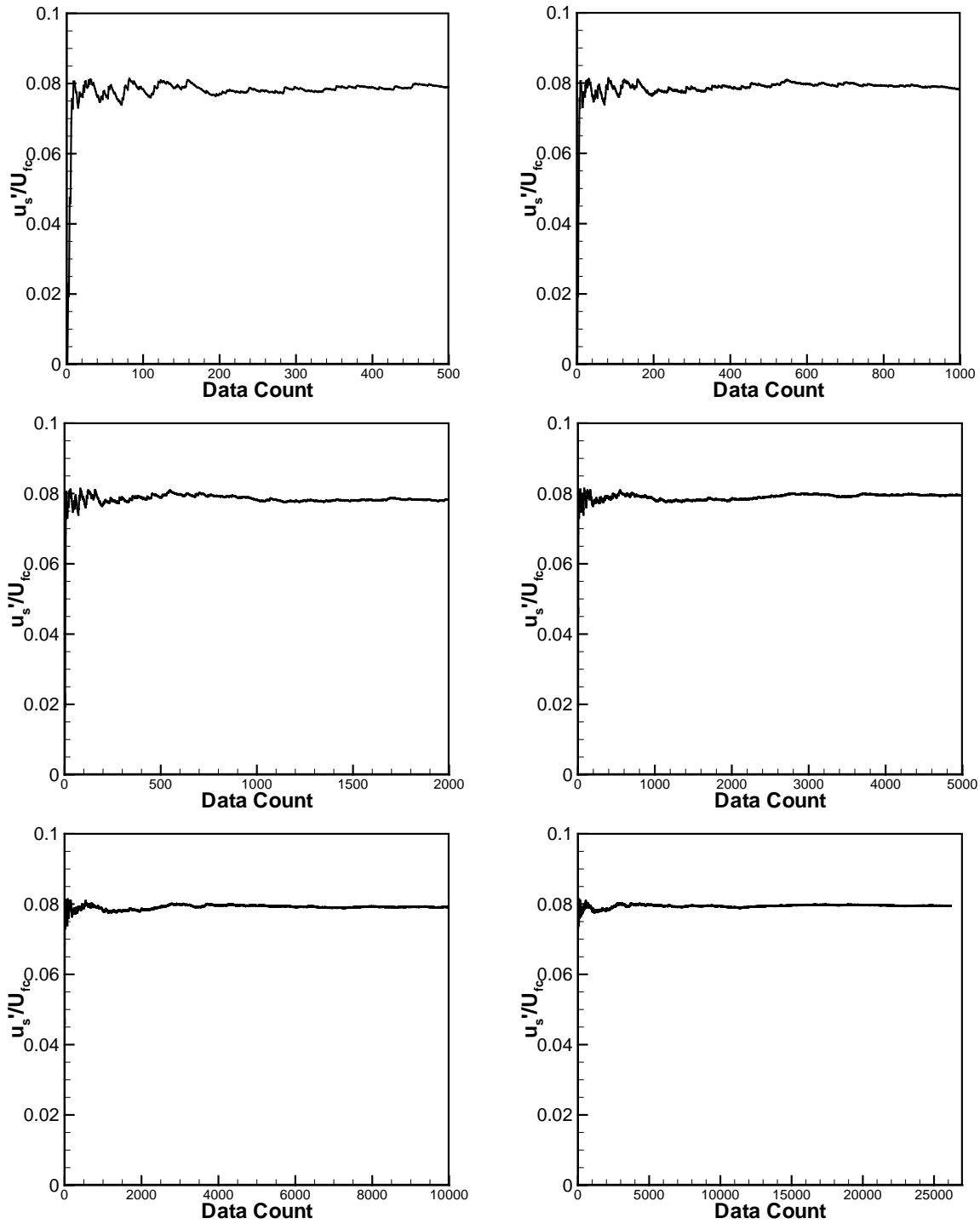


Figure 6-22. Evolution of  $u'_s$  with data count for 0.5 mm particles at  $r/R=0.91$  for 0.7% solids at  $Re=3.35 \times 10^5$

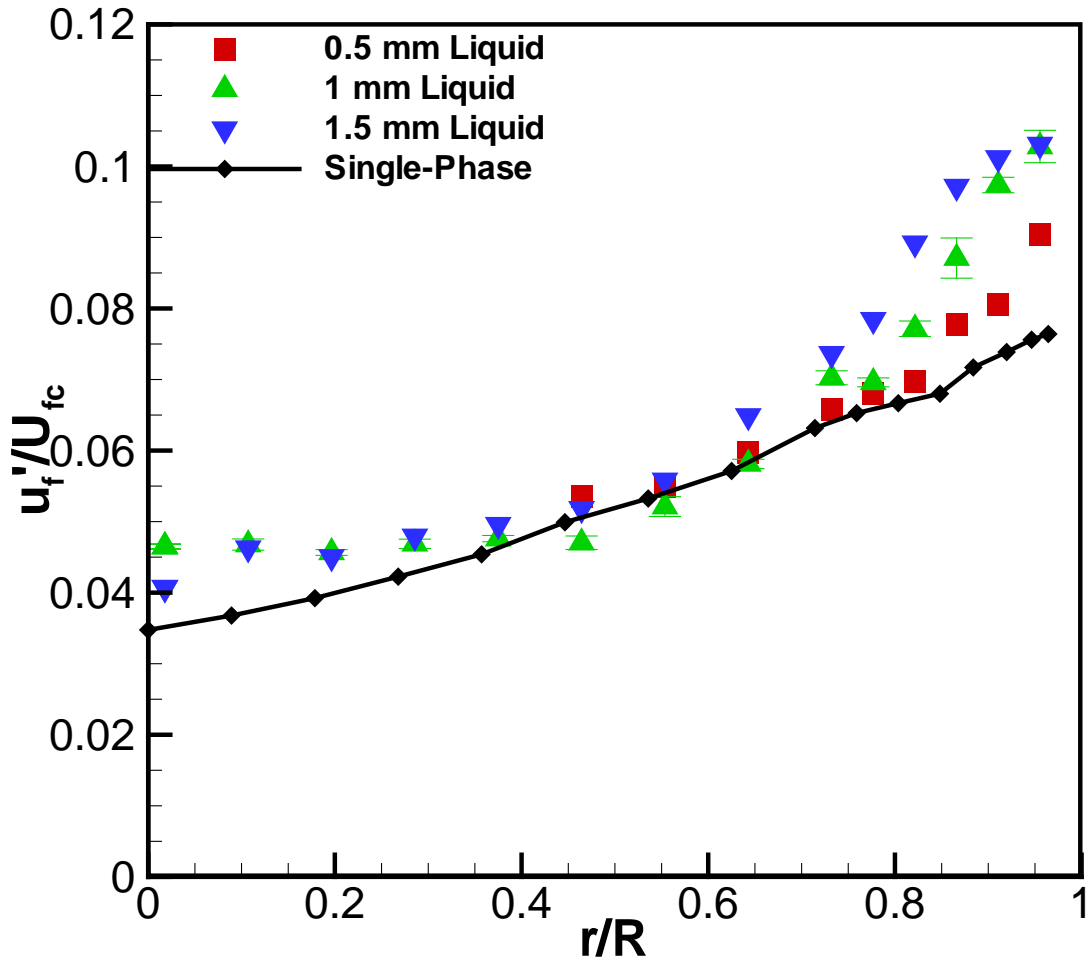


Figure 6-23. Fluid fluctuating velocity error based on standard deviation of  $u_f'$  after 250 measurements for 3% solids at  $Re=5.0 \times 10^5$

## CHAPTER 7 CONCLUSIONS AND RECOMMENDATIONS

The main goal of this dissertation was the acquisition of benchmark multiphase flow data—non-intrusive mean and fluctuating velocity measurements of a turbulent liquid-solid pipe flow. These data map the transition from a viscous-dominated to an inertial or collision-dominated flow. The experiments were designed such that a range of particle sizes, solids concentrations, and flow rates could be investigated. The data are needed in the validation of computational fluid dynamic (CFD) models which can be used to predict flow and transport properties of multiphase flows in relevant industrial settings. Current models which are built on kinetic theory concepts are incapable of predicting the flow behavior as viscous forces become significant.

Prior to the addition of the solid-phase, a single-phase base needed to be established. This consisted of velocity and pressure measurements. These two sets of measurements each revealed interesting phenomena not previously documented. The first was the acquisition of pressure data for flow in pipe bends at a novel combination of conditions—large pipe curvature at high  $Re$ . It was found that upstream effects occur well beyond a few pipe diameters prior to a pipe bend provided the  $Re$  is sufficiently high. The pressure difference between the outside and the inside of the pipe in the bend, as well as downstream of the pipe bend, is weakly dependent on  $Re$ . Existing correlations for total bend pressure loss significantly under predict the pressure drop in the bend and fail to capture a decrease in  $k_t$  with increasing  $Re$ . Finally, independent of exit configuration, the loss coefficient varies linearly throughout the bend, signifying that the effective length of the pipe is equal to its actual length, and wall friction is the dominant process contributing to pressure loss in bends of  $R_b/R \geq 24$ .

The second involved a significant variation in the reported values of single-phase gas turbulence intensity among the commonly cited references of these measurements. In both gas and liquid flow, this variation exceeds typical errors associated with the flow measurement techniques. The magnitude of the turbulence velocity fluctuations in water is consistently higher than in air at the same  $Re$ . In addition, the magnitude of the variations in the measurements of turbulent velocity is greater in liquid versus gas flow. In air, the turbulent velocity exhibits no  $Re$  dependence far from the wall; in water, there is a  $Re$  dependency. In air, turbulent velocity profiles measured using LDV are consistently flatter than those obtained from hot wire measurements. Based on these results the single-phase measurements were deemed to be in agreement with established values, proving the suitability of the experimental flow facility and instrumentation for two-phase experiments.

Finally, the solid-phase was added to the experimental facility and two-phase measurements of velocity and pressure were obtained. The pressure results indicate little change over the single-phase pressure gradients except at 0.7% and 1.7% at  $Re = 5.0 \times 10^5$  where drag reduction was observed. Further measurements at  $Re > 5.0 \times 10^5$  are necessary to see if the drag reduction persists over a wider range of  $Re$  and if it occurs at higher  $Re$  with the other particle sizes.

The velocity results show an increase in particle independence from the fluid with increasing Bagnold and Stokes number. In general, the 0.5 mm particles damp the fluid turbulence while the 1.0 mm and 1.5 mm particles are either neutral or enhance the turbulence. The solid turbulence of the 1.0 mm particles exceeds that of the fluid in their presence, while the solid-phase turbulence of the 0.5 mm particles is less than the

fluid in their presence. The turbulence of both phases becomes increasingly flat near the center of the pipe with increasing  $Re$  and solids loading. This is in agreement with the flat profiles of both fluid and solid turbulence in inertia dominated gas-solid flows.

The results reveal the need for further investigation into turbulence enhancement as a function of  $Re$  and particle size. Specifically, at what  $Re$  and/or  $Re_p$  does vortex shedding and wake formation occur and how does this balance with the decrease in turbulence with increasing  $Re$ . Other recommendations for future work include the acquisition of the particle velocity for the 1.5 mm particles, which constitute Bagnold numbers from the upper-transitional to the lower grain-inertia regime. These measurements can be obtained with the proper LDV/PDPA lenses which are available for the new LDV/PDPA that has been purchased. The new LDV/PDPA will also allow for radial velocity measurements—data that will be beneficial for the validation of CFD models. This validation includes the analysis of current CFD models to examine their ability to predict the experimental results and the subsequent development of new constitutive relationships that better capture fluid-particle interactions.

The current data are also limited to solids concentrations of 3% by volume or less. However, industrial slurries are typically composed of a higher volume of solids. Increasing the solids concentration would require the matching of index of refraction of the solid and liquid. A solution of sodium-iodine is a potential candidate for the fluid which can be manipulated to match that of the current glass particles. Increasing the fluid velocity to accommodate a larger range of  $Re$  is also possible. This can be achieved by increasing the pump speed and also by increasing the temperature of the water. The two methods, when combined would allow for the investigation of  $Re > 10^6$ .

Other potential investigations, which do not require any modifications to the current experimental setup, include measuring the effects of a bi-modal particle size distribution.

APPENDIX A  
EXPERIMENTAL VELOCITY DATA

**Two-Phase Flows**

**0.5 mm Particles**

Table A-1. Fluid and solid velocity measurements for 0.7% solids at  $Re=2.0 \times 10^5$

r/R	$U_f$ (m/s)	$u_f'$ (m/s)	$U_s$ (m/s)	$u_s'$ (m/s)
0.955	2.199	0.329	2.215	0.324
0.911	2.344	0.281	2.382	0.282
0.866	2.461	0.266	2.447	0.248
0.821	2.587	0.263	2.607	0.245
0.777	2.644	0.245	2.624	0.223
0.732	2.658	0.216	2.648	0.209
0.643	2.775	0.205	2.794	0.190
0.554	2.825	0.191	2.818	0.182
0.464	2.904	0.172	2.919	0.164
0.375	3.005	0.160	3.002	0.150
0.286	3.076	0.153	3.077	0.138
0.196	3.078	0.137	3.069	0.132
0.107	3.097	0.132	3.090	0.120
0.018	3.122	0.128	3.103	0.119

Table A-2. Fluid and solid velocity measurements for 1.7% solids at  $Re=2.0 \times 10^5$

r/R	$U_f$ (m/s)	$u_f'$ (m/s)	$U_s$ (m/s)	$u_s'$ (m/s)
0.955	2.311	0.282	2.327	0.285
0.911	2.462	0.267	2.476	0.255
0.866	2.562	0.263	2.578	0.236
0.821	2.633	0.252	2.649	0.230
0.777	2.692	0.230	2.708	0.228
0.732	2.749	0.246	2.728	0.221
0.643	2.782	0.213	2.783	0.213
0.554	2.891	0.181	2.873	0.186
0.464	2.966	0.182	2.964	0.166
0.375	3.048	0.161	3.042	0.156
0.286	3.119	0.146	3.083	0.143
0.196	3.136	0.150	3.112	0.140
0.107	3.149	0.147	3.127	0.131
0.018	3.168	0.155	3.163	0.146

Table A-3. Fluid and solid velocity measurements for 3% solids at  $Re=2.0 \times 10^5$

$r/R$	$U_f$ (m/s)	$u_f'$ (m/s)	$U_s$ (m/s)	$u_s'$ (m/s)
0.955	2.463	0.309	2.430	0.288
0.911	2.565	0.288	2.546	0.281
0.866	2.647	0.253	2.659	0.243
0.821	2.725	0.237	2.732	0.217
0.777	2.789	0.238	2.802	0.218
0.732	2.853	0.228	2.839	0.210
0.643	2.982	0.216	3.000	0.210
0.554	3.049	0.226	3.048	0.196
0.464	3.108	0.206	3.106	0.202

Table A-4. Fluid and solid velocity measurements for 0.7% solids at  $Re=3.35 \times 10^5$

$r/R$	$U_f$ (m/s)	$u_f'$ (m/s)	$U_s$ (m/s)	$u_s'$ (m/s)
0.955	3.716	0.414	3.730	0.386
0.911	3.889	0.415	3.902	0.394
0.866	4.036	0.389	4.028	0.377
0.821	4.205	0.347	4.250	0.355
0.777	4.271	0.328	4.235	0.326
0.732	4.390	0.321	4.375	0.306
0.643	4.516	0.307	4.445	0.283
0.554	4.588	0.271	4.560	0.259
0.464	4.696	0.229	4.680	0.223
0.375	4.774	0.213	4.781	0.207
0.286	4.857	0.199	4.842	0.191
0.196	4.878	0.180	4.866	0.170
0.107	4.904	0.172	4.897	0.161
0.018	4.933	0.171	4.924	0.161

Table A-5. Fluid and solid velocity measurements for 1.7% solids at  $Re=3.35 \times 10^5$

$r/R$	$U_f$ (m/s)	$u_f'$ (m/s)	$U_s$ (m/s)	$u_s'$ (m/s)
0.955	3.645	0.441	3.687	0.411
0.911	3.814	0.437	3.868	0.393
0.866	4.022	0.413	4.045	0.400
0.821	4.146	0.411	4.127	0.390
0.777	4.206	0.356	4.142	0.360
0.732	4.254	0.350	4.223	0.327
0.643	4.454	0.318	4.418	0.314
0.554	4.580	0.274	4.572	0.271
0.464	4.757	0.250	4.766	0.244
0.375	4.877	0.264	4.841	0.247
0.286	4.920	0.224	4.903	0.192
0.196	5.031	0.212	5.004	0.191
0.107	5.013	0.187	4.986	0.172
0.018	5.096	0.197	5.076	0.188

Table A-6. Fluid and solid velocity measurements for 3% solids at  $Re=3.35 \times 10^5$

r/R	$U_f$ (m/s)	$u_f'$ (m/s)	$U_s$ (m/s)	$u_s'$ (m/s)
0.955	3.579	0.457	3.587	0.435
0.911	3.828	0.440	3.798	0.414
0.866	4.003	0.397	3.988	0.385
0.821	4.210	0.379	4.212	0.365
0.777	4.333	0.353	4.298	0.353
0.732	4.399	0.352	4.407	0.337
0.643	4.554	0.312	4.538	0.306
0.554	4.662	0.287	4.681	0.275
0.464	4.804	0.263	4.786	0.254

Table A-7. Fluid and solid velocity measurements for 0.7% solids at  $Re=5.0 \times 10^5$

r/R	$U_f$ (m/s)	$u_f'$ (m/s)	$U_s$ (m/s)	$u_s'$ (m/s)
0.955	5.308	0.649	5.302	0.598
0.911	5.792	0.556	5.788	0.546
0.866	5.962	0.550	5.921	0.526
0.821	6.116	0.489	6.095	0.507
0.777	6.197	0.487	6.180	0.485
0.732	6.346	0.455	6.310	0.452
0.643	6.453	0.423	6.447	0.417
0.554	6.738	0.362	6.720	0.344
0.464	6.581	0.381	6.575	0.369
0.375	6.816	0.337	6.824	0.325
0.286	6.910	0.311	6.927	0.307
0.196	7.015	0.293	7.030	0.278
0.107	7.115	0.267	7.106	0.255
0.018	7.144	0.255	7.118	0.252

Table A-8. Fluid and solid velocity measurements for 1.7% solids at  $Re=5.0 \times 10^5$

r/R	$U_f$ (m/s)	$u_f'$ (m/s)	$U_s$ (m/s)	$u_s'$ (m/s)
0.955	5.409	0.652	5.378	0.631
0.911	5.649	0.605	5.656	0.591
0.866	5.978	0.559	5.918	0.538
0.821	6.026	0.543	5.971	0.534
0.777	6.179	0.488	6.117	0.457
0.732	6.247	0.444	6.246	0.432
0.643	6.538	0.406	6.538	0.394
0.554	6.580	0.397	6.537	0.381
0.464	6.603	0.344	6.589	0.328
0.375	6.868	0.333	6.870	0.331
0.286	7.024	0.310	7.008	0.312
0.196	7.144	0.326	7.118	0.296
0.107	7.000	0.322	6.957	0.315
0.018	7.032	0.284	7.015	0.303

Table A-9. Fluid and solid velocity measurements for 3% solids at  $Re=5.0 \times 10^5$

$r/R$	$U_f$ (m/s)	$u_f'$ (m/s)	$U_s$ (m/s)	$u_s'$ (m/s)
0.955	5.389	0.654	5.475	0.588
0.911	5.735	0.583	5.713	0.560
0.866	5.970	0.563	5.969	0.527
0.821	6.195	0.504	6.191	0.478
0.777	6.303	0.492	6.301	0.454
0.732	6.354	0.476	6.396	0.445
0.643	6.510	0.432	6.532	0.398
0.554	6.764	0.397	6.755	0.376
0.464	6.904	0.387	6.916	0.393

### 1.0 mm Particles

Table A-10. Fluid and solid velocity measurements for 0.7% solids at  $Re=2.0 \times 10^5$

$r/R$	$U_f$ (m/s)	$u_f'$ (m/s)	$U_s$ (m/s)	$u_s'$ (m/s)
0.955	2.173	0.369	2.289	0.431
0.911	2.340	0.339	2.331	0.409
0.866	2.397	0.310	2.396	0.386
0.821	2.502	0.279	2.459	0.351
0.777	2.573	0.282	2.516	0.332
0.688	2.662	0.257	2.630	0.292
0.598	2.760	0.225	2.714	0.263
0.509	2.855	0.206	2.778	0.244
0.420	2.923	0.197	2.890	0.229
0.330	3.007	0.177	2.954	0.210
0.241	3.053	0.169	2.931	0.221
0.152	3.092	0.147	3.018	0.194
0.063	3.110	0.135	3.057	0.178
0.027	3.107	0.146	3.057	0.190

Table A-11. Fluid and solid velocity measurements for 1.7% solids at  $Re=2.0 \times 10^5$

$r/R$	$U_f$ (m/s)	$u_f'$ (m/s)	$U_s$ (m/s)	$u_s'$ (m/s)
0.955	2.258	0.297	2.207	0.327
0.911	2.404	0.270	2.269	0.297
0.866	2.477	0.237	2.317	0.291
0.821	2.535	0.237	2.373	0.283
0.777	2.600	0.231	2.420	0.271
0.732	2.646	0.209	2.449	0.267
0.643	2.722	0.201	2.577	0.214
0.554	2.790	0.183	2.638	0.198
0.464	2.833	0.163	2.697	0.181
0.375	2.910	0.147	2.749	0.188
0.286	2.954	0.137	2.780	0.186
0.196	2.979	0.119	2.815	0.168
0.107	3.007	0.124	2.837	0.164
0.018	3.020	0.135	2.855	0.156

Table A-12. Fluid and solid velocity measurements for 3% solids at  $Re=2.0 \times 10^5$

$r/R$	$U_f$ (m/s)	$u_f'$ (m/s)	$U_s$ (m/s)	$u_s'$ (m/s)
0.955	2.337	0.342	2.482	0.279
0.911	2.430	0.289	2.544	0.274
0.866	2.538	0.254	2.578	0.271
0.821	2.622	0.229	2.619	0.266
0.777	2.679	0.227	2.636	0.261
0.732	2.727	0.212	2.625	0.273
0.643	2.799	0.216	2.718	0.247
0.554	2.874	0.203	2.802	0.212
0.464	2.912	0.194	2.876	0.198
0.375	2.967	0.186	2.919	0.196
0.286	3.070	0.169	2.951	0.176
0.196	3.126	0.164	2.982	0.177
0.107	3.141	0.153	3.007	0.177
0.018	3.158	0.153	3.022	0.173

Table A-13. Fluid and solid velocity measurements for 0.7% solids at  $Re=3.35 \times 10^5$

$r/R$	$U_f$ (m/s)	$u_f'$ (m/s)	$U_s$ (m/s)	$u_s'$ (m/s)
0.955	3.625	0.475	4.058	0.427
0.911	3.889	0.464	3.963	0.478
0.866	4.080	0.413	4.040	0.449
0.821	4.211	0.414	4.149	0.431
0.777	4.315	0.370	4.183	0.456
0.688	4.476	0.330	4.304	0.436
0.598	4.617	0.316	4.487	0.377
0.509	4.699	0.273	4.583	0.340
0.420	4.827	0.242	4.650	0.323
0.330	4.898	0.260	4.768	0.278
0.241	4.983	0.208	4.790	0.301
0.152	5.030	0.196	4.870	0.235
0.063	5.056	0.190	4.929	0.206
0.027	5.041	0.191	4.964	0.190

Table A-14. Fluid and solid velocity measurements for 1.7% solids at  $Re=3.35 \times 10^5$

$r/R$	$U_f$ (m/s)	$u_f'$ (m/s)	$U_s$ (m/s)	$u_s'$ (m/s)
0.955	3.890	0.440	3.783	0.441
0.911	3.969	0.429	3.927	0.410
0.866	4.144	0.389	4.058	0.374
0.821	4.251	0.374	4.144	0.370
0.777	4.380	0.368	4.251	0.365
0.732	4.466	0.331	4.328	0.365
0.643	4.581	0.303	4.442	0.341
0.554	4.660	0.316	4.547	0.328
0.464	4.786	0.270	4.650	0.296
0.375	4.864	0.256	4.718	0.264
0.286	4.938	0.228	4.769	0.238
0.196	4.971	0.201	4.818	0.226
0.107	4.994	0.187	4.835	0.213
0.018	5.032	0.211	4.865	0.215

Table A-15. Fluid and solid velocity measurements for 3% solids at  $Re=3.35 \times 10^5$

$r/R$	$U_f$ (m/s)	$u_f'$ (m/s)	$U_s$ (m/s)	$u_s'$ (m/s)
0.955	3.519	0.429	3.338	0.431
0.911	3.657	0.390	3.515	0.410
0.866	3.751	0.355	3.614	0.402
0.821	3.867	0.353	3.682	0.385
0.777	3.962	0.340	3.768	0.359
0.732	4.055	0.320	3.880	0.346
0.643	4.197	0.292	4.016	0.320
0.554	4.289	0.286	4.116	0.312
0.464	4.385	0.266	4.254	0.312
0.375	4.479	0.235	4.341	0.295
0.286	4.539	0.224	4.428	0.286
0.196	4.605	0.203	4.502	0.264
0.107	4.651	0.170	4.548	0.257
0.018	4.079	0.159	4.599	0.241

Table A-16. Fluid and solid velocity measurements for 0.7% solids at  $Re=5.0 \times 10^5$

$r/R$	$U_f$ (m/s)	$u_f'$ (m/s)	$U_s$ (m/s)	$u_s'$ (m/s)
0.955	5.190	0.643	5.354	0.696
0.911	5.511	0.579	5.510	0.670
0.866	5.813	0.505	5.658	0.655
0.821	5.903	0.508	5.761	0.637
0.777	6.044	0.465	5.846	0.595
0.732	6.151	0.463	5.925	0.569
0.643	6.265	0.434	6.185	0.518
0.554	6.484	0.387	6.371	0.500
0.464	6.599	0.352	6.505	0.467
0.375	6.721	0.373	6.644	0.436
0.286	6.873	0.361	6.794	0.397
0.196	6.938	0.347	6.881	0.390
0.107	7.058	0.352	6.922	0.400
0.018	7.055	0.348	6.952	0.391

Table A-17. Fluid and solid velocity measurements for 1.7% solids at  $Re=5.0 \times 10^5$

$r/R$	$U_f$ (m/s)	$u_f'$ (m/s)	$U_s$ (m/s)	$u_s'$ (m/s)
0.955	5.366	0.597	5.270	0.656
0.911	5.560	0.571	5.388	0.624
0.866	5.770	0.550	5.505	0.611
0.821	5.896	0.540	5.570	0.589
0.777	6.026	0.513	5.636	0.603
0.732	6.186	0.493	5.805	0.570
0.643	6.320	0.429	5.955	0.538
0.554	6.451	0.341	6.161	0.491
0.464	6.587	0.311	6.267	0.443
0.375	6.708	0.327	6.366	0.406
0.286	6.791	0.322	6.453	0.359
0.196	6.854	0.306	6.541	0.357
0.107	6.956	0.333	6.573	0.368
0.018	7.043	0.333	6.656	0.350

Table A-18. Fluid and solid velocity measurements for 3% solids at  $Re=5.0 \times 10^5$

$r/R$	$U_f$ (m/s)	$u_f'$ (m/s)	$U_s$ (m/s)	$u_s'$ (m/s)
0.955	5.202	0.702	4.905	0.752
0.911	5.381	0.665	5.036	0.766
0.866	5.570	0.595	5.073	0.746
0.821	5.757	0.527	5.197	0.694
0.777	5.927	0.475	5.370	0.666
0.732	5.989	0.480	5.482	0.652
0.643	6.174	0.397	5.639	0.651
0.554	6.378	0.356	5.708	0.625
0.464	6.521	0.321	5.808	0.597
0.375	6.559	0.325	5.941	0.534
0.286	6.696	0.320	6.083	0.473
0.196	6.740	0.312	6.229	0.426
0.107	6.817	0.319	6.334	0.415
0.018	6.830	0.318	6.424	0.366

## 1.5 mm Particles

Table A-19. Fluid velocity measurements for 0.7% solids at  $Re=2.0 \times 10^5$

$r/R$	$U_f$ (m/s)	$u_f'$ (m/s)
0.955	2.222	0.323
0.911	2.336	0.300
0.866	2.404	0.302
0.821	2.482	0.286
0.777	2.565	0.245
0.732	2.583	0.258
0.643	2.664	0.253
0.554	2.731	0.264
0.464	2.770	0.203
0.375	2.858	0.167
0.286	2.906	0.158
0.196	2.940	0.136
0.107	2.992	0.135
0.018	2.961	0.126

Table A-20. Fluid velocity measurements for 1.7% solids at  $Re=2.0 \times 10^5$

$r/R$	$U_f$ (m/s)	$u_f'$ (m/s)
0.955	2.211	0.325
0.911	2.321	0.267
0.866	2.400	0.255
0.821	2.463	0.251
0.777	2.486	0.250
0.732	2.535	0.223
0.643	2.616	0.202
0.554	2.661	0.193
0.464	2.708	0.180
0.375	2.769	0.170
0.286	2.829	0.160
0.196	2.886	0.160
0.107	2.949	0.182
0.018	2.905	0.160

Table A-21. Fluid velocity measurements for 3% solids at  $Re=2.0 \times 10^5$

$r/R$	$U_f$ (m/s)	$u_f'$ (m/s)
0.955	2.093	0.301
0.911	2.183	0.307
0.866	2.276	0.303
0.821	2.381	0.276
0.777	2.407	0.271
0.732	2.422	0.234
0.643	2.544	0.192
0.554	2.619	0.190
0.464	2.627	0.175
0.375	2.642	0.166
0.286	2.706	0.161
0.196	2.751	0.158
0.107	2.763	0.160
0.018	2.788	0.155

Table A-22. Fluid velocity measurements for 0.7% solids at  $Re=3.35 \times 10^5$

$r/R$	$U_f$ (m/s)	$u_f'$ (m/s)
0.955	3.655	0.444
0.911	3.830	0.400
0.866	3.967	0.341
0.821	4.096	0.342
0.777	4.170	0.328
0.732	4.254	0.314
0.643	4.423	0.299
0.554	4.498	0.282
0.464	4.494	0.261
0.375	4.613	0.230
0.286	4.692	0.193
0.196	4.747	0.187
0.107	4.766	0.189
0.018	4.784	0.189

Table A-23. Fluid velocity measurements for 1.7% solids at  $Re=3.35 \times 10^5$

$r/R$	$U_f$ (m/s)	$u_f'$ (m/s)
0.955	3.691	0.413
0.911	3.888	0.400
0.866	3.937	0.398
0.821	4.032	0.374
0.777	4.130	0.344
0.732	4.188	0.326
0.643	4.319	0.308
0.554	4.396	0.264
0.464	4.478	0.239
0.375	4.593	0.213
0.286	4.654	0.217
0.196	4.669	0.180
0.107	4.734	0.178
0.018	4.758	0.183

Table A-24. Fluid velocity measurements for 3% solids at  $Re=3.35 \times 10^5$

$r/R$	$U_f$ (m/s)	$u_f'$ (m/s)
0.955	3.453	0.415
0.911	3.649	0.373
0.866	3.776	0.392
0.821	3.901	0.341
0.777	3.976	0.325
0.732	4.029	0.323
0.643	4.160	0.275
0.554	4.317	0.271
0.464	4.308	0.242
0.375	4.403	0.217
0.286	4.537	0.193
0.196	4.571	0.194
0.107	4.613	0.179
0.018	4.638	0.164

Table A-25. Fluid velocity measurements for 0.7% solids at  $Re=5.0 \times 10^5$

$r/R$	$U_f$ (m/s)	$u_f'$ (m/s)
0.955	5.505	0.662
0.911	5.773	0.579
0.866	5.973	0.579
0.821	6.025	0.529
0.777	6.167	0.471
0.732	6.280	0.419
0.643	6.439	0.406
0.554	6.554	0.394
0.464	6.762	0.374
0.375	6.774	0.365
0.286	6.901	0.318
0.196	7.002	0.315
0.107	6.924	0.310
0.018	6.956	0.311

Table A-26. Fluid velocity measurements for 1.7% solids at  $Re=5.0 \times 10^5$

$r/R$	$U_f$ (m/s)	$u_f'$ (m/s)
0.955	5.138	0.667
0.911	5.443	0.631
0.866	5.738	0.599
0.821	5.830	0.579
0.777	5.925	0.576
0.732	5.965	0.581
0.643	6.198	0.461
0.554	6.363	0.410
0.464	6.583	0.345
0.375	6.636	0.334
0.286	6.699	0.329
0.196	6.776	0.324
0.107	6.842	0.301
0.018	6.905	0.274

Table A-27. Fluid velocity measurements for 3% solids at  $Re=5.0 \times 10^5$

$r/R$	$U_f$ (m/s)	$u_f'$ (m/s)
0.955	4.938	0.713
0.911	5.265	0.700
0.866	5.504	0.672
0.821	5.696	0.617
0.777	5.871	0.543
0.732	6.019	0.509
0.643	6.286	0.449
0.554	6.350	0.386
0.464	6.517	0.358
0.375	6.632	0.343
0.286	6.718	0.332
0.196	6.847	0.312
0.107	6.924	0.320
0.018	6.919	0.282

### Reproducibility

Table A-28. Three measurements of solids fluctuating velocity for 1.0 mm particles at 0.7% solids at  $Re=2.0 \times 10^5$

$r/R$ 1	$u_s'$ 1	$r/R$ 2	$u_s'$ 2	$r/R$ 3	$u_s'$ 3
0.955	0.117	0.955	0.119	0.955	0.123
0.911	0.121	0.911	0.115	0.911	0.120
0.866	0.109	0.866	0.110	0.866	0.114
0.821	0.103	0.821	0.104	0.821	0.111
0.777	0.097	0.777	0.102	0.777	0.102
0.732	0.091	0.732	0.094	0.688	0.091
0.643	0.088	0.643	0.087	0.598	0.083
0.554	0.083	0.554	0.080	0.509	0.078
0.464	0.082	0.464	0.083	0.420	0.072
0.375	0.076	0.375	0.076	0.330	0.068
0.286	0.071	0.286	0.072	0.241	0.071
0.196	0.063	0.196	0.066	0.152	0.062
0.107	0.060	0.107	0.063	0.063	0.057
0.018	0.058	0.018	0.060	0.027	0.057

## Fully-Developed Flow

Table A-29. Solid mean and fluctuating velocity at two radii and two axial locations for 0.5 mm particles at 0.7% solids at  $Re=2.0 \times 10^5$

r/R	North Top		East Top		East Middle	
	$U_s$	$u_s'$	$U_s$	$u_s'$	$U_s$	$u_s'$
0.955	2.215	0.324	2.277	0.293	2.152	0.3196
0.911	2.382	0.282	2.38	0.2662	2.339	0.3049
0.866	2.447	0.248	2.512	0.2376	2.417	0.2893
0.821	2.607	0.245	2.599	0.2282	2.541	0.2294
0.777	2.624	0.223	2.693	0.2156	1.581	0.2322
0.732	2.648	0.209	2.763	0.2112	2.669	0.2008
0.643	2.794	0.190	2.821	0.1957	2.824	0.1991
0.554	2.818	0.182	2.888	0.1859	2.864	0.184
0.464	2.919	0.164	2.989	0.1661	2.945	0.167
0.375	3.002	0.150	3.067	0.1549	3.006	0.1435
0.286	3.077	0.138	3.112	0.1405	3.045	0.1355
0.196	3.069	0.132	3.146	0.1338	3.099	0.1349
0.107	3.090	0.120	3.142	0.1251	3.139	0.1384
0.018	3.103	0.119	3.146	0.123	3.098	0.1398

## Single-Phase Flows

Table A-30. Mean and fluctuating velocity of single phase water

r/R	$Re=2.0 \times 10^5$		$Re=3.35 \times 10^5$		$Re=5.0 \times 10^5$	
	$U_f$ (m/s)	$u_f'$ (m/s)	$U_f$ (m/s)	$u_f'$ (m/s)	$U_f$ (m/s)	$u_f'$ (m/s)
0.964	2.219	0.275	3.737	0.454	5.428	0.541
0.938	2.332	0.268	3.877	0.415	5.520	0.529
0.893	2.439	0.250	4.049	0.395	5.719	0.513
0.848	2.516	0.245	4.188	0.369	5.862	0.487
0.804	2.584	0.238	4.287	0.352	6.075	0.477
0.759	2.643	0.233	4.389	0.330	6.170	0.467
0.714	2.699	0.224	4.445	0.334	6.290	0.452
0.625	2.774	0.210	4.579	0.311	6.511	0.409
0.536	2.852	0.198	4.669	0.293	6.617	0.381
0.446	2.906	0.196	4.763	0.276	6.793	0.357
0.357	2.973	0.168	4.854	0.247	6.928	0.325
0.268	3.019	0.165	4.920	0.226	7.036	0.302
0.179	3.053	0.157	4.965	0.208	7.088	0.281
0.089	3.068	0.140	4.976	0.199	7.102	0.263
0.000	3.077	0.139	4.973	0.186	7.155	0.249

Table A-31. Fluctuating velocity of single phase water

r/R	Re=2.2x10 <sup>5</sup>	Re=3.6x10 <sup>5</sup>	Re=5.0x10 <sup>5</sup>	Re=6.1x10 <sup>5</sup>
	u <sub>f</sub> ' (m/s)			
0.973	0.241	0.553	0.610	0.698
0.955	0.241	0.454	0.562	0.671
0.929	0.234	0.415	0.544	0.626
0.893	0.231	0.395	0.503	0.616
0.848	0.220	0.369	0.480	0.581
0.804	0.212	0.352	0.470	0.562
0.759	0.197	0.330	0.448	0.536
0.714	0.193	0.334	0.439	0.526
0.625	0.187	0.311	0.393	0.500
0.536	0.174	0.293	0.358	0.464
0.446	0.163	0.276	0.335	0.439
0.357	0.149	0.247	0.307	0.399
0.268	0.142	0.226	0.285	0.361
0.179	0.140	0.208	0.266	0.337
0.089	0.132	0.199	0.255	0.333
0.000	0.124	0.186	0.247	0.318

APPENDIX B  
EXPERIMENTAL PRESSURE DATA

**Two-Phase Flows**

Table B-3. Pressure gradient for 0.5 mm particles

Re	Solids Concentration (Volume)		
	0.7%	1.7%	3%
	(kPa/m)	(kPa/m)	(kPa/m)
$2.0 \times 10^5$	10.61	10.775	10.951
$3.35 \times 10^5$	11.432	11.716	
$5.0 \times 10^5$	12.802	13.009	

Table B-3. Pressure gradient for 1.0 mm particles

Re	Solids Concentration (Volume)		
	0.7%	1.7%	3%
	(kPa/m)	(kPa/m)	(kPa/m)
$2.0 \times 10^5$	10.548	10.848	11.147
$3.35 \times 10^5$	11.727	11.851	12.114
$5.0 \times 10^5$	12.425	12.166	12.942

Table B-3. Pressure gradient for 1.5mm particles

Re	Solids Concentration (Volume)		
	0.7%	1.7%	3%
	(kPa/m)	(kPa/m)	(kPa/m)
$2.0 \times 10^5$	10.625	10.651	11.142
$3.35 \times 10^5$	11.463	11.282	11.365
$5.0 \times 10^5$	13.893	13.686	13.195

**Single-Phase Flows**

Table B-1. Pressure along vertical pipe and bend with sudden expansion at downstream tangent (Configuration A)

Distance from Bend Entrance (Diameters)	Re = $3.68 \times 10^5$		Re = $5.0 \times 10^5$		Re = $6.16 \times 10^5$		Re = $7.36 \times 10^5$		Re = $8.5 \times 10^5$	
	Inside (PSI)	Outside (PSI)	Inside (PSI)	Outside (PSI)	Inside (PSI)	Outside (PSI)	Inside (PSI)	Outside (PSI)	Inside (PSI)	Outside (PSI)
-37	4.19		5.86		8.15		10.65		13.40	
-32	3.58		5.25		7.60		10.02		12.76	
-27	3.00		4.63		6.95		8.88		12.05	
-22	2.39		3.92		6.17		8.57		11.13	
-17	1.65		2.98		5.06		7.42		9.40	
-12	0.91		2.24		4.02		6.15		7.95	
-7	0.30		1.46		3.14		5.18		6.74	
-2	-0.20		0.86		2.81		4.87		6.54	
0	-0.53	-0.46	0.42	0.58	2.26	2.54	4.23	4.64	5.74	6.22
4	-0.95	-0.93	-0.13	0.04	1.60	1.90	3.47	3.95	4.76	5.48
8	-1.29	-1.30	-0.48	-0.33	1.25	1.58	3.12	3.73	4.45	5.39
12	-1.82	-1.74	-1.15	-0.91	0.41	0.77	2.09	2.65	3.15	3.99
16	-2.03	-2.06	-1.40	-1.25	0.04	0.50	1.48	2.35	2.45	3.74
20	-2.12	-2.21	-1.49	-1.51	-0.13	-0.25	1.33	1.14	2.20	2.16
22	-2.06	-2.35	-1.35	-1.67	0.05	-0.34	1.56	1.09	2.51	2.07
27	-2.29	-2.56	-1.67	-1.96	-0.23	-0.73	1.25	0.55	2.18	1.38

Table B-2. Pressure along vertical pipe and bend with steel pipe at downstream tangent (Configuration B)

Distance from Bend Entrance (Diameters)	Re = 3.68x10 <sup>5</sup>		Re = 5.0x10 <sup>5</sup>		Re = 6.16x10 <sup>5</sup>		Re = 7.36x10 <sup>5</sup>		Re = 8.5x10 <sup>5</sup>	
	Inside (PSI)	Outside (PSI)	Inside (PSI)	Outside (PSI)	Inside (PSI)	Outside (PSI)	Inside (PSI)	Outside (PSI)	Inside (PSI)	Outside (PSI)
-37	4.19		5.86		8.15		10.65		13.40	
-32	3.64		5.34		7.68		10.30		13.10	
-27	2.93		4.54		6.71		8.40		11.70	
-22	2.35		3.90		6.00		8.14		10.95	
-17	1.64		3.04		4.98		7.12		9.45	
-12	0.90		2.36		3.96		5.88		8.08	
-7	0.30		1.64		3.10		4.95		6.95	
-2	-0.20		1.06		2.77		4.65		6.75	
0	-0.52	-0.46	0.63	0.78	2.23	2.50	4.03	4.42	6.00	6.45
4	-0.92	-0.90	0.13	0.29	1.62	1.92	3.28	3.80	5.05	5.80
8	-1.26	-1.25	-0.22	-0.03	1.27	1.65	2.94	3.63	4.75	5.74
12	-1.78	-1.67	-0.86	-0.58	0.45	0.86	1.97	2.62	3.55	4.44
16	-1.99	-1.97	-1.10	-0.86	0.07	0.65	1.35	2.39	2.85	4.27
20	-2.08	-2.08	-1.18	-1.05	-0.10	-0.01	1.20	1.35	2.60	2.94
22	-2.02	-2.22	-1.05	-1.20	0.08	-0.10	1.43	1.30	2.90	2.85
27	-2.26	-2.43	-1.37	-1.48	-0.21	-0.48	1.10	0.78	2.56	2.20

Table B-3. Pressure along vertical pipe and bend with sudden expansion at downstream tangent (Configuration A) with vertical adjustment

Distance from Bend Entrance (Diameters)	Re = 3.68x10 <sup>5</sup>		Re = 5.0x10 <sup>5</sup>		Re = 6.16x10 <sup>5</sup>		Re = 7.36x10 <sup>5</sup>		Re = 8.5x10 <sup>5</sup>	
	Inside (PSI)	Outside (PSI)	Inside (PSI)	Outside (PSI)	Inside (PSI)	Outside (PSI)	Inside (PSI)	Outside (PSI)	Inside (PSI)	Outside (PSI)
4	-0.95	-0.93	-0.13	0.03	1.59	1.89	3.46	3.94	4.75	5.47
8	-1.34	-1.36	-0.53	-0.39	1.20	1.53	3.07	3.67	4.40	5.33
12	-1.99	-1.92	-1.32	-1.10	0.24	0.58	1.92	2.47	2.98	3.81
16	-2.42	-2.49	-1.79	-1.67	-0.35	0.08	1.09	1.93	2.06	3.32
20	-2.85	-3.00	-2.22	-2.30	-0.86	-1.04	0.60	0.35	1.47	1.37
22	-2.79	-3.14	-2.08	-2.46	-0.68	-1.14	0.83	0.30	1.78	1.27
27	-3.02	-3.35	-2.40	-2.75	-0.96	-1.53	0.51	-0.25	1.45	0.59

Table B-4. Pressure along vertical pipe and bend with steel pipe at downstream tangent (Configuration B) with vertical adjustment

Distance from Bend Entrance (Diameters)	Re = 3.68x10 <sup>5</sup>		Re = 5.0x10 <sup>5</sup>		Re = 6.16x10 <sup>5</sup>		Re = 7.36x10 <sup>5</sup>		Re = 8.5x10 <sup>5</sup>	
	Inside (PSI)	Outside (PSI)	Inside (PSI)	Outside (PSI)	Inside (PSI)	Outside (PSI)	Inside (PSI)	Outside (PSI)	Inside (PSI)	Outside (PSI)
4	-0.93	-0.91	0.12	0.28	1.61	1.91	3.27	3.79	5.04	5.79
8	-1.31	-1.31	-0.27	-0.09	1.22	1.59	2.89	3.57	4.70	5.68
12	-1.95	-1.86	-1.03	-0.77	0.28	0.67	1.80	2.43	3.38	4.25
16	-2.38	-2.39	-1.49	-1.28	-0.32	0.23	0.96	1.97	2.46	3.85
20	-2.81	-2.87	-1.91	-1.84	-0.83	-0.80	0.47	0.56	1.87	2.15
22	-2.75	-3.01	-1.78	-1.99	-0.65	-0.89	0.70	0.51	2.17	2.06
27	-2.99	-3.22	-2.10	-2.27	-0.94	-1.27	0.37	-0.01	1.83	1.41

## LIST OF REFERENCES

- [1] Merrow, E.W. 2000, "Problems and Progress in Particle Processing," *Chemical Innovation*, **30**, pp. 34-41.
- [2] Bell, T.A., 2005, "Challenges in the Scale-Up of Particulate Processes-an Industrial Perspective," *Powder Tech.*, **150**, pp. 60-71.
- [3] Maeda, M., Hishida, K., and Furutani, T., 1980, "Optical Measurements of Local Gas and Particle Velocity in an Upward Flowing Dilute Gas-Solids Suspension," *Polyphase Flow Transport Technology*, San Francisco, CA.
- [4] Lee, S., and Durst, F., 1982, "On the Motion of Particles in Turbulent Duct Flows," *Int. J. Multiphase Flow*, **8**(2), pp. 125-146.
- [5] Tsuji, Y., Morikawa, Y., and Shiomi, H., 1984, "LDV Measurements of an Air-Solid Two-Phase Flow in a Vertical Pipe," *J. Fluid Mech.*, **139**, pp. 417-434.
- [6] Sheen, H., Chang, Y., and Chiang, Y., 1993, "Two-Dimensional Measurements of Flow Structure in a Two-Phase Vertical Pipe Flow," *Proc. Natl. Sci. Council. ROC(A)*, **17**(3), pp. 200-213.
- [7] van de Wall, E., and Soo, S., "Relative Motion between Phases of a Particular Suspension," *Powder Tech.*, **95**, pp. 153-163.
- [8] Jones, E.N., 2001, "An Experimental Investigation of Particle Size Distribution Effects in Dilute-Phase Gas-Solid Flow," Ph.D. Thesis, Purdue University, West Lafayette, IN.
- [9] Hadinoto, K., Jones, E.N., Yurteri, C., and Curtis, J.S., 2005, "Reynolds Number Dependence of Gas-Phase Turbulence in Gas-Particle Flows," *Int. J. Multiphase Flow*, **31**, pp. 416-434.
- [10] Theofanous, T. and Sullivan, J., 1982, "Turbulence in Two-Phase Dispersed Flows," *J. Fluid Mech.*, **116**, pp. 343-362.
- [11] Wang, S., Lee, S., Jones Jr., O., and Lahey Jr., R., 1987, "3-D Turbulence Structure and Phase Distribution Measurements in Bubbly Two-Phase Flows," *Int. J. Multiphase Flow*, **13**(3), pp. 327-343.
- [12] Hu, B., Mata, O., Hewitt, G. and Angeli, P., 2007, "Mean and Turbulent Fluctuating Velocities in Oil-Water Vertical Dispersed Flows," *Chem. Eng. Sci.*, **62**, pp. 1199-1214.
- [13] Zisselmar, R. and Molerus, O., 1979, "Investigation of Solid-Liquid Pipe Flow with regard to Turbulence Modification," *Chem. Eng. J.*, **18** pp. 233-239.

- [14] Abbas, M. and Crowe, C., 1987, "Experimental Study of the Flow Properties of a Homogeneous Slurry near Transitional Reynolds Numbers", *Int. J. Multiphase Flow*, **13**, pp. 357-364.
- [15] Nouri, J., Whitelaw, J. and Yianneskis, M., 1987, "Particle Motion and Turbulence in Dense Two-Phase Flows," *Int. J. Multiphase Flow*, **13**(6), pp. 729-739.
- [16] Alajbegović, A., Assad, A., Bonetto, F., and Jahey, R., 1994, "Phase Distribution and Turbulence Structure for Solid/Fluid Upflow in a Pipe," *Int. J. Multiphase Flow*, **20**, pp. 453-479.
- [17] Assad, A., Bonetto, F., and Lahey, R. T., 2000, "An Experimental Study of Phase Distribution and Turbulence Structure for Solid/Liquid Flow in a Horizontal Pipe," *Chem. Eng. Comm.*, **179**, pp. 149-177.
- [18] Koh, C., Hookham, P., and Leal, L., 1994, "An Experimental Investigation of Concentrated Suspension Flows in a Rectangular Channel," *J. Fluid Mech.*, **266**, pp. 1-32.
- [19] Averbakh, A., Shauly, A., Nir, A. and Semiat, R., 1997, "Slow Viscous Flows of Highly Concentrated Suspensions—Part I," *Int. J. Multiphase Flow*, **23**, pp. 409-424.
- [20] Hardalupas, Y., Taylor, A., Whitelaw, J., 1989, "Velocity and Particle-Flux Characteristics of Turbulent Particle-Laden Jets," *Proc. Royal Society A*, **26**, pp 31-78.
- [21] Simonin, O., Wang, Q., and Squire, K.D., 1997, "Comparisons between Two-Fluid Model Predictions and Large Eddy Simulation Results in a Vertical Gas-Solid Turbulent Channel Flow," *Proceedings of the 7th International Symposium on Gas-Particle Flows*, ASME.
- [22] Yamamoto, Y., Potthoff, M., Tanaka, T., Kajishima, T., Tsuji, Y., 2001, "Large Eddy Simulation of Turbulent Gas-Particle Flow in a Vertical Channel: Effect of Considering Interparticle Collisions," *J. Fluid Mech.*, **442**, pp. 303-334.
- [23] Bagnold, R., 1954, "Experiments on a Gravity-Free Dispersion of Large Solid Spheres in a Newtonian Fluid Under Shear," *Proc. Royal Society A*, **225**, pp. 49-63.
- [24] Hunt, M.L.; Zenit, R.; Campbell, C.S.; and Brennen, C.E., 2002, "Revisiting the 1954 Suspension Experiments of R.A. Bagnold," *J. Fluid Mech.*, **452**, pp. 1-24.
- [25] Silbert, L.E., Landry, J.W., and Grest, G.S., 2003, "Granular Flow Down a Rough Inclined Plane: Transition between Thin and Thick Piles," *Physics of Fluids*, **15**(1), pp. 1-10.

- [26] Wilson, K.C., 2004, "Rotating-Drum Experiments for Particle-Laden Flows: A New View," *Granular Matter*, **6**, pp. 97-101.
- [27] Kulick J.D., Fessler, J.R., Eaton, J.K., 1994, "Particle Response and Turbulence Modification in Fully Developed Channel Flow," *J. Fluid Mech.*, **277**, pp. 107-134.
- [28] Hosokawa, S. and Tomiyama, A., 2004, "Turbulence Modification in Gas-Liquid and Solid-Liquid Dispersed Two-Phase Pipe Flows," *Int. J. Heat and Fluid Flow*, **24**, pp. 489-498.
- [29] Chemloul, N.S. and Benrabah, O., 2008, "Measurement of Velocities in Two-Phase Flow by Laser Velocimetry: Interaction between Solid Particles' Motion and Turbulence," *J. Fluids Eng.*, **130**, pp.1-10.
- [30] Lyon, M.K. and Leal, L.G., 1998, "An Experimental Study of the Motion of Concentrated Suspensions in Two-Dimensional Channel Flow. Part 1. Monodisperse Systems," *J. Fluid Mech.*, **363**, pp. 25-65.
- [31] Mishra, R., Singh, S.N., and Seshadri, V., 1997, "Velocity Measurement in Solid-Liquid Flows using an Impact Probe," *Flow Meas. Instrum.*, **8**(3/4), pp. 157-165.
- [32] Kiger, K.T. and Pan, C., 2002, "Suspension and Turbulence Modification Effects of Solid Particulates on a Horizontal Turbulent Channel Flow," *J. Turbulence*, **3**, pp. 1-21.
- [33] Liu, Q. Q. and Singh, V. P., 2004, "Fluid-Solid Interaction in Particle-Laden Flows," *J. Eng. Mech.*, **130**(12), pp. 1476-1485.
- [34] Gore, R.A. and Crowe, C.T., 1989, "Effect of Particle-Size on Modulating Turbulent Intensity," *Int. J. Multiphase Flow*, **15**(2), pp. 279-285.
- [35] Hetsroni, G., 1989, "Particles Turbulence Interaction," *Int. J. Multiphase Flow*, **15**(5), pp. 735-746.
- [36] Hutchinson, P., Hewitt, G., and Dukler, A.E., 1971, "Deposition of Liquid or Solid Dispersion from Turbulent Gas Streams: A Stochastic Model," *Chem. Eng. Sci.*, **26**, pp. 419-439.
- [37] Crowe, C.T., 2000, "On Models for Turbulence Modulation in Fluid-Particle Flows," *Int. J. Multiphase Flow*, **26**(5), pp. 719-727.
- [38] Chaouki, J., Larachi, F., and Dudukovic, M., 1997, "Noninvasive Tomographic and Velocimetric Monitoring of Multiphase Flows," *Ind. Eng. Chem. Res.*, **36**, pp. 4476-4503.

- [39] Sakaguchi, T., Shakutsi, H., Tomiyama, A., Minigawa, H., and Kitani, S., 1991, "Microscopic Characteristic of Multiphase Flow using Digital Image Processing," *Proceedings of The International Conference on Multiphase Flows*, Tsukuba, Japan, pp. 357-360.
- [40] Muste, M., Parthasarathy, R. N., and Patel, V. C., 1996, "Discriminator Laser Doppler Velocimetry for Measurement of Liquid and Particle Velocities in Sediment-Laden Flows," *Exp. in Fluids*, **22**, pp. 45-56.
- [41] Brady, J.F. and Bossis, G., 1988, "Stokesian Dynamics," *Annual Rev. Fluid Mech.*, **20**, pp. 111-157.
- [42] Anderson, T., and Jackson, R., 1967, "A Fluid Mechanical Description of Fluidized Beds," *Ind. Eng. Chem. Fund.*, **6**, pp. 527-539.
- [43] Tavoularis, S., 2005, "Measurement of wall shear stress," *Measurement in Fluid Mechanics*, Cambridge University Press, pp. 328-344.
- [44] Prandtl, L., 1935, "The Mechanics of Viscous Fluids," *Aerodynamic Theory*, Springer-verlag.
- [45] Albrecht, H.E., Borys, M., Wenzel, M., Thomas, W., 1994, "Influence of the Measurement Volume on the Phase Error in Phase Doppler Anemometry Part I: Reflective Mode Operation," *Part. Part. Sys. Char.*, **11**, pp. 339-344.
- [46] Albrecht, H.-E., Borys, M., Damaschke, N., and Tropea, C., 2003, *Laser Doppler and Phase Doppler Measurement Techniques*, Springer, New York.
- [47] Goldstein, R.J. 1983, *Fluid Mechanics Measurements*, Hemisphere Publishing Corporation, New York.
- [48] Durst, F. and Zare, M., 1975, "Laser-Doppler Measurements in Two-Phase Flows," *Proceedings of the LDA-Symposium*, Copenhagen, pp. 403-429.
- [49] Dullenkopf, K., Willmann, M., Wittig, S., Schone, F., Stieglmeier, M., Tropea, C., Mundo, C., 1998, "Comparative Mass Flux Measurements in Sprays using a Patternator and the Phase-Doppler Technique," *Part. Part. Sys. Char.*, **15**, pp. 81-89.
- [50] Aísa, L., Garcia, J.A., Cerecedo, L.M., García Palacín, I., Calvo, E., 2002, "Particle Concentration and Local Mass Flux Measurements in Two-Phase with PDA Application to a Study on the Dispersion of Spherical Particles in a turbulent Air Jet," *Int. J. Multiphase Flow*, **28**, pp. 301-324.
- [51] Roisman, I.V. and Tropea, C., 2001, "Flux Measurements in Sprays Using Phase Doppler Techniques," *Atomization and Sprays*, **11**(6), pp. 667-699.

- [52] Qiu, J.-H and Sommerfeld, M., 1992, "A Reliable Method for determining the Measurement Volume Size and Particle Mass Fluxes using Phase-Doppler Anemometry," *Exp. in Fluids*, **13**, pp. 393-404.
- [53] Saffman, M., 1987, "Automatic Calibration of LDA Measurement Volume Size," *Applied Optics*, **26**, pp. 2592-2597.
- [54] Qiu, J.-H and Sommerfeld, M., 1995, "Particle Concentration Measurements by Phase-Doppler Anemometry in Complex Dispersed 2-Phase Flows," *Exp. in Fluids*, **18**(3), pp. 187-198.
- [55] Van den Moortel, T., Santini, R., Tadriss, L., and Pantaloni, J., 1997, "Experimental Study of the Particle Flow in a Circulating Fluidized Bed using a Phase Doppler Particle Analyser: A new Post-Processing Data Algorithm," *Int. J. Multiphase Flow*, **23**(6), pp. 1189-1209.
- [56] Bergenblock, T., Lecknew, B., Onofri, F., Occelli, R., and Tadriss, L., 2006, "Averaging of Particle Data from Phase Doppler Anemometry in Unsteady Two-Phase Flow: Validation by Numerical Simulation," *Int. J. Multiphase Flow*, **32**, pp. 248-268.
- [57] Assar, M., 1996, "A Theoretical and Experimental Study of Slurry Flow," Ph.D. Thesis, Case Western Reserve University, Cleveland, OH.
- [58] Chen, R.C. and Kadambi, J.R., 1995, "Discrimination between Solid and Liquid Velocities in Slurry Flow using Laser Doppler Velocimeter," *Powder Tech.*, **85**, pp. 127-134.
- [59] Yanta, W. and Smith, R., 1973, "Measurements of Turbulence Transport Properties with a Laser Doppler Velocimeter," Paper No. 73-169, *AIAA 11th Aerospace Sciences Meeting*, Washington, DC.
- [60] Lun, C.K.K., and Savage, S., 1987, "Kinetic Theory for Rapid Flow," unpublished manuscript, McGill University, Canada.
- [61] Lun, C.K.K., and Savage, S., 2003, "Kinetic Theory for Inertia Flows of Dilute Turbulent Gas-Solids Mixtures," *Lecture Notes in Physics: Theory of Granular Gases*, Springer, New York, pp. 267-289.
- [62] Myong, H.K. and Kasagi, N., 1990, "A New Approach to the Improvement of Kappa-Epsilon Turbulence Model for Wall-Bounded Shear Flows," *JSME Int. J. Series II*, **33**(1), pp. 63-72.
- [63] Lun, C.K.K., Savage, S.B., Jeffrey, D.J., and Chepuruiy, N., 1984, "Kinetic Theory for Granular Flow: Inelastic Particles in Couette Flow and Slightly Inelastic Particles in a General Flowfield," *J. Fluid Mech.*, **140**, pp. 223-256.

- [64] Sinclair, J.L. and Jackson, R., 1989, "Gas-Particle Flow in a Vertical Pipe with Particle-Particle Interactions," *AIChE J.*, **35**, pp. 1473-1486.
- [65] Louge, M.Y., Mastorakos, E., and Jenkins, J.K., 1991, "The Role of Particle Collisions in Pneumatic Transport," *J. Fluid Mech.*, **231**, pp. 345-359.
- [66] Bolio, E.J., Yusuna, J.A., and Sinclair, J.L., 1995, "Dilute Turbulent Gas-Solid Flow in Risers with Particle-Particle Interactions," *AIChE J.*, **41**, pp. 1375-1388.
- [67] Tsuji, Y., 1993, Private communication, Osaka, Japan.
- [68] Johnson, P.C. and Jackson, R., 1987, "Frictional-Collisional Constitutive Relations for Granular Materials, with Application of Plane Shearing," *J. Fluid Mech.*, **176**, pp. 67-93.
- [69] Patankar, S.V., 1980, *Numerical Heat Transfer and Fluid Flow*, Hemisphere Publishing Co., New York.
- [70] Berger, S.A., Talbot, L., and Yao, L.-S., 1983, "Flow in Curved Pipes," *Annual Rev. of Fluid Mech.*, **15**, pp. 461-512.
- [71] Ito, H., 1987, "Flow in Curved Pipes," *Jap. Sch. Mech. Eng. Int. J.*, **30**, pp. 543-552.
- [72] Ito, H., 1960, "Pressure Losses in Smooth Pipe Bends," *J. Basic Eng. ASME* **82**, pp. 131-143.
- [73] Miller, D.S., 1990, 2nd Ed., *Internal Flow Systems*, BHRA, Cranfield UK, pp. 205-209.
- [74] 1980, "Flow of Fluids through Valves, Fittings, and Pipe," Technical Paper No. 410, Crane Company, New York, NY.
- [75] Rowe, M., 1970, "Measurements and Computations of Flow in Pipe Bends," *J. Fluid Mech.*, **43**(4), pp. 771-783.
- [76] Anwer, M., So, R. M. C., and Lai, Y.G., 1989, "Perturbation by and Recovery from Bend Curvature of a Fully Developed Turbulent Pipe Flow," *Physics of Fluids A*, **1**(8), pp. 1387-1397.
- [77] Anwer, M., and So, R.M.C., 1993, "Swirling Turbulent Flow through a Curved Pipe," *Exp. in Fluids*, **14**, pp. 85-96.
- [78] Sudo, K., Sumida, M., and Hibara, H., 1998, "Experimental Investigation on Turbulent Flow in a Circular-Sectioned 90-degree Bend," *Exp. in Fluids*, **25**, pp. 42-49.

- [79] Sudo, K., Sumida, M., and Hibara, H., 2000, "Experimental Investigation on Turbulent Flow through a Circular-Sectioned 180° Bend," *Exp. in Fluids*, **28**, pp. 51-57.
- [80] Crawford, N. M., Cunningham, G., and Spence, S. W. T., 2007, "An Experimental Investigation into the Pressure Drop for Turbulent Flow in 90° Elbow Bends," *Proc. Inst. Mech. Eng. E J. Proc. Mech. Eng.*, **221**, pp. 77-88.
- [81] Coffield, R. D., Brooks, P. S., and Hammond, R. B., 1994, "Piping Elbow Irrecoverable Pressure Loss Coefficients for Moderately High Reynolds Numbers," DE-AC11-93PN38195, Bettis Atomic Power Laboratory, West Mifflin, PA.
- [82] Hawthorne, W.R., 1951, "Secondary Circulation in Fluid Flow," *Proc. Royal Society A, Mathematical and Physical Sciences*, **206**(1046), pp. 374-387.
- [83] Ward-Smith, A.J., 1980, *Internal Fluid Flow: the Fluid Dynamics of Flow in Pipes and Ducts*, Clardon Press, Oxford, pp. 280.
- [84] Laufer, J., 1954, "The Structure of Turbulence in Fully Developed Pipe Flow," Report 1174, NACA.
- [85] Perry, A. and Abell, C., 1975, "Scaling laws for pipe-flow turbulence," *J. Fluid Mech.*, **67**(2), pp. 257-271.
- [86] Lawn, C., 1971, "The Determination of the Rate of Dissipation in Turbulent Pipe Flow," *J. Fluid Mech.*, **48**(3), pp. 477-505.
- [87] Schildknecht, M., Miller, J., and Meier, G., 1979, "The Influence of Suction on the Structure of Turbulence in Fully Developed Pipe Flow," *J. Fluid Mech.*, **90**(1), pp. 67-107.
- [88] Van Doorne, C. and Westerweel, J., 2007, "Measurement of Laminar, Transitional, and Turbulent Pipe Flow using Stereoscopic-PIV," *Exp. in Fluids*, **42**(2), pp. 259-279.
- [89] Fujiwara, A., Minato, D. and Hishida, K. 2004, "Effect of Bubble Diameter on Modification of Turbulence in an Upward Pipe Flow," *Int. J. Heat and Fluid Flow*, **25**, pp. 481-488.
- [90] Eggels, J., Unger, F., Weiss, M., Westerweel, J., Adrian, R., Friedrich, R., and Nieuwstadt, F., 1994, "Fully Developed Turbulent Pipe Flow: A Comparison between Direct Numerical Simulation and Experiment," *J. Fluid Mech.*, **268**, pp. 175-209.

- [91] Wu, X. and Moin, P., 2008, "A Direct Numerical Simulation Study on the Mean Velocity Characteristics in Turbulent Pipe Flow," *J. Fluid Mech.*, **608**, pp. 81-112.
- [92] Zhao, R. and Smits, A.J., 2007, "Scaling of the Wall-Normal Turbulence Component in High-Reynolds-Number Pipe Flow," *J. Fluid Mech.*, **576**, pp. 457-473.
- [93] Morrison, J. F., McKeon, B. J., Jiang, W., and Smits, A. J., 2004, "Scaling of the Streamwise Velocity Component in Turbulent Pipe Flow," *J. Fluid Mech.*, **508**, pp. 99-131.
- [94] Schlichting, H., 1979, *Boundary-Layer Theory*, McGraw-Hill, New York.
- [95] den Toonder, J., and Nieuwstadt, F., 1997, "Reynolds Number Effects in a Turbulent Pipe Flow for Low to Moderate Re," *Physics of Fluids*, **9**(11), pp. 3398-3409.
- [96] Comte-Bellot, G., 1976, "Hot-Wire Anemometry," *Annual Rev. Fluid Mech.*, **8**, pp. 209-231.
- [97] Shawkat, M., Ching, C., and Shoukri, M., 2007, "On the Liquid Turbulence Energy Spectra in Two-Phase Bubbly Flow in a Large Diameter Vertical Pipe," *Int. J. Multiphase Flow*, **33**, pp. 300-316.
- [98] Sumner, R.J., 1993, "Pipeline Flow of Slurries and Emulsions," Ph.D. Thesis, University of Saskatchewan, Saskatoon, Canada.
- [99] Shook, C.A. and Bartosik, A.S., 1994, "Particle-wall Stresses in Vertical Slurry Flows," *Powder Tech.*, **81**, pp. 117-124.
- [100] Bartosik, A.S., 1996, "Modeling the Bagnold Stress Effects in Vertical Slurry Flow," *J. Hydrol. Hydromech.*, **44**(1), pp. 49-58.
- [101] Matoušek, V., 2002, "Pressure Drops and Flow Patterns in Sand-Mixture Pipes," *Exp. Therm. Fluid Sci.*, **26**, pp. 693-702.
- [102] Matoušek, V., 2009, "Pipe-Wall Friction in Vertical Sand-Slurry Flows," *Part. Sci. and Tech.*, **27**, pp. 456-468.
- [103] Littman, H. and Paccione, J.D., 2007, "Effect of Large Particles on the Augmentation of Wall Friction in Vertical Pneumatic and Hydraulic Transport in a Turbulent Fluid," *Ind. Eng. Chem. Res.*, **46**, pp. 3429-3442.
- [104] Churchill, S.W., 1977, "Friction-factor Equation Spans all Fluid-flow Regimes," *Chem. Eng.*, **84**(24), pp. 91-92.

- [105] Ferre, A.L. and Shook, C.A, 1998, "Course Particle Wall Friction in Vertical Slurry Flows," Part. Sci. and Tech., **16**, pp. 125-133.
- [106] Sifferman, T.R., and Greenkorn, R.A., 1981, "Drag Reduction in Three Distinctly Different Fluid Systems," Soc. Petroleum Eng. J., **21**(6), pp. 663-669.
- [107] Zandi, I., 1967, "Decreased head Losses in Raw Water Conduits," J. Amer. Water. Works. Ass., **59**, pp. 213.
- [108] Radin, I, Zakin, J.L., and Patterson, G.K., 1975, "Drag Reduction in Solid-Fluid Systems," AIChE J., **21**(2), pp. 358-371.

## BIOGRAPHICAL SKETCH

Mark Pepple was born in 1979 in Park Ridge, Illinois. The second of two sons, he grew up in Elmhurst, Illinois, graduating from York High School in 1998. He then enrolled at the University of Illinois, Urbana-Champaign (UIUC), where he graduated with a Bachelor of Science in chemical engineering in December 2002. While at UIUC, he was a member of the cross country and track and field teams and was extensively involved with Intervarsity Christian Fellowship.

Before beginning his Ph.D. in chemical engineering at the University of Florida in August 2004, he held positions at the Illinois State Geological Survey and ChemSensing Inc., volunteered with Intervarsity Christian Fellowship, and began a Master of Arts in religion at Trinity Evangelical Divinity School. While working toward his doctorate, Mark attempted to balance his life with other activities. This included running up to 80 miles a week, posting personal records from 3k to 10k, and competing at the 2009 USA Track and Field club cross country national championship. Additionally, he was a member of the Graduate Christian Fellowship, a student organization, serving as president for two years.